

Constrained MR Image Reconstruction of Undersampled Data from Multiple Coils

Ph.D. Thesis

conducted at the

Institute of Medical Engineering,
Graz University of Technology



by

Florian Knoll

April 18, 2011

Supervisor: Univ.-Prof. DI. Dr. Rudolf Stollberger

EIDESSTATTLICHE ERKLÄRUNG

Ich erkläre an Eides statt, dass ich die vorliegende Arbeit selbstständig verfasst, andere als die angegebenen Quellen/Hilfsmittel nicht benutzt und die den benutzten Quellen wörtlich und inhaltlich entnommenen Stellen als solche kenntlich gemacht habe.

Graz, am _____
Datum

Unterschrift

STATUTORY DECLARATION

I declare that I have authored this thesis independently, that I have not used other than the declared sources/resources and that I have explicitly marked all material which has been quoted either literally or by content from the used sources.

Graz, _____
Date

Signature

Abstract

While Magnetic Resonance Imaging (MRI) is recognized to be the leading diagnostic imaging modality for numerous diseases, it is often limited by the long examination times. The main reason for this is that for MRI encoding only a limited number of data points can be encoded from one MR signal (FID or echo) and the measurement has to be repeated for many times. Increasing imaging speed has always been a major research area ever since the first experiments in the 1970s, and improvements in this field have contributed significantly to pave the way for clinical application of MRI. One way to accelerate data acquisition is to reduce the number of data points that are used to reconstruct an image with a defined resolution. However, as this approach violates the Nyquist-Shannon sampling theorem, aliasing artifacts are introduced in the reconstructions which have to be eliminated. This can be done by incorporating additional a-priori knowledge during the image reconstruction process. Examples are the use of multiple channels for signal reception (parallel imaging) or the application of dedicated regularization terms which penalize aliasing artifacts in the reconstructed images. This work demonstrates the use of newly developed image reconstruction methods which allow to reconstruct images from highly accelerated data. Numerous examples based on simulations, phantom- and in-vivo-measurements are presented. It is also shown that parallelized implementations of these approaches can be achieved on dedicated graphics hardware which leads to a fundamental reduction of computation time.

Keywords: Magnetic Resonance Imaging (MRI), Image Reconstruction, Accelerated Imaging, Constrained Reconstruction, Parallel Imaging, Inverse Problems, Numerical Optimization.

Zusammenfassung

Die Magnetresonanztomographie (MRT) ist die führende diagnostische Bildgebungsmodalität für eine Vielzahl von häufig auftretenden Erkrankungen. Eine der Haupteinschränkungen der MRT entsteht durch die lange Untersuchungsdauer. Der Grund für die langsame Datenaufnahme im Vergleich zu anderen Modalitäten liegt darin, dass bei der MR-Bildkodierung nur eine beschränkte Anzahl an Datenpunkten durch ein einzelnes MR-Signal aufgenommen werden kann, und die Messung mehrmals wiederholt werden muss. Die Verkürzung der Messzeit war daher seit den ersten MR-Experimenten der 1970er Jahre ein sehr aktives Forschungsgebiet und die Errungenschaften in diesem Bereich haben wesentlich zur klinischen Anwendung der MRT beigetragen. Eine Möglichkeit die Messzeit zu verringern besteht darin die Anzahl der Daten, die verwendet werden um ein Bild mit einer definierten Auflösung zu rekonstruieren, zu verringern. Da dies allerdings das Nyquist-Shannon-Abtasttheorem verletzt, führt diese Vorgehensweise zu Aliasing-Artefakten in den rekonstruierten Bildern, die im Zuge der Bildrekonstruktion entfernt werden müssen. Dies kann dadurch erreicht werden, dass zusätzliches a-priori Wissen im Zuge der Rekonstruktion verwendet wird. Beispiele sind die Verwendung von mehreren Empfangsspulen zur Aufnahme des MR-Signals (parallele Bildgebung) oder die Verwendung von speziellen Straftermen zur Regularisierung, die das Auftreten von Artefakten in den rekonstruierten Bildern verhindern. Diese Arbeit zeigt die Anwendung von neuen Methoden zur Bildrekonstruktion, die es erlauben Rekonstruktionen von stark unterabgetasteten Daten zu erhalten. Die Arbeit beinhaltet eine Vielzahl von Experimenten, basierend auf Simulationen Phantom- sowie in-vivo-Messungen. Es wird auch gezeigt, dass die vorgeschlagenen Ansätze parallelisiert auf Graphik-Hardware implementiert werden können, was zu einer entscheidenden Verkürzung der Rechenzeit führt.

Schlüsselwörter: Magnetresonanztomographie (MRT), Bildrekonstruktion, Beschleunigte Bildgebung, Parallele Bildgebung, Inverse Probleme, Numerische Optimierung.

Contents

Abstract	v
Zusammenfassung	vii
List of figures	xiii
List of tables	xxi
1 Introduction	1
1.1 Outline of the thesis	2
2 MR Image Reconstruction	7
2.1 Spatial Signal Encoding and Image Reconstruction	7
2.2 k -space Sampling	8
2.3 Infinite Discrete k -space Sampling	10
2.4 Discrete Finite k -space Sampling	12
2.5 Aliasing	12
2.6 Reconstruction of non-Cartesian data	15
2.7 Parallel Imaging	20
2.7.1 Introduction	20
2.7.2 Phased array coils	20
2.7.3 Array Coil Compression	22
2.7.4 SENSE Reconstruction	24
2.7.5 GRAPPA Reconstruction	26
2.7.6 Estimation of coil sensitivities and extensions of SENSE and GRAPPA	29
2.8 Formulation of image reconstruction as an inverse problem	32
2.9 Constrained Reconstruction	34
2.10 Evaluation of Image Quality and Validation of Image Reconstruction Algorithms	36
3 Adapted Random Sampling Patterns for Accelerated MRI	37
3.1 Introduction	37
3.2 Theory	38
3.3 Materials and Methods	39
3.3.1 Downsampling experiments	39
3.3.2 Accelerated in vivo measurements	40

3.4	Results	41
3.5	Discussion	44
3.6	Conclusion	47
4	Total Generalized Variation (TGV) for MRI	49
4.1	Introduction	49
4.2	Theory	50
4.2.1	The Concept of Total Generalized Variation	50
4.2.2	Application of TGV in MRI	51
4.3	Materials and Methods	52
4.3.1	Application of TGV for denoising	52
4.3.2	Image reconstruction of Subsampled Multicoil Radial Data with a TGV Constraint	54
4.3.3	MR Image Reconstruction of Subsampled Spiral Data from Multiple Coils	54
4.4	Results	55
4.4.1	Application of TGV for Denoising	55
4.4.2	Image Reconstruction of Subsampled Multicoil Radial Data with a TGV Constraint	55
4.4.3	MR Image Reconstruction of Subsampled Spiral Data from Multiple Coils	58
4.5	Discussion	60
4.5.1	Choice of the Regularization Parameter	62
4.5.2	Computational Requirements	63
4.5.3	Extensions	64
4.6	Conclusions	65
5	Parallel Imaging with Nonlinear Reconstruction using Variational Penalties	67
5.1	Introduction	67
5.2	Theory	68
5.3	Materials and Methods	69
5.3.1	Data Acquisition	69
5.3.2	Nonlinear reconstruction	70
5.3.3	Parameter Choice	70
5.4	Results	70
5.5	Discussion	72
5.6	Conclusions	78
6	Fast Reduction of Undersampling Artifacts in Radial MR Angiography with 3D Total Variation on Graphics Hardware	81
6.1	Introduction	81
6.2	Theory	82
6.2.1	Undersampled Radial Imaging and Total Variation	82
6.2.2	GPU Implementation	83
6.3	Materials and Methods	85

6.3.1	Phantom Measurements	85
6.3.2	In vivo Angiography Measurements	85
6.3.3	Reconstruction Time of the GPU Implementation	86
6.4	Results	87
6.5	Discussion	91
6.6	Conclusions	93
7	Summary and Future Work	95
7.1	Summary	95
7.2	Future Work	96
A	Appendix: Numerical Algorithms	99
A.1	Algorithms for TGV	99
A.1.1	TGV denoising	100
A.1.2	TGV undersampling reconstruction	101
A.2	Algorithms for IRGN T(G)V	102
A.2.1	Solution of the IRGN-TV sub-problem	102
A.2.2	Solution of the IRGN-TGV sub-problem	103
A.2.3	Parameter Choice	103
	Bibliography	105
	Curriculum Vitae	115
	List of Publications as First Author	117
	Acknowledgments	121

List of Figures

2.1	Cartesian spin echo sampling: The pulse sequence (a) and the corresponding k -space trajectory (b) are displayed.	9
2.2	Radial spin echo sampling: The pulse sequence (a) and the corresponding k -space trajectory (b) are displayed.	9
2.3	Illustration of the effects of discrete infinite sampling of the MR signal $s(k_x)$ on the reconstructed spin density (corresponding to the reconstructed image). Sampling, which results in a discrete but infinite signal $\hat{s}_\infty(k_x)$, can be formulated as a multiplication of the original continuous signal $s(k_x)$ with a sampling function $\phi_\infty(k_x)$, which is comprised of an infinite series of equidistant Dirac delta functions (left column). With the use of the Fourier convolution theorem, it can be shown that this operation is equivalent to a convolution of the original underlying physical spin density $\rho(x)$ with $\Phi_\infty(x)$, the inverse Fourier transform of the sampling function, which is another infinite series of Dirac delta functions with spacing $FOV = \frac{2\pi}{\Delta k_x}$ (right column). If the length of the object L is smaller than the FOV , the sampling theorem (equation 2.12) is fulfilled and the reconstructed images do not overlap.	11
2.4	In real world MR-measurements, only a finite number of samples are acquired. This can be expressed as a multiplication with a rectangular window function $w(k_x)$, keeping $N = 2n$ sample points (left column). With the use of the Fourier convolution theorem, it can be shown that this operation is equivalent to a convolution of the reconstructed spin density $\hat{\rho}_\infty(x)$ with $W(x)$, the inverse Fourier transform of the rectangular window function $w(k_x)$, which is a <i>sinc</i> function (right column). This leads to blurring and Gibb's ringing artifacts in the final reconstruction $\hat{\rho}(x)$	13
2.5	Illustration of the effect of aliasing: The spacing Δk_x^A of the sampling function $\Phi_\infty^A(k_x)$ is increased by 2. The $FOV^A = \frac{2\pi}{\Delta k_x^A}$ is halved, and $L > FOV$. The periodic replicates $\hat{\rho}_\infty^A(x)$ overlap, and cannot be separated from each other anymore.	14

2.6 Radial sampling trajectory with 256 radial spokes and 384 sample points on each spoke, corresponding to an oversampling ratio of 1.5 in the readout direction. The k -space coordinates are normalized and range from -0.5 ($-k_{max}$) to $+0.5$ ($+k_{max}$) (left). Corresponding density compensation function (DCF). Note that the minimum of the DCF corresponds to the center of k -space where all radial spokes intersect. However, the minimum value does not reach zero, as this would result in a complete elimination of the signal at the center of k -space. In this example, the minimum value of the DCF is 0.0013 (right). 17

2.7 Radial k -space data obtained with the sampling trajectory of Figure 2.6 with 256 radial spokes, each consisting of 384 sample points (each spoke is one column in the data matrix) (top row), the result of the convolution operation which interpolates the data points on a Cartesian grid (middle row), and the reconstructed image after the application of an inverse Fourier transform (bottom row). These steps are performed for both the original radial data (left column), and for density compensated data (right column), using the DCF from Figure 2.6. The reduced signal intensity in the center of k -space can be observed for both radial and re-gridded data. In the absence of density compensation, the effect of overweighting of the low frequencies yields a significantly blurred image. 18

2.8 Reconstructed image from regridded k -space data (Figure 2.7) before and after deapodization (a), and horizontal cross-section plots through the central row (128) of the image matrix (b). 19

2.9 Examples of subsampling with different sampling trajectories. 21

2.10 An example of a measurement with a 4 channel head coil. The images from the individual coil elements, as well as a sum of squares (SOS) combination, are displayed. 22

2.11 Plot of the singular values of the SVD decomposition of MR data from a 32 channel head coil. 23

2.12 Comparison of a reconstructed image obtained with a 32 channel head coil (left), and a reconstruction from 10 virtual coil elements, generated by means of truncated SVD. 24

2.13 Illustration of SENSE reconstruction for acceleration factor $R = 2$ and $N_c = 4$. The pixels from all N_c coils can be stacked in a single complex signal vector \vec{I} with dimension $N_c \times 1$. The same can be done with all superimposed pixels from the full FOV image $\hat{\rho}$, which form an $R \times 1$ vector $\vec{\hat{\rho}}$. C can then be written as an $N_c \times R$ matrix consisting of the coil sensitivities of all N_c coils at the R superimposed positions, which leads to a system of linear equations that can be written in matrix form. 25

- 2.14 SENSE reconstruction with acceleration factors $R = 2, 3, 4$ for a 4 channel data set. While the reconstruction for $R = 2$ yields an almost perfect image, the result for $R = 3$ is already slightly corrupted by noise and residual aliasing artifacts. Pronounced non-uniform noise enhancement can be observed in the case of $R = 4$. Note that noise amplification is highest in the central parts of the image, due to the highest amount of overlap of the coil sensitivities in this region (a). This is also illustrated by cross-section plots across a vertical line (direction of acceleration) of the reconstructions (b). Coil sensitivities were estimated with a normalization of the individual coil $\hat{\rho}_k$ images by the corresponding SOS combination $\hat{\rho}_{SOS}$ (equation 2.23), followed by filtering with a 2D Gaussian low pass filter (c). 27
- 2.15 Illustration of GRAPPA reconstruction for acceleration factor $R = 4$, using 12 ACS lines and a 5×2 GRAPPA reconstruction kernel (see text for details). 29
- 2.16 GRAPPA reconstruction with acceleration factors $R = 2, 3, 4$ for a 4 channel data set. 12 ACS lines at the center of k -space were used to estimate the GRAPPA coefficients, yielding slightly lower total acceleration factors than the SENSE reconstructions of Figure 2.14 (a). Results of GRAPPA reconstructions of a single coil, as well as corresponding coil images after an inverse Fourier transform. The striped patterns in k -space, resulting from inconsistencies between acquired data and data points that were reconstructed with GRAPPA can clearly be depicted for $R = 3$ and especially $R = 4$ (b). 30
- 2.17 Illustration of the problem of errors in the coil sensitivity estimation due to object motion: SENSE reconstruction for undersampled data with acceleration factor $R = 2$, identical to Figure 2.14. No object movement occurred between coil sensitivity estimation and SENSE reconstruction, which yields a reasonable reconstruction (left). Using the same sensitivities after a slight rotation of the imaged object leads to residual aliasing artifacts in the reconstruction (middle). If the rotating motion is increased, aliasing artifacts become more severe (right). 32
- 2.18 Schematic representation of the steps that are performed by the system matrix K and the adjoint matrix K^H , adapted from [1]. Input to K is an image vector \vec{u} of length $N^2 \times 1$ in the case of an $N \times N$ image matrix, and the output is a k -space data vector \vec{s} with sample points on an arbitrary trajectory from a single individual coil. The length of this vector depends on the specific sampling pattern and the amount of undersampling that was used during data acquisition. In the case of the adjoint matrix K^H , the input is a data vector \vec{s} from a single coil, and the output is an image vector \vec{u} corresponding to an $N \times N$ image matrix without modulation by the coil sensitivity. In both cases, estimations of the coil sensitivities need to be available and have to be determined in a previous step. 33
- 3.1 Example of a pdf (left) and a sampling pattern with subsampling factor $R = 4$ generated from it using a Monte Carlo method (right). k_y and k_z denote the two phase encoding directions; the frequency encoding direction is orthogonal to the image plane. The pdf was obtained from a reference scan and was used to generate the sampling patterns for the in vivo experiments (cf. Figure 3.5). 39

- 3.2 Comparison of reconstruction results for different sampling patterns: Random sampling with non-optimized (left) and optimized (middle) polynomial powers, and the proposed template based method (right) for acceleration factors of $R=4$ and $R=9$. The k -space data sets of the different sampling strategies (two top rows) and GRAPPA reconstructions (two bottom rows) are shown. 42
- 3.3 Comparison of reconstruction results when different templates are used to generate the sampling pattern. An adjacent slice of the same data set as the undersampled slice (first column), a rotation of this slice (second column), a more cranial slice with slightly different anatomy and size of the head (third column), a data set of a different volunteer with different contrast (fourth column) and completely different anatomy (fifth column) were used. The templates, corresponding sampling patterns and GRAPPA reconstructions are shown for $R=4$ and $R=9$. . . 43
- 3.4 Template image used to generate the sampling pattern, fully sampled gold standard and reconstruction results of the experiments with the knee data set are shown. Left column: Used sampling pattern. Middle left column: undersampled and zero-filled (SOS) images. Middle right column: GRAPPA reconstruction. Right column: k -space of corresponding GRAPPA reconstruction. Top row: $R=2$. Bottom row: $R=4$ 45
- 3.5 Template image used to generate the sampling pattern and reconstruction results of accelerated in-vivo measurements for different subsampling factors are shown. Left column: Used sampling pattern. Middle left column: undersampled and zero-filled (SOS) images. Middle right column: GRAPPA reconstruction. Right column: k -space of corresponding GRAPPA reconstruction. Top row: $R=4$. Bottom row: $R=10$ 46
- 4.1 Denoising a ramp image with TV and TGV penalty. The noisy test image f (left), its Total-Variation regularization (middle) and its Total-Generalized-Variation regularization (4.3) (right). The absence of staircasing artifacts for TGV can nicely be observed here. 51
- 4.2 Reconstructions of a Shepp-Logan phantom from undersampled radial k -space data, modulated with a simulated coil sensitivity generated with the use of Biot-Savart's law. Top row: Original test image of size 256×256 (left) and the corresponding radial sampling pattern with 24 radial spokes (right). Middle row: Conventional NUFFT Reconstruction (left), Minimum-TV-Solution (4.4) (middle) and Minimum-TGV $_{\alpha}^2$ -Solution (4.5) (right). Bottom row: Magnified views from the middle row. 53
- 4.3 TV (middle) and TGV (right) denoising results from the contrast enhanced T_1 weighted prostate scan. The images show smooth modulations due to inhomogeneities of the exciting B_1 field and the surface coils used for signal reception which lead to significant artifacts when conventional TV is applied. 56

4.4	Denoising experiments for the T_2 weighted brain scan. In the top row, the original image with high SNR (left) which has been contaminated with additive Gaussian noise (middle left) is shown. TV (middle right) and TGV (right) denoising results are displayed as well as magnified views of the respective images (middle and bottom rows). An example of an unwanted image feature that is introduced during denoising is highlighted by arrows.	56
4.5	Results from experiments with the T_2 weighted brain scan (256×256 matrix) using 32, 24, 16 and 12 radial projections. The columns depict conventional NUFFT reconstructions (left), reconstructions with CG-SENSE (middle left), with a TV constraint (middle right) and with a TGV constraint (right), respectively. The original, fully sampled image is displayed in Figure 4.4.	57
4.6	Magnified views of the same data as shown in Figure 4.5. The tendency of TV to introduce additional staircases is visible at the frontal interface of the ventricle (highlighted).	58
4.7	Radial image reconstructions of accelerated measurements of the human brain (256×256 matrix) from 96, 48, 32 and 24 projections. The columns depict conventional NUFFT reconstructions (left), reconstructions with CG-SENSE (middle left), with a TV constraint (middle right) and with a TGV constraint (right), respectively.	59
4.8	Reconstruction of subsampled spiral data of the brain. Conventional minimum norm solution (left column) and reconstruction with TGV regularization (right column). Results of undersampled data from 24, 16 and 12 spiral interleaves are shown.	60
4.9	Reconstruction of subsampled spiral data of synthetic MR-angiography data generated from a projection X-ray measurement. Conventional minimum norm solution (left column) and reconstruction with TGV regularization (right column). Timeframes 1, 5, 10 and 20 are displayed.	61
4.10	Denoising (top row) and radial image reconstruction with 32 radial projections (256×256 matrix) from the downsampled (middle row), and the in-vivo accelerated (bottom row) experiments. Results with a high regularization weight (left), an appropriate weight (middle) and a low weight (right) are shown.	63
5.1	Reconstructions of pseudo random sampling, phantom data set. IRGN (left), IRGN-TV (right). Acceleration factors $R = 4$ (top, $\beta_{min} = 0$) and $R = 10$ (bottom, $\beta_{min} = 5 \cdot 10^{-3}$).	71
5.2	Comparison of IRGN (top row) and IRGN-TV (bottom row) for pseudorandom subsampling of the T_2 weighted brain dataset ($\beta_{min} = 0$). From left: fully sampled acquisition, acceleration factors $R = 4$, $R = 6$, $R = 8$	73
5.3	Reconstructions of pseudo random sampling, brain data set. IRGN (left) and IRGN-TV (right). Acceleration factor $R = 4$, $\beta_{min} = 0$	74
5.4	Reconstructions of radial sampling, phantom data, two different slices. IRGN (left) and IRGN-TV (right). 25 spokes were used for the reconstruction of a 128×128 image, $\beta_{min} = 5 \cdot 10^{-3}$	75

5.5 Comparison of IRGN (left) and IRGN-TV (middle) for radial real-time imaging of the beating human heart without cardiac gating and during free breathing ($\beta_{\min} = 5 \cdot 10^{-3}$). Top: 25 spokes. Highlighted are structures with little signal intensity that can be lost due to strong TV regularization. Middle: 21 spokes. Highlighted are structures of similar size but slightly higher signal intensity that are preserved even in case of TV regularization. Bottom: 19 spokes. The plots on the right show signal intensities across a horizontal line, indicated in the top row of the reconstruction results. The ability of IRGN-TV to preserve sharp edges is highlighted in the plot of the reconstruction from 19 spokes. The arrow marks the sharp boarder of the ventricle, which is depicted equally well with IRGN and IRGN-TV. The undesired loss of a small structure is highlighted in the plot of the reconstruction from 21 spokes. The plot crosses two adjacent vessels, which are both represented in the IRGN solution, but only the left one appears in the IRGN-TV reconstruction. 76

5.6 Comparison of conventional TV (left) and TGV (right) regularization for phantom experiments where modulations from the coil sensitivities lead to pronounced staircasing artifacts when TV is applied. Left: magnified regions from Figures 5.1 (R=10, top) and 5.4 (bottom); right: IRGN-TGV reconstruction of the same data set (with $\beta_{\min} = 5 \cdot 10^{-3}$). 77

6.1 Stack of stars trajectory with shifted projection angles, 10 radial projections are displayed. 84

6.2 Illustration of the effect of shifted projection angles on the streaking artifacts in the reconstructed image for a numerical phantom. The phantom was sampled using 10 radial projections, and the projection angles were shifted by $\frac{\pi}{2k}$ between the two reconstructions. This leads to changes in the structure of the streaking artifacts which can easily be seen by the orientation of the specific streak that is highlighted by the arrows. 84

6.3 A single slice from the data set of the phantom measurements using 64 (top row, $\lambda = 10$), 32 (middle row, $\lambda = 7$) and 24 (bottom row, $\lambda = 5$) shifted projections. Conventional NUFFT reconstruction (left) and reconstruction with the proposed 3D TV method. 88

6.4 A single slice from the angiography data set with 80 projections ($\lambda_{2DROF} = 0.03$, $\lambda_{2Dk\text{space}} = 0.35$, $\lambda_{3D} = 15$). Shown are original, fully sampled data set, conventional NUFFT reconstruction with zero filling, 2D slice by slice ROF TV filtering, TV reconstruction with data fidelity term in k -space, proposed 3D TV filtering using a conventional stack of stars trajectory, proposed 3D TV filtering using the shifted stack of stars trajectory 89

6.5 A single slice from the angiography data set with 40 projections ($\lambda_{2DROF} = 0.08$, $\lambda_{2Dk\text{space}} = 0.45$, $\lambda_{3D} = 10$). Shown are original, fully sampled data set, conventional NUFFT reconstruction with zero filling, 2D slice by slice ROF TV filtering, TV reconstruction with data fidelity term in k -space, proposed 3D TV filtering using a conventional stack of stars trajectory, proposed 3D TV filtering using the shifted stack of stars trajectory 90

List of Tables

2.1	Values of the TV penalty for the undersampled images from Figure 2.9.	35
3.1	Quantitative evaluation of GRAPPA reconstruction errors of the downsampling experiments with different sampling patterns. RMS differences (a.u.) to an SOS image from the original fully sampled data set are shown. The values are means with standard deviations over 10 different patterns for the same pdf.	44
3.2	Quantitative evaluation of the GRAPPA reconstruction errors of the experiments with different templates. RMS differences (a.u.) to an SOS image from the original fully sampled data set are shown. Means with standard deviations over 10 different patterns for the same pdf are shown.	45
4.1	CUDA Reconstruction times of experiments with radial subsampling. Data sets with 12 (Figure 4.7) and 32 (Figure 4.5) channels with different numbers of spokes were used.	64
6.1	Quantitative evaluation of the following reconstruction methods for the in vivo angiography data: Conventional NUFFT reconstruction with zero filling, 2D slice by slice ROF TV filtering, TV reconstruction with data fidelity in k -space, proposed 3D TV filtering using a conventional stack of stars trajectory, proposed 3D TV filtering using the shifted stack of stars trajectory that is introduced in this chapter. Mean value and standard deviation of RMS differences (a.u.) to the fully sampled data set for 40 slices are displayed using the 80 and 40 projections subsampled data.	91
6.2	Computation times of PDU 3D TV on the GPU for all tested data sets.	91

Chapter 1

Introduction

Magnetic Resonance Imaging (MRI) is nowadays considered to be the most important non-invasive diagnostic imaging modality for a wide range of common diseases like stroke, cancer and disorders of the cardiovascular system. Since the first experiments in the 1970s, the method has been refined continuously, and current MR systems deliver images of high quality for many applications. The key advantages of MRI are the excellent soft tissue contrast, which is superior to that of any other imaging modality, and the fact that, in contrast to computed tomography (CT), positron emission tomography (PET) or conventional X-Ray imaging, MRI does not use ionizing radiation. It has also been developed to a method which can be used to get functional or even metabolic information. This development is driven by the need for a better staging of diseases and characterization of disease subtypes or by applications in the field of treatment monitoring.

However, there are still a number of limitations in MRI. The strong main magnetic field prohibits the examination of patients with implants like pacemakers, and requires the use of dedicated medical devices in the vicinity of the MR-system. Ferromagnetic objects have to be handled with extreme care as there is the potential danger that they can turn into projectiles that can cause significant harm to patients, personnel and the MR-system itself. Another main challenge arises due to the long data acquisition times. This is especially a problem when patient movement occurs during a measurement. The sources of movement are numerous and include uncooperative or very young patients, but also motion due to breathing or the beating heart. The main reason for the lengthy data acquisition is that only a limited number of data points can be encoded from one MR signal (FID or echo) and the measurement has to be repeated for many times. This means that MR data is acquired sequentially (line by line) in frequency (k)-space. This is a fundamental difference in comparison to other imaging modalities, which always acquire complete images in one measurement step. As a consequence, increasing imaging speed has always been a major research area ever since the first experiments, and improvements in this field have contributed significantly to introduce new applications for MRI. In the past, research to accelerate MR imaging speed was mainly directed toward faster collection of data. However, in current MR systems, these developments have reached a state where further advances are not limited by technical challenges, but by fundamental physiological limits due to patient safety. One way to circumvent this problem is to increase imaging speed by reducing the number of

data points that are used to reconstruct an image with a defined resolution. However, as this approach violates the Nyquist-Shannon sampling theorem, aliasing artifacts are introduced in the reconstructions which have to be eliminated. This is only possible with the integration of additional a-priori information during the reconstruction process.

The development of Parallel Imaging [2–4], the use of multiple receiver coils to augment conventional data acquisition, has had a tremendous impact and is already used successfully in daily clinical practice during the last years. Accurate estimations of the coil sensitivities are vital for parallel imaging, and the investigation of new strategies to obtain sensitivity maps is a very active topic of current research. A promising new approach strategy is joint estimation of image content and sensitivity profiles [5–7]. Other successful strategies use spatiotemporal redundancies in image data sets [8–13]. In the last couple of years, a major advance was achieved with the introduction of nonlinear L1 based regularization methods to MRI image reconstruction. This approach leads to a more efficient elimination of noise, and as described by the recent theory of compressed sensing [14–17], the combination of incoherent sampling, a sparse representation in a transformation domain and nonlinear reconstruction can also be used to eliminate undersampling efficiently. The L1 penalty is also a natural link to the theory of Total Variation (TV) [18], which is already well known in image processing, but has also been introduced to MR image reconstruction recently [1, 19]. Latest developments also investigated the combination of Parallel Imaging and L1 regularization [1, 20].

1.1 Outline of the thesis

This thesis contributes to the field of image reconstruction for accelerated imaging. As described in detail in later chapters, image reconstruction can be treated as an inverse problem. This approach provides a general framework to incorporate a-priori knowledge about the spatial positions of the receiver coils or the structure of the solution, and allows to reformulate image reconstruction as a constrained optimization problem. With the methods presented in this thesis, MR data sets can be acquired up to 33 times faster than dictated by the Nyquist rate. This not only increases patient comfort and the throughput rate of radiology departments, it also opens the door for completely new MR procedures. Temporal resolutions of 38 milliseconds (corresponding to frame rates of approximately 26 frames per second) allow real-time visualization of the beating heart without the use of ECG triggering and respiratory bellows during free breathing, or imaging of the propagation of contrast agents in the vessel system (MR-fluoroscopy). The rapid scan times also lead to a significant reduction of motion artifacts, which are a very common problem in MRI, especially for cardiac imaging where very complex movement patterns arise due to heartbeat and breathing. In the following section, an outline of the thesis is provided.

Chapter 2 gives an overview of image reconstruction strategies for accelerated imaging.

Chapter 3 discusses the design of sampling patterns for accelerated imaging. The proposed approach uses tailored sampling patterns, derived from a-priori knowledge about the energy distribution in k -space. Undersampled data are reconstructed using the well known GRAPPA [4]

method. This chapter is based on the journal publication *Adapted Random Sampling Patterns for Highly Accelerated MRI* [21]. Individual author contributions to this paper were:

- Florian Knoll: Proposal of the basic idea, development of the adapted random sampling pulse sequence on the MR scanner system, MR measurements, raw data handling, image reconstruction, evaluation of the results, preparation of the manuscript.
- Christian Clason: Implementation of the method to draw samples from a pdf to obtain a sampling pattern, assistance in evaluation of the results and during preparation of the manuscript.
- Clemens Diwoy: Assistance in the development of the pulse sequence on the scanner system.
- Rudolf Stollberger: General assistance during all tasks, including methodological work, data acquisition and preparation of the manuscript.

Chapter 4 introduces the new concept of Total Generalized Variation (TGV) for MR image reconstruction. While the Total Variation (TV) has been applied successfully as a regularizer for image reconstruction, the main criticism of this approach is the fact that TV favors images with cartoon-like appearance, and introduces staircasing artifacts in regions with smooth signal changes. The work presented in this chapter aims to provide a solution for these issues. It is based on the paper *Second Order Total Generalized Variation (TGV) for MRI* [22], and individual author contributions were:

- Florian Knoll: Basic concept of the application of TGV to MRI, MR measurements, rawdata handling, image reconstruction, evaluation of the results, preparation of the manuscript.
- Kristian Bredies: Development of the mathematical framework of TGV including analytical foundations as well as numerical algorithms, preparation of the manuscript (especially for the section "Theory").
- Thomas Pock: Assistance in the development of TGV, in particular the numerical primal-dual algorithm, preparation of the manuscript (especially for the section "Numerical Algorithms").
- Rudolf Stollberger: General assistance during all tasks, including methodological work, data acquisition and preparation of the manuscript.

Chapter 5 introduces a general framework for nonlinear parallel imaging reconstruction by means of nonlinear inversion (IRGN-T(G)V). This approach enables joint estimation of image content and coil sensitivities, as first described in [6], but it also allows to include the same regularization terms that are described in chapter 4. It is based on the publication *Nonlinear Parallel Imaging with Variational Penalties* [23]. Individual author contributions were:

- Florian Knoll: Proposal of the underlying concept, MR measurements to obtain all Cartesian and randomly subsampled data sets, rawdata handling, image reconstruction, evaluation of the results, preparation of the manuscript.

- Christian Clason: Development of the mathematical framework of IRGN-TV, including analytical work and the primal-dual extra-gradient algorithm, preparation of the manuscript (especially section "Theory").
- Kristian Bredies: Assistance in the development of IRGN-TGV and during preparation of the manuscript.
- Martin Uecker: MR measurements to obtain the radial phantom and the radial real-time cardiac rawdata, assistance during preparation of the manuscript.
- Rudolf Stollberger: General assistance during all tasks, including methodological work, data acquisition and preparation of the manuscript.

The challenge of the presented approaches is the increase in computation time. While conventional MR image reconstruction can be performed by means of the fast Fourier transform (FFT), for the methods in this work, a solution of a constrained optimization problem has to be obtained. To allow the use of these strategies in daily clinical practice, reconstruction times have to be achieved that are not significantly longer than the data acquisition times. **Chapter 6** demonstrates that 3D-TV based elimination of artifacts from radial undersampling can be performed on commodity graphics hardware, with computation times that allow real-time interactive artifact removal for large 3D data sets. It is based on the journal publication *Fast reduction of undersampling artifacts in radial MR angiography with 3D total variation on graphics hardware* [24], with the following individual author contributions:

- Florian Knoll: Basic idea of the application of 3D-GPU-TV filtering to undersampled radial data, proposal and development of the radial shifted spokes trajectory, MR data acquisition, conduction of experiments with the 3D-TV method, evaluation of the results, preparation of the manuscript.
- Markus Unger: Implementation of the 3D-TV method on the GPU, preparation of the manuscript (especially for the sections concerning the TV filter and the GPU implementation).
- Clemens Diwok: Implementation of the shifted radial spokes trajectory on the MR scanner system.
- Christian Clason: Assistance during evaluation of the results and during preparation of the manuscript (especially concerning the TV method).
- Thomas Pock: Assistance in the implementation of the 3D-TV method on the GPU.
- Rudolf Stollberger: General assistance during all tasks, including methodological work, data acquisition and preparation of the manuscript.

Finally, a summary of the contributions of this work to the field of image reconstruction for accelerated imaging and future work based on the results of this thesis is given in **Chapter 7**.

One of the main aspects of this thesis is its interdisciplinarity. This does not come as a surprise, as contributions to the field of medical imaging have always been characterized by their

wide range of expertise, including work from basic scientists, engineers and clinical researchers. The most important scientific society in the field of MRI, the *International Society for Magnetic Resonance in Medicine* (ISMRM)¹ always strived for a confluence of basic science and clinical application. In fact, the motto of the upcoming annual meeting of the society², the major annual conference in the field, is “Clinical Needs and Research Promises: Bridging the gap”. In particular, this thesis is characterized by interdisciplinary work with mathematicians, as it is based on research conducted by the Special Research Program (Spezialforschungsbereich, SBF) “Mathematical Optimization and Applications in Biomedical Sciences”³. This is one of the excellence programs of the Austrian Science Fund⁴ (FWF) and is comprised of mathematicians, (medical) physicists and biomedical engineers. Additional collaboration was conducted with clinical partners from the local university hospital.

¹<http://www.ismrm.org/>

²<http://www.ismrm.org/11/index.htm>

³<http://math.uni-graz.at/mobis/>

⁴<http://www.fwf.ac.at/de/projects/sfb.html>

Chapter 2

MR Image Reconstruction

2.1 Spatial Signal Encoding and Image Reconstruction

The underlying physics necessary to understand the generation of the MR signal are complex and out of scope of this thesis. Details can be found in MRI textbooks [25, 26]. From the perspective of image reconstruction, the most important property is that data is acquired in frequency space (k -space), and spatial encoding is performed with the use of magnetic gradient fields. The MR-signal therefore looks as follows:

$$s(t, G_y) = \int_{-\infty}^{+\infty} \int_{-\infty}^{+\infty} \rho(x, y) e^{-i(\Phi(x, t) + \Phi(y, G_y))} dx dy \quad (2.1)$$

The phase of the signal can be described by the following relations:

$$\Phi(y, G_y) = -\gamma y \int_0^T G_y d\tau \quad (2.2)$$

$$\Phi(x, t) = -\gamma x \int_0^t G_x d\tau \quad (2.3)$$

With the notation:

$$\Phi(y, G_y) = -\gamma y \int_0^T G_y d\tau \equiv k_y y \quad (2.4)$$

$$\Phi(x, t) = -\gamma x \int_0^t G_x d\tau \equiv k_x x, \quad (2.5)$$

the fundamental MR signal equation looks as follows:

$$s(k_x, k_y) = \int_{-\infty}^{+\infty} \int_{-\infty}^{+\infty} \rho(x, y) e^{-i(k_x x + k_y y)} dx dy \quad (2.6)$$

In equations 2.1 to 2.6, G_x is the frequency encoding gradient, G_y is the phase encoding gradient, T is the time interval the phase encoding gradient is turned on, γ is the gyro magnetic ratio and ρ is the underlying spin density.

It can be observed instantly from equation 2.6 that this signal equation is of the form of a two dimensional Fourier transform, which means that the underlying spin density can be reconstructed with the use of an inverse Fourier transform. The sampling positions k_x and k_y are defined by the k -space trajectory. Figures 2.1 and 2.2, which originally appeared in [27], illustrate k -space trajectories and corresponding spin echo pulse sequence diagrams of two popular sampling patterns. Cartesian sampling, which is currently the backbone of all MR examinations in clinical practice, and radial sampling, which was used in the original formulation of MR image encoding [28] and is having a revival recently due to advances in MR instrumentation. Radial sampling is discussed in more detail in chapters 4, 5 and 6, and detailed assessment of state-of-the-art radial sampling can be found in [19]. In Figures 2.1 and 2.2, RF is the radio frequency pulse that is used to excite the spins, and TE is the echo time (again, details can be found in MR textbooks). This also illustrates the sequential character of MR data acquisition. In conventional pulse sequences as shown here, each line in k -space is acquired after a new excitation pulse, the time interval between subsequent pulses being the repetition time TR. It can therefore be seen instantly that the time that is needed to obtain a complete MR data set is proportional to the number of lines that have to be acquired.

To encode a 3D volume of interest, two strategies are possible. The first is to excite multiple individual slices and perform 2D image image encoding as described above. The alternative is to extend the concept of phase encoding to the third dimension. Image reconstruction is then performed with a 3D inverse Fourier transform. The latter approach allows great flexibility in spatial encoding. For example, in the case of radial imaging, it is possible to perform radial sampling in the x, y dimension and conventional Cartesian encoding in the z direction, an approach that is commonly known as a stack of stars acquisition. However, it is also possible to extend the radial sampling pattern to full 3D [29]. In the case of Cartesian sampling, 3D encoding allows to select arbitrary sampling points in the y, z plane (the plane of the two phase encoding directions). This was an important prerequisite for the exciting new field of compressed sensing in MRI [16], as it allowed the generation of randomized sampling patterns. A detailed discussion of random sampling is given in chapter 3.

2.2 k -space Sampling

In real MR experiments, the k -space signal is always acquired in discretized form. Therefore the discrete Fourier transform (DFT) is used for image reconstruction. In this section, it is assumed that the MR-signal is sampled at equidistant intervals Δk_x (reconstruction of data from non-Cartesian sampling trajectories is covered in section 2.6), and for simplicity only 1D sampling is considered. All relaxation effects are also neglected, which means that the reconstructed image is a direct representation of the underlying physical spin density. Of course, it is not possible to obtain an infinite number of sample points, but it is instructive to consider the situation of infinite discrete k -space sampling first, and then move on to finite sampling as the next step. A more extensive coverage of the effect of discrete k -space sampling is given in MRI textbooks [26, 30].

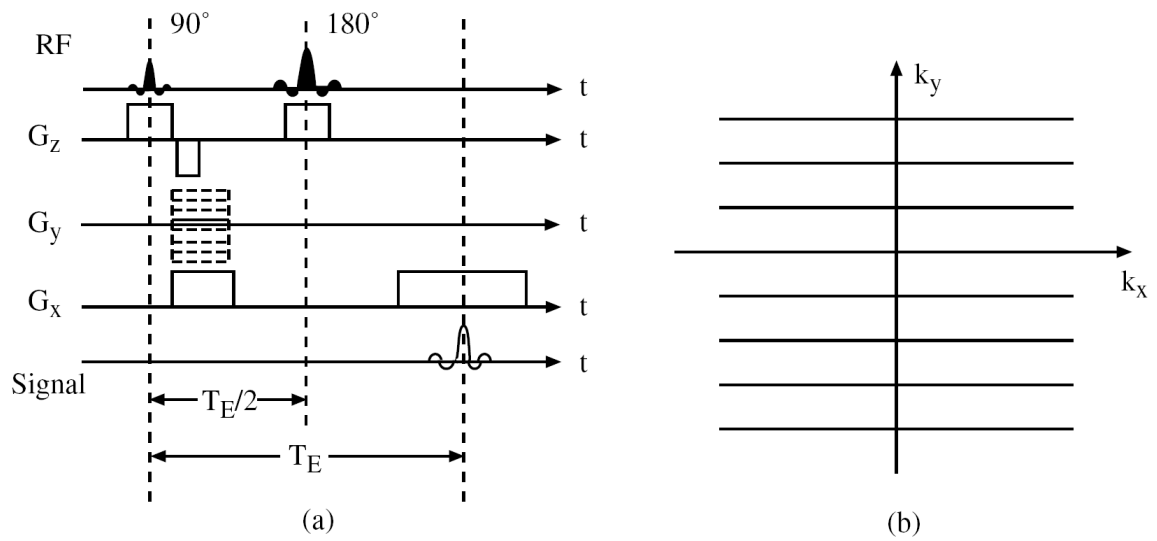


Figure 2.1: Cartesian spin echo sampling: The pulse sequence (a) and the corresponding k -space trajectory (b) are displayed.

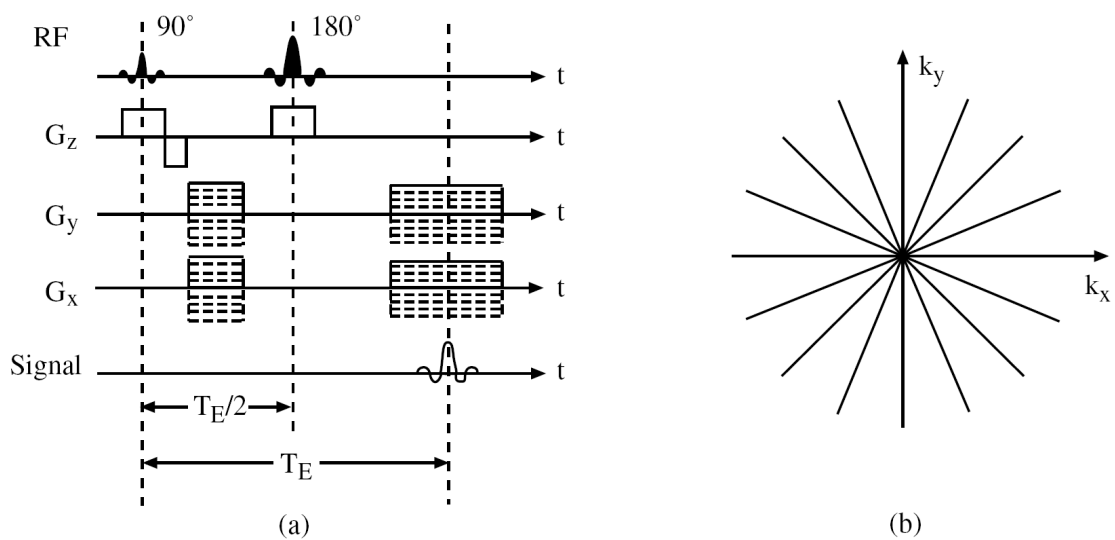


Figure 2.2: Radial spin echo sampling: The pulse sequence (a) and the corresponding k -space trajectory (b) are displayed.

2.3 Infinite Discrete k -space Sampling

In the following, the m 'th step of 1D k -space, sampled in the k_x dimension, is denoted by $\hat{s}(m\Delta k_x)$. In a real-world multi dimensional MR data acquisition, $s(k_x)$ corresponds to a single readout line in frequency encoding direction. Mathematically, the sampling step which results in a discrete but infinite signal $\hat{s}_\infty(k_x)$, can be formulated as a multiplication of the original continuous signal $s(k_x)$ with a sampling function $\phi_\infty(k_x) = \Delta k_x \sum_{m=-\infty}^{+\infty} \delta(k_x - m\Delta k_x)$ which consists of an infinite series of equidistant Dirac delta functions.

$$\hat{s}_\infty(k_x) = s(k_x) \cdot \phi_\infty(k_x) = \Delta k_x \sum_{m=-\infty}^{+\infty} s(m\Delta k_x) \cdot \delta(k_x - m\Delta k_x). \quad (2.7)$$

The corresponding reconstructed (1D) spin density $\hat{\rho}_\infty(x)$ is obtained with an inverse Fourier transform.

$$\hat{\rho}_\infty(x) = \int_{-\infty}^{+\infty} \hat{s}_\infty(k_x) \cdot e^{ik_x x} dk_x = \Delta k_x \sum_{m=-\infty}^{+\infty} s(m\Delta k_x) \cdot e^{im\Delta k_x x}. \quad (2.8)$$

It is instructive to make use of the Fourier convolution theorem to get additional insights in these operations (see Figure 2.3 for a visual representation). The reconstructed spin density $\hat{\rho}_\infty(x)$ can be obtained by a convolution of the original underlying physical spin density with the inverse Fourier transform of the sampling function $\phi_\infty(k_x)$, denoted by $\Phi_\infty(x)$.

$$\hat{s}_\infty(k_x) = s(k_x) \cdot \phi_\infty(k_x) \quad \bullet \text{---} \circ \quad \hat{\rho}_\infty(x) = \rho(x) \star \Phi_\infty(x). \quad (2.9)$$

The inverse Fourier transform of an infinite series of equidistant Dirac delta functions with spacing Δk_x is another series of equidistant delta functions with spacing $\frac{2\pi}{\Delta k_x}$, which is called the imaging Field of View FOV :

$$\Phi_\infty(x) = \sum_{l=-\infty}^{+\infty} \delta\left(x - l \frac{2\pi}{\Delta k_x}\right). \quad (2.10)$$

This leads to the following result for the reconstructed spin density:

$$\hat{\rho}_\infty(x) = \sum_{l=-\infty}^{+\infty} \rho\left(x - l \frac{2\pi}{\Delta k_x}\right), \quad (2.11)$$

which means that the reconstructed spin density $\hat{\rho}_\infty(x)$ is a periodic repetition of the original underlying spin density $\rho(x)$ with spacing $\frac{2\pi}{\Delta k_x}$. If the Field of View is larger than the length of the object

$$FOV > L \quad \Leftrightarrow \quad \Delta k_x < \frac{2\pi}{L} \quad (2.12)$$

in the corresponding dimension, the reconstructed spin densities $\hat{\rho}_\infty(x)$ do not overlap. Equation 2.12 is the well known Nyquist-Shannon sampling theorem. If Δk_x is chosen too large (which corresponds to a FOV that is too small), the sampling theorem is violated and aliasing occurs. This is covered in more detail in section 2.5.

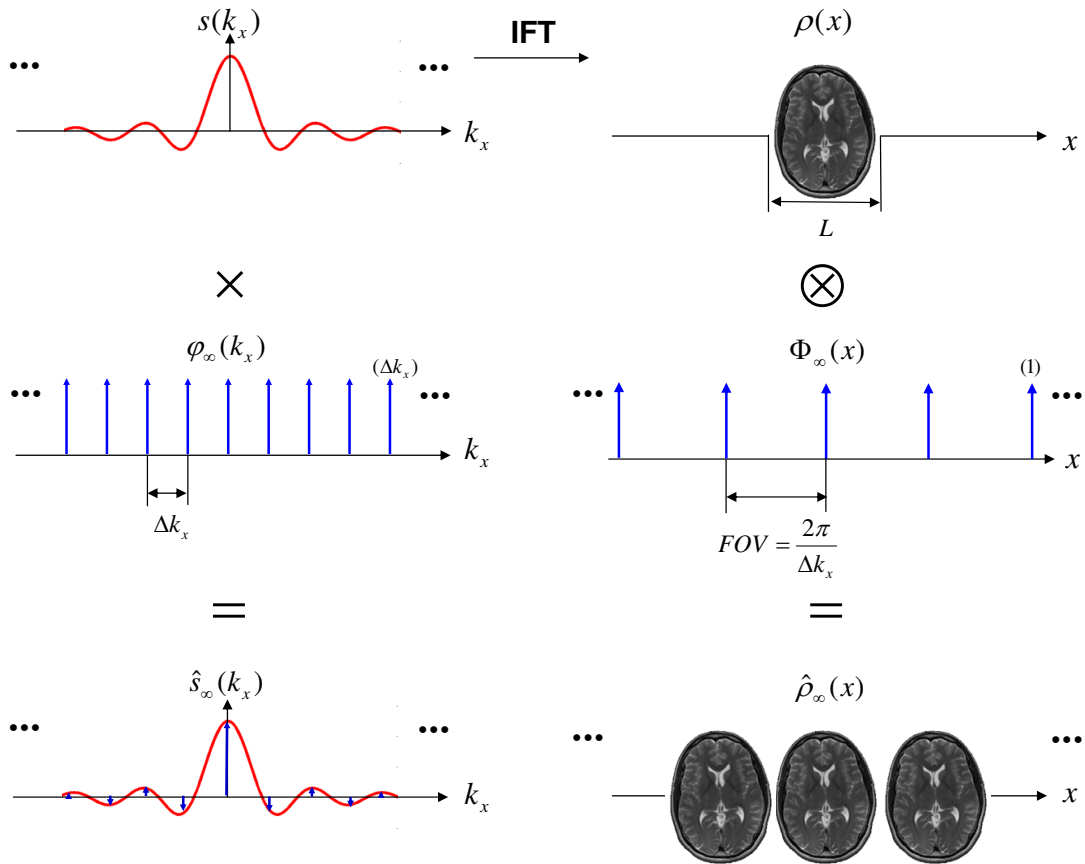


Figure 2.3: Illustration of the effects of discrete infinite sampling of the MR signal $s(k_x)$ on the reconstructed spin density (corresponding to the reconstructed image). Sampling, which results in a discrete but infinite signal $\hat{s}_\infty(k_x)$, can be formulated as a multiplication of the original continuous signal $s(k_x)$ with a sampling function $\phi_\infty(k_x)$, which is comprised of an infinite series of equidistant Dirac delta functions (left column). With the use of the Fourier convolution theorem, it can be shown that this operation is equivalent to a convolution of the original underlying physical spin density $\rho(x)$ with $\Phi_\infty(x)$, the inverse Fourier transform of the sampling function, which is another infinite series of Dirac delta functions with spacing $FOV = \frac{2\pi}{\Delta k_x}$ (right column). If the length of the object L is smaller than the FOV , the sampling theorem (equation 2.12) is fulfilled and the reconstructed images do not overlap.

2.4 Discrete Finite k -space Sampling

In the previous section, it was assumed that an infinite number of discrete sample points are obtained from the the continuous MR signal $s(k_x)$. In practice, sampling is performed only during a limited time, which means that the data points are truncated. Mathematically, this can be expressed as a multiplication of the infinite discrete sample points \hat{s}_∞ with a rectangular window function $w(k_x)$, which keeps $N = 2n$ sample points:

$$\hat{s}(k_x) = \underbrace{s(k_x) \cdot \phi_\infty(k_x)}_{\hat{s}_\infty(k_x)} \cdot w(k_x) = \Delta k_x \sum_{m=-n}^{n-1} s(m\Delta k_x) \cdot \delta(k_x - m\Delta k_x). \quad (2.13)$$

Again, the spin density $\hat{\rho}$ is reconstructed by means of an inverse Fourier transform:

$$\hat{\rho}(x) = \int_{-\infty}^{+\infty} \hat{s}(k_x) \cdot e^{ik_x x} dk_x = \Delta k_x \sum_{m=-n}^{n-1} s(m\Delta k_x) \cdot e^{im\Delta k_x x}. \quad (2.14)$$

Similar to case of infinite sampling, insight in the effects of this operation on the reconstruction result can be obtained with the use of the Fourier convolution theorem:

$$\hat{s}(k_x) = s(k_x) \cdot \phi_\infty(k_x) \cdot w(k_x) \quad \bullet \text{---} \circ \quad \hat{\rho}(x) = \underbrace{\rho(x) \star \Phi_\infty(x)}_{\hat{\rho}_\infty(x)} \star W(x). \quad (2.15)$$

$W(x)$ is the inverse Fourier transform of the rectangular window function $w(k_x)$, which is known to be a *sinc* function. The reconstructed spin density $\hat{\rho}_\infty(x)$, which is already replicated due to discrete sampling, is additionally convolved with $W(x)$. This leads to blurring and Gibb's ringing artifacts in the final reconstruction $\hat{\rho}(x)$. This is illustrated in Figure 2.4.

In a real world measurement, where the output of the system is a digital image, the reconstruction $\hat{\rho}(x)$ is also discretized with a spacing of Δx , and truncated to the imaging field of view $N \cdot \Delta x$ (N being the number of sample points in the reconstruction). This means that the relation of $s(m\Delta k_x)$ and $\hat{\rho}(q\Delta x)$ is the discrete Fourier transform pair:

$$s(m\Delta k_x) = \Delta x \sum_{q=-n}^{n-1} \hat{\rho}(q\Delta x) \cdot e^{-im\Delta k_x q\Delta x} \quad (2.16)$$

$$\hat{\rho}(q\Delta x) = \Delta k_x \sum_{m=-n}^{n-1} s(m\Delta k_x) \cdot e^{im\Delta k_x q\Delta x}. \quad (2.17)$$

2.5 Aliasing

If the *FOV* is chosen too small with respect to the imaged object (which is equivalent to a Δk_x that is too large), this means that the sampling theorem 2.12 is violated, and aliasing occurs. This is illustrated in Figure 2.5, where the spacing Δk_x^A of the sampling function $\Phi_\infty^A(k_x)$ is increased by a factor of 2. As a consequence, the $FOV^A = \frac{2\pi}{\Delta k_x^A}$ is halved, and now smaller than the length of the imaged object L . The periodic replicates $\hat{\rho}_\infty^A(x)$ of the spin density $\rho(x)$ overlap, and cannot be separated from each other anymore.

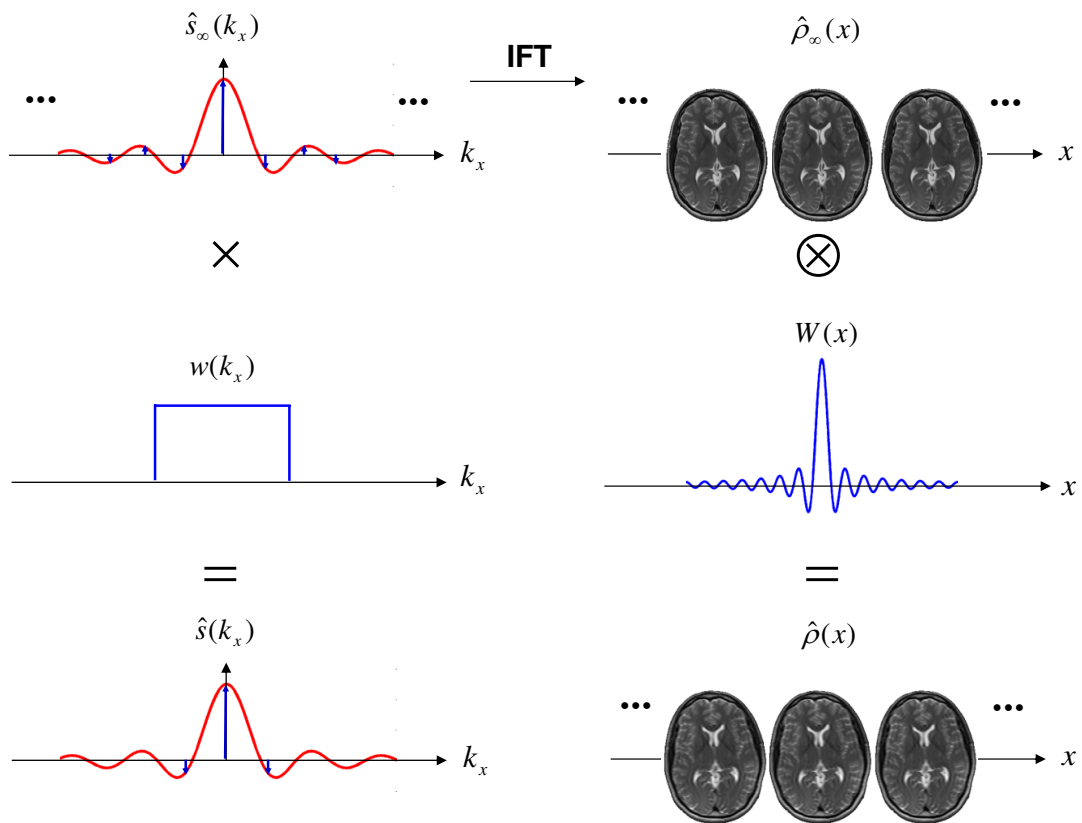


Figure 2.4: In real world MR-measurements, only a finite number of samples are acquired. This can be expressed as a multiplication with a rectangular window function $w(k_x)$, keeping $N = 2n$ sample points (left column). With the use of the Fourier convolution theorem, it can be shown that this operation is equivalent to a convolution of the reconstructed spin density $\hat{\rho}_\infty(x)$ with $W(x)$, the inverse Fourier transform of the rectangular window function $w(k_x)$, which is a *sinc* function (right column). This leads to blurring and Gibb's ringing artifacts in the final reconstruction $\hat{\rho}(x)$.

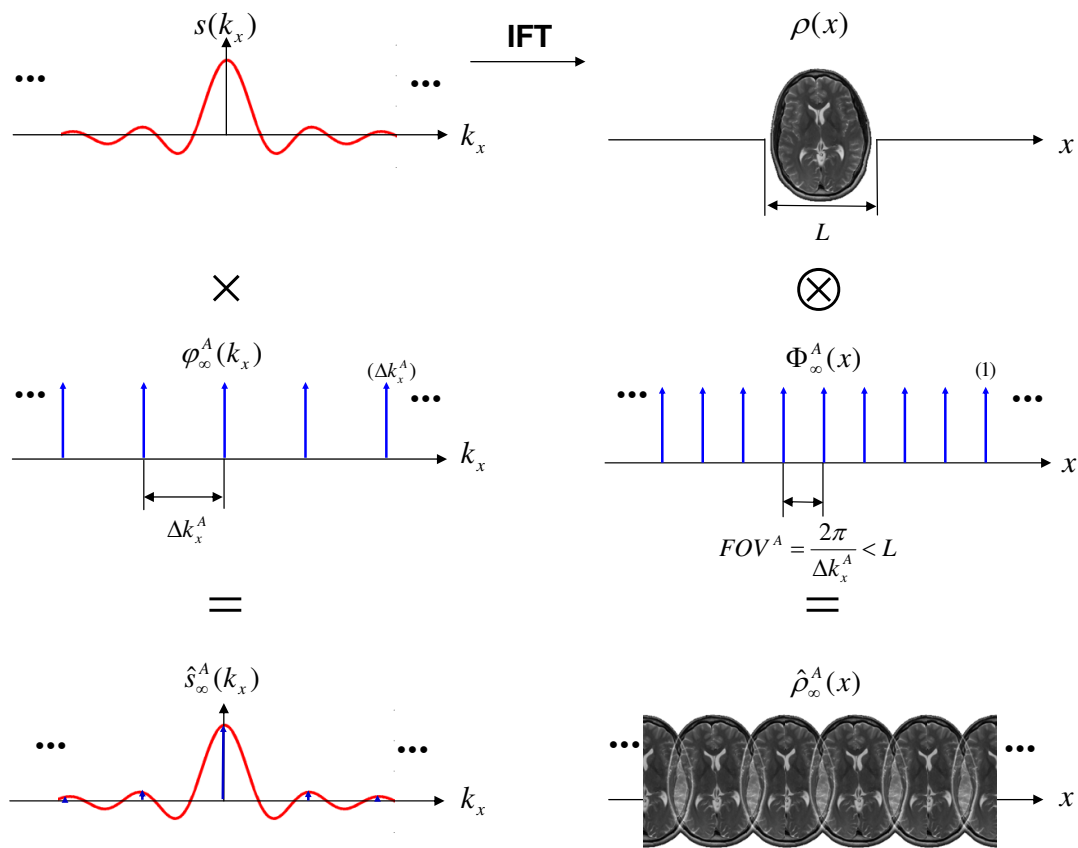


Figure 2.5: Illustration of the effect of aliasing: The spacing Δk_x^A of the sampling function $\Phi_\infty^A(k_x)$ is increased by 2. The $FOV^A = \frac{2\pi}{\Delta k_x^A}$ is halved, and $L > FOV$. The periodic replicates $\hat{\rho}_\infty^A(x)$ overlap, and cannot be separated from each other anymore.

In accelerated imaging, which is covered in detail in section 2.7, Δk is deliberately increased in phase encoding direction. The reason is that this reduces the number of phase encoding steps needed for a given resolution and therefore leads to a reduction of scan time of the factor R , which is called the subsampling- or acceleration factor. The aliasing artifacts, which occur due to the violation of the sampling theorem are then removed with special strategies during the image reconstruction process.

2.6 Reconstruction of non-Cartesian data

The treatment in the previous sections assumed that data points are sampled equidistantly and on a Cartesian grid. While this assumption is valid in the case of a conventional Cartesian sampling pattern, it was mentioned in section 2.1 that in principle, arbitrary trajectories can be used for data acquisition. In these cases, data points have to be interpolated to a Cartesian grid before the application of the inverse Fourier transform. This principle is called regridding and was first described for CT image reconstruction in 1985 [31]. Many refinements and adjustments for MR image reconstruction were published since then (e.g. [32–34]).

The sampled non-Cartesian data has to be convolved with a so called regridding kernel. To interpolate the data points on a rectangular grid, the results of this convolution are evaluated at $n \times n$ grid points with a spacing Δk . An optimal kernel window for interpolation in k -space is an infinite *sinc* function because the corresponding multiplication with a rectangular function does not distort the reconstructed image. However, as a convolution with an infinite kernel window is not feasible in practice, a kernel with compact support has to be used. A systematic assessment of the performance of different kernel windows can be found in [34, 35]. Based on these results, the Kaiser-Bessel window [36] is now used as a de-facto standard in MR imaging. For simplicity of notation, the following description of the gridding algorithm is restricted to the 1D case. Similar to the previous sections, generalization to higher dimensions is straight forward. In the figures that are included to illustrate the concepts the 2D case, most commonly used in practical imaging settings, is shown.

If the regridded Cartesian k -space data is denoted by $\hat{s}_c(k)$, the original non-Cartesian data by $\hat{s}_{nc}(k_j)$, and $\Gamma(k)$ is the convolution kernel, this operation can be written as:

$$\hat{s}_c(k) = \sum_j \hat{s}_{nc}(k_j) \cdot \Gamma(k - k_j) = \hat{s}_{nc}(k_j) \star \Gamma(k), \quad (2.18)$$

where k is the k -space index on the Cartesian grid (k_x, k_y in the 2D case) and k_j denotes an arbitrary (not equidistantly sampled and not on a Cartesian grid) k -space position. Please note that \star denotes the discrete convolution in equation 2.18. Of course the regridding method can also be described formally for the continuous case. However, in the case of continuous data instead of sampled data, the data could just be resampled to the Cartesian sample points without the convolution step.

An important issue arises due to the fact that non-Cartesian data can be acquired with a varying sampling density. For example, the data points in radial sampling (Figure 2.2) are acquired with a significantly higher density in the central parts of k -space. If this is not accounted for, it leads to images with a pronounced overweighting of low k -space frequencies. As the

spatial positions of the sample points cannot be determined any more after the convolution, compensation of the variable sampling density has to be performed as an initial step. Each sample point has to be weighted with a density compensation function $DCF(k_j)$, which is a measure of the inverse of the k -space sampling density.

$$\hat{s}_{c-dc}(k) = (DCF(k_j) \cdot \hat{s}_{nc}(k_j)) \star \Gamma(k). \quad (2.19)$$

In equation 2.19, $\hat{s}_{c-dc}(k)$ denotes regridded Cartesian k -space data that was obtained from density compensated non-Cartesian data. A reconstructed 1D image signal $\hat{\rho}_{dc}(x)$ from density compensated and regridded data can then be obtained by means of an inverse discrete Fourier transform (\mathcal{F}^{-1}).

$$\hat{\rho}_{dc}(x) = \mathcal{F}^{-1} \{ (DCF(k_j) \cdot \hat{s}_{nc}(k_j)) \star \Gamma(k) \}. \quad (2.20)$$

In general, numerical estimations are needed to estimate the sampling density. The most widely used approach in MR image reconstruction is the Voronoi diagram [32,37]. In the special case of radial sampling, it is also possible to find an analytical representation of the sampling density, which leads to the Ram-Lak filter [38]. A radial sampling trajectory (256 radial spokes, 384 sample points on each spoke, corresponding to an oversampling ratio of 1.5 in the readout direction) and its corresponding density compensation function are shown in Figure 2.6. The effect of density compensation is illustrated in Figure 2.7. It shows radial k -space data of a T2 weighted data set of the brain, obtained with the sampling trajectory of Figure 2.6. In addition, the result of the convolution operation which interpolates the data points on a Cartesian grid and the reconstructed image after the application of an inverse Fourier transform are shown. All of these steps are performed for both the original radial data, and for density compensated data, using the DCF from Figure 2.6. The reduced signal intensity in the center of k -space can be observed for both radial and regridded data. Overweighting of low frequencies due to the absence of density compensation yields a significantly blurred image.

After the convolution interpolation, the regridded data is transformed back to image space by means of a conventional inverse discrete Fourier transform. However, due to the convolution with a finite kernel window, the reconstructed image is multiplied with the inverse Fourier transform of the kernel window $\Gamma(k)$, which leads to undesired intensity modulations. This effect can be compensated for by dividing the reconstructed image by the inverse Fourier transform of the regridding kernel (denoted by $\gamma(x)$), which is usually called deapodization or roll-off correction, and results in a final reconstructed image $\hat{\rho}_{dc-deapod}(x)$.

$$\hat{\rho}_{dc-deapod}(x) = \hat{\rho}_{dc}(x) \cdot \frac{1}{\gamma(x)}. \quad (2.21)$$

This is illustrated in Figure 2.8, which shows the reconstructed image from Figure 2.7 before and after deapodization, as well as horizontal cross-sectional plots through the central row (128) of the image matrix. The intensity modulation results in a dampening of the outer parts of the reconstructed image which is corrected with the deapodization procedure.

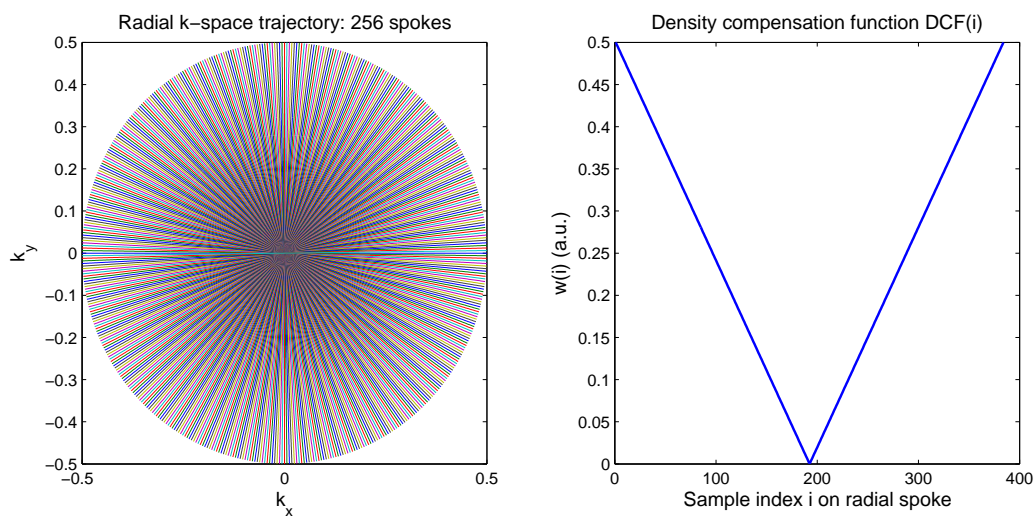


Figure 2.6: Radial sampling trajectory with 256 radial spokes and 384 sample points on each spoke, corresponding to an oversampling ratio of 1.5 in the readout direction. The k -space coordinates are normalized and range from -0.5 ($-k_{max}$) to $+0.5$ ($+k_{max}$) (left). Corresponding density compensation function (DCF). Note that the minimum of the DCF corresponds to the center of k -space where all radial spokes intersect. However, the minimum value does not reach zero, as this would result in a complete elimination of the signal at the center of k -space. In this example, the minimum value of the DCF is 0.0013 (right).

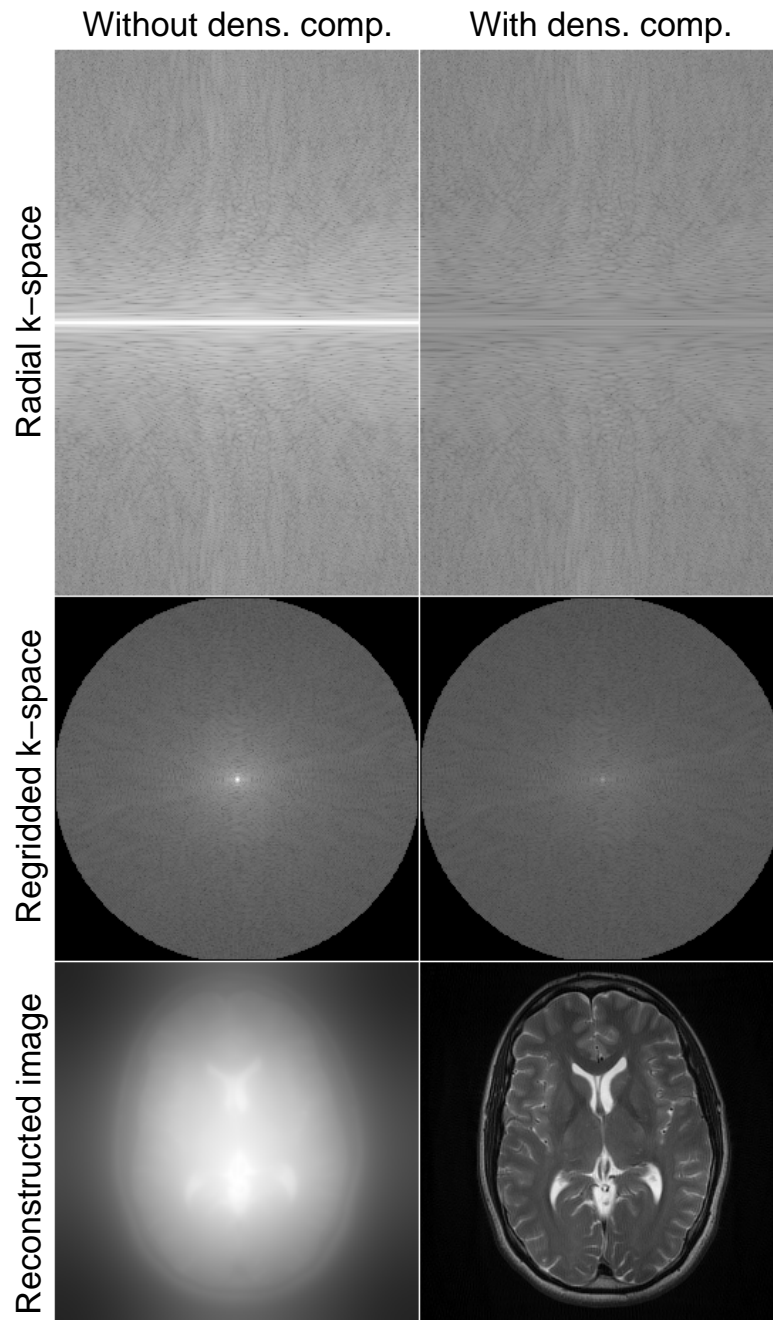
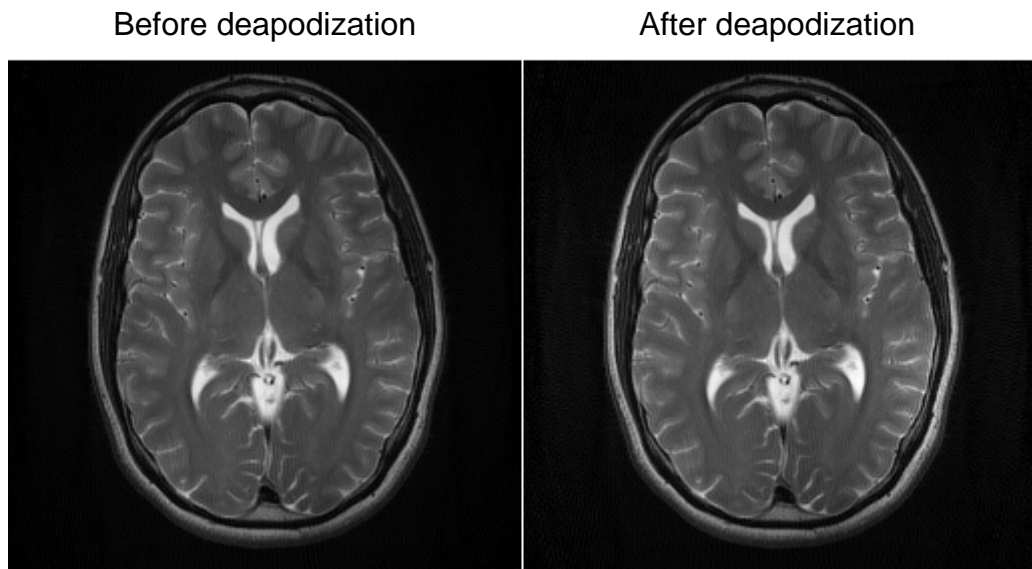
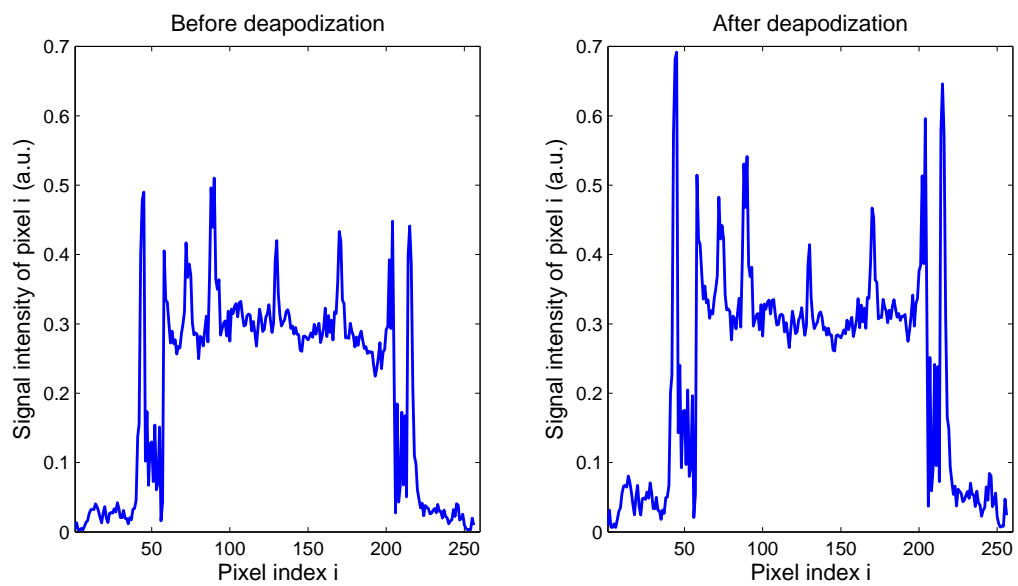


Figure 2.7: Radial k -space data obtained with the sampling trajectory of Figure 2.6 with 256 radial spokes, each consisting of 384 sample points (each spoke is one column in the data matrix) (top row), the result of the convolution operation which interpolates the data points on a Cartesian grid (middle row), and the reconstructed image after the application of an inverse Fourier transform (bottom row). These steps are performed for both the original radial data (left column), and for density compensated data (right column), using the DCF from Figure 2.6. The reduced signal intensity in the center of k -space can be observed for both radial and regridded data. In the absence of density compensation, the effect of overweighting of the low frequencies yields a significantly blurred image.



(a) Reconstructed images.



(b) Cross-section plots.

Figure 2.8: Reconstructed image from regridded k -space data (Figure 2.7) before and after deapodization (a), and horizontal cross-section plots through the central row (128) of the image matrix (b).

2.7 Parallel Imaging

2.7.1 Introduction

The key idea of parallel imaging is to complement spatial signal encoding of gradient fields with information about the spatial position of multiple receive coils, which record signals from the imaged object in parallel. With this approach, k -space data acquisition can be accelerated by means of undersampling. As this violates the sampling theorem (equation 2.12) aliasing artifacts are introduced in the images (see section 2.5). The specific structure of the artifacts depends on the used sampling trajectory. This is illustrated in Figure 2.9 for a T2 weighted data set of the brain. Cartesian subsampling is performed with acceleration factor $R = 2$ in the row dimension, $R = 4$ in the row dimension and $R = 2$ in both row and column dimension (resulting in a total acceleration of $R = 4$). In the case of radial sampling, 256, 128, 64 and 32 projections were used to reconstruction a 256×256 image. As $N \cdot \frac{\pi}{2}$ spokes have to be obtained to fulfill the Nyquist-Shannon sampling theorem in the case of radial sampling [26], this corresponds to acceleration factors of $R \approx 1.57$, $R \approx 3.14$, $R \approx 6.28$ and $R \approx 12.57$. It can be observed that subsampled Cartesian imaging leads to backfolding artifacts, while subsampling of radial trajectories yields images with streaking artifacts. It is also noticeable that while radial sampling appears to be less efficient than Cartesian sampling because $\frac{\pi}{2}$ times more sample points are needed to satisfy the Nyquist criterion, radial sampling is far more benign toward moderate undersampling. The reconstruction from 256 projections is in fact free of artifacts, and even the case of 128 projections, which already corresponds to an undersampling rate of 2 in comparison to a fully sampled Cartesian scan, is only mildly corrupted by streaking artifacts.

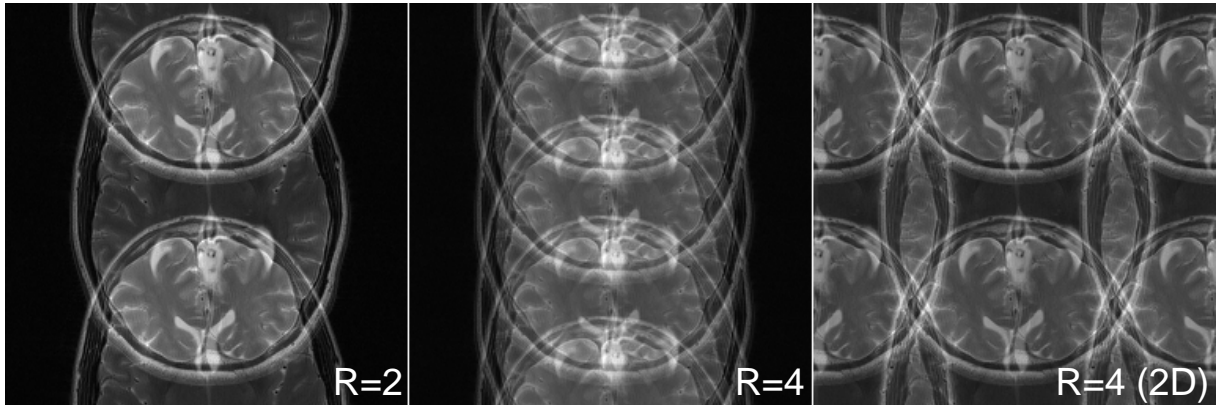
The idea to use information about the spatial position of multiple receive coils as an additional way of spatial encoding dates back to the time when the first phased array coils [39] were introduced [40]. However, it took another 10 years until the famous algorithms SMASH [2], SENSE [3] and GRAPPA [4] were developed. This paved the way for parallel imaging in clinical applications, where they are used every day nowadays. The most extreme case of parallel imaging is known under the name Inverse MRI [41], where gradient encoding in the phase encoding direction is completely replaced with encoding from coil sensitivities.

A large number of practical approaches exist to tackle the parallel imaging reconstruction problem. Sections 2.7.4 and 2.7.5 present SENSE [3] and GRAPPA [4], the two most widely used methods in clinical practice, is given. More detailed revisions of parallel imaging methods can be found in the literature [42–45].

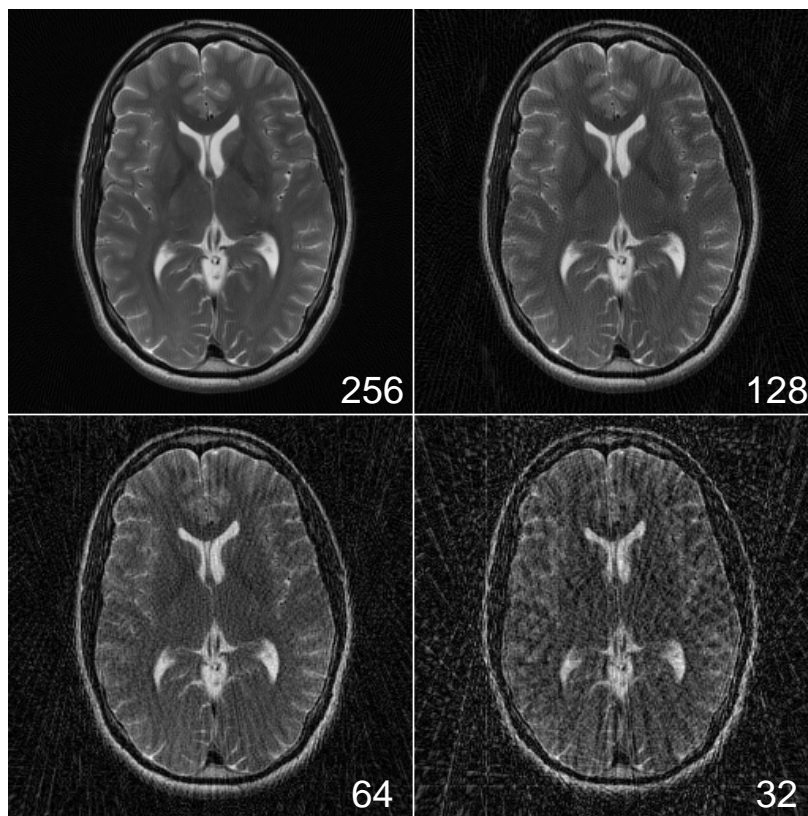
2.7.2 Phased array coils

Phased array coils [39] were originally designed to increase the SNR of MR measurements. They consist of multiple small coil elements and each single coil covers only a small part of the total (FOV). The individual signals from the coils are then combined to a single image of the complete FOV. Equation 2.6 can be generalized to include data acquisition with multiple receive coils:

$$s_k(k_x, k_y) = \int_{-\infty}^{+\infty} \int_{-\infty}^{+\infty} \rho(x, y) c_k(x, y) e^{-i(k_x x + k_y y)} dx dy. \quad (2.22)$$



(a) Cartesian subsampling with acceleration factor $R = 2$ in the row dimension (left), $R = 4$ in the row dimension (middle) and $R = 2$ in both row and column dimension, resulting in a total acceleration of $R = 4$.



(b) Radial subsampling with 256, 128, 64 and 32 projections to reconstruct a 256×256 image, corresponding to acceleration factors of $R \approx 1.57$, $R \approx 3.14$, $R \approx 6.28$ and $R \approx 12.57$.

Figure 2.9: Examples of subsampling with different sampling trajectories.

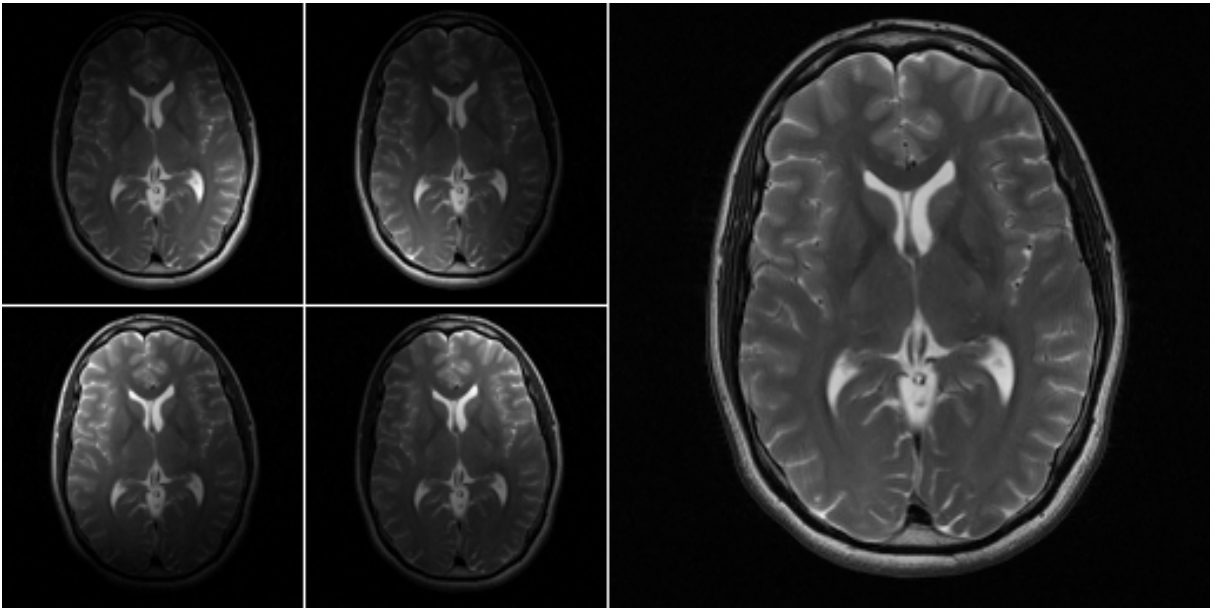


Figure 2.10: An example of a measurement with a 4 channel head coil. The images from the individual coil elements, as well as a sum of squares (SOS) combination, are displayed.

In equation 2.22, s_k is the MR signal of coil k , and c_k is the corresponding coil sensitivity. It is known that an optimal combination of the individual coil signals in terms of SNR is achieved with a pixel by pixel summation of the signals from each coil element, weighted by the corresponding coil sensitivities at the location of the pixels [46,47]. However, this approach requires an accurate estimation of the coil sensitivities, which is often not available. A pragmatic alternative, which is used most of the time during routine applications, is the root mean sum of squares (SOS) combination of individual coil images $\hat{\rho}_k$ after the inverse Fourier transform. This approach is described in equation 2.23, where K is the total number of coil elements. Figure 2.10 displays the images from the individual coil elements of a 4 channel head coil, and the corresponding SOS combination.

$$\hat{\rho}_{SOS} = \sqrt{\sum_{k=1}^K |\hat{\rho}_k|^2} \quad (2.23)$$

2.7.3 Array Coil Compression

State-of-the-art experimental MR systems are equipped with up to 128 receiver channels and corresponding receive coils [41,48]. An increase of coil elements yields images with higher SNR and, if the individual coils measure independent information, allows the use of higher acceleration factors. The drawback is the enormous increase in data that has to be processed during the measurements. This lead to the development of coil compression strategies. In this work, a method based on singular value decomposition (SVD) is used to reduce redundant data. An equivalent formulation can be obtained by means of principal component analysis (PCA) [49].

If D is the measured MR data of a single slice from all channels, arranged in a two dimensional matrix with dimensions $M \times N_c$, where M is the product of phase encoding steps and frequency

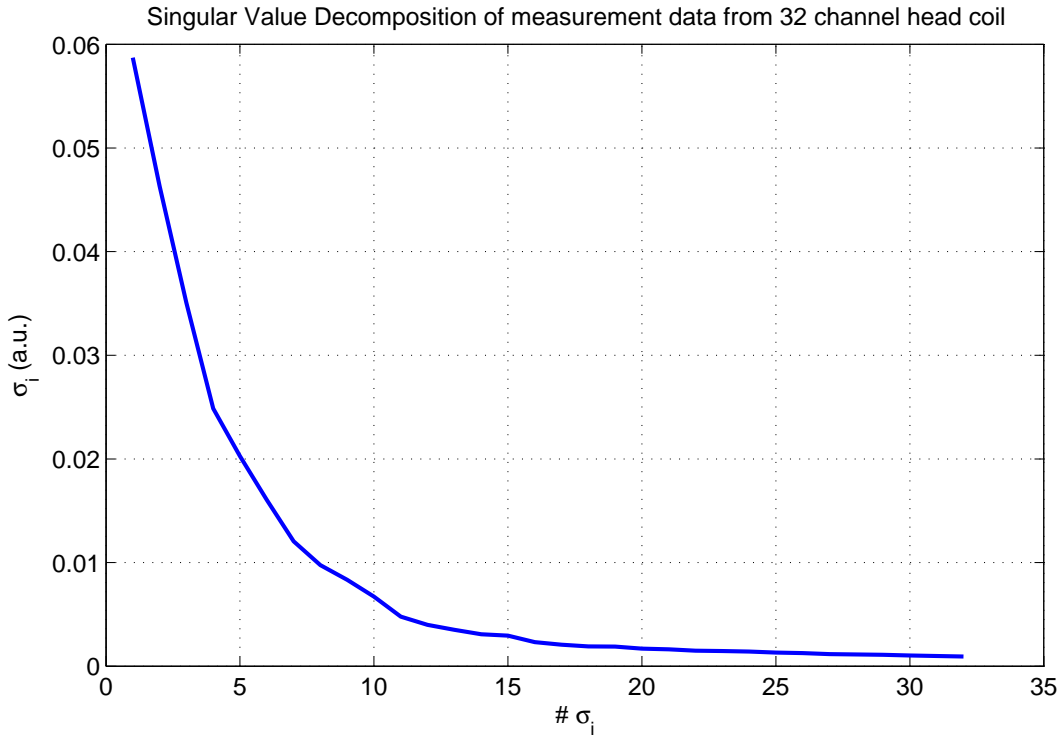


Figure 2.11: Plot of the singular values of the SVD decomposition of MR data from a 32 channel head coil.

encoding steps and N_c is the number of receiver channels, this matrix D can be decomposed in the form

$$D = U\Sigma V^H, \quad (2.24)$$

where U is a unitary $M \times M$ matrix, V^* is a unitary $N_c \times N_c$ matrix (V^H denoting the conjugate transpose of V), and Σ is an $M \times N_c$ diagonal matrix. The diagonal entries of Σ , $\Sigma_{ii} = \sigma_1, \dots, \sigma_{\min(M, N_c)}$ are the singular values that are uniquely determined by D . A plot of the singular values of the SVD decomposition of MR data with matrix size 256×256 from a 32 channel head coil is shown in Figure 2.11.

A well known compression approach that is also used in dimension reduction, e.g. for the problem of feature extraction in machine learning, is to truncate the singular values after a defined threshold τ :

$$(\hat{\Sigma}^\tau)_{ii} = \begin{cases} (\Sigma)_{ii} & (\Sigma)_{ii} \geq \tau \cdot \max(\Sigma)_{ii} \\ 0 & \text{otherwise.} \end{cases} \quad (2.25)$$

If Σ^τ is a truncation of $(\hat{\Sigma}^\tau)_{ii}$, including only the $M \times N_c^\tau$ non-zero elements, and $(V^\tau)^H$ is a corresponding truncation, selecting only the upper left $N_c^\tau \times N_c^\tau$ elements of V^H , compressed data D^τ is then obtained by

$$D^\tau = U\Sigma^\tau(V^\tau)^H. \quad (2.26)$$

Figure 2.12 shows a comparison of a reconstructed T2 weighted image of the brain using all original 32 channels to an SVD compression using only 10 virtual channels corresponding to

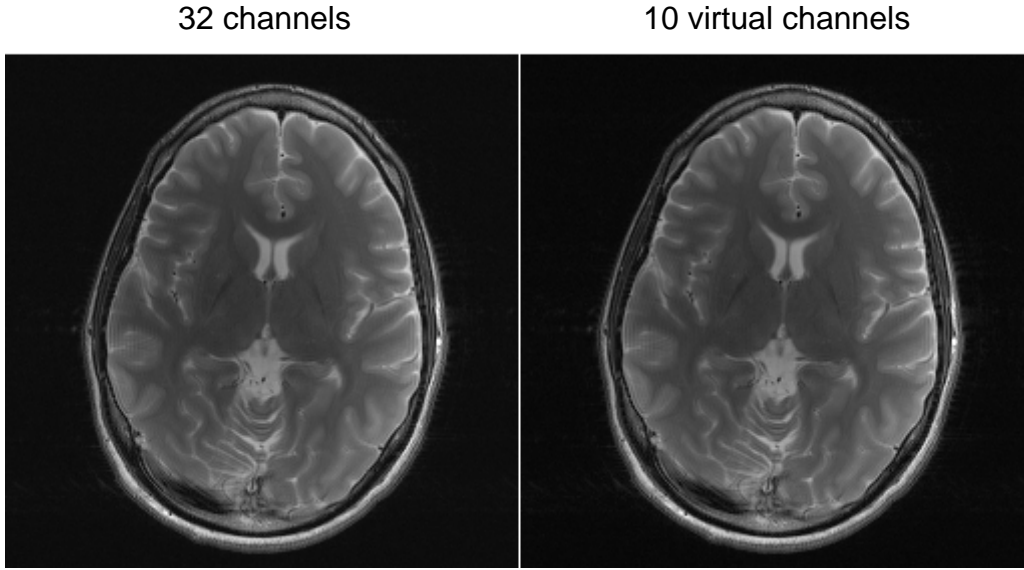


Figure 2.12: Comparison of a reconstructed image obtained with a 32 channel head coil (left), and a reconstruction from 10 virtual coil elements, generated by means of truncated SVD.

the largest singular values. Due to data redundancy, no visible difference between the two reconstructions can be observed.

2.7.4 SENSE Reconstruction

SENSE is an image space based parallel imaging method. This means that the elimination of the aliasing artifacts is performed in image space, after the application of an inverse Fourier transform. As demonstrated in section 2.5, a violation of the sampling theorem due to the reduced *FOV* leads to a superposition of periodic repetitions of the original full *FOV* image $\hat{\rho}$. This means that each pixel I^k in the accelerated image acquired with coil k consists of a superposition of R (the acceleration factor) pixels from $\hat{\rho}$, which are weighted according to the values of the coil sensitivities C^k at the corresponding pixel positions l .

$$I^k = \sum_{l=1}^R C_l^k \cdot \hat{\rho}_l \quad (2.27)$$

The index l counts from 1 to R (corresponding to the number of pixels that are superimposed), and k counts from 1 to the number of coils N_c . As shown in Figure 2.13 for $N_c = 4$ and $R = 2$, the pixels from all N_c coils can be stacked in a single complex signal vector \vec{I} with dimension $N_c \times 1$. The same can be done with all superimposed pixels from the full *FOV* image $\hat{\rho}$, which form an $R \times 1$ vector $\vec{\hat{\rho}}$. C can then be written as an $N_c \times R$ matrix consisting of the coil

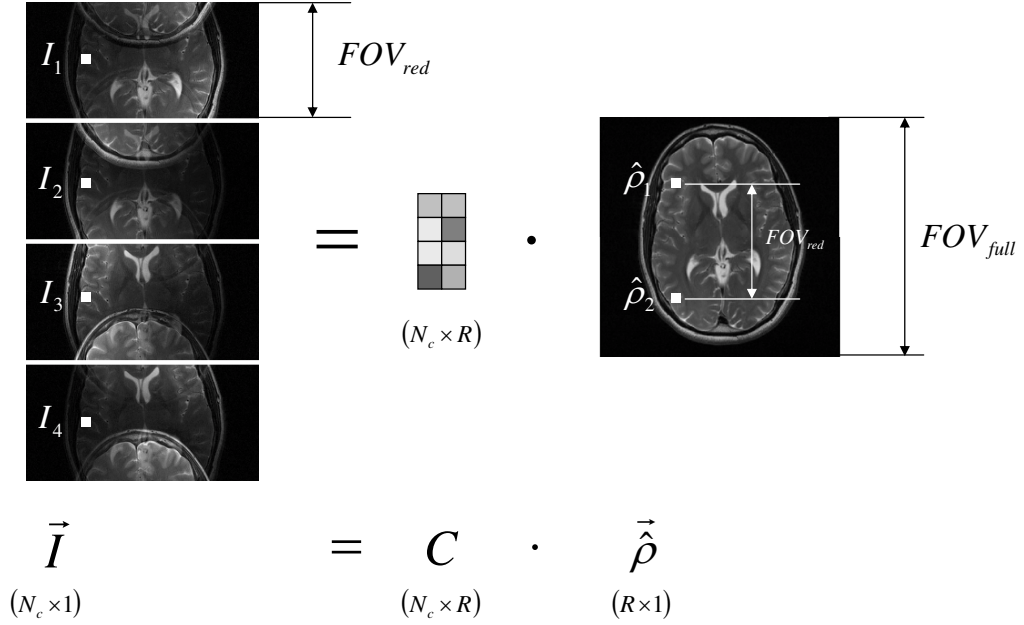


Figure 2.13: Illustration of SENSE reconstruction for acceleration factor $R = 2$ and $N_c = 4$. The pixels from all N_c coils can be stacked in a single complex signal vector \vec{I} with dimension $N_c \times 1$. The same can be done with all superimposed pixels from the full FOV image $\hat{\rho}$, which form an $R \times 1$ vector $\vec{\hat{\rho}}$. C can then be written as an $N_c \times R$ matrix consisting of the coil sensitivities of all N_c coils at the R superimposed positions, which leads to a system of linear equations that can be written in matrix form.

sensitivities of all N_c coils at the R superimposed positions, which leads to the following system of linear equations:

$$\begin{pmatrix} I_1 \\ I_2 \\ I_3 \\ I_4 \end{pmatrix} = \begin{pmatrix} C_{11} & S_{12} \\ C_{21} & S_{22} \\ C_{31} & S_{32} \\ C_{41} & S_{42} \end{pmatrix} \begin{pmatrix} \hat{\rho}_1 \\ \hat{\rho}_2 \end{pmatrix}. \quad (2.28)$$

This system of equations can be written in matrix form:

$$\vec{I} = \mathbf{C} \cdot \vec{\hat{\rho}}. \quad (2.29)$$

If the coil sensitivity matrix C is known, the values of the original full FOV $\vec{\hat{\rho}}$ can be recovered (unfolded) by means of a generalized inversion, e.g. the pseudoinverse $pinv(C) = (C^H C)^{-1} C^H$:

$$\vec{\hat{\rho}} = pinv(C) \cdot \vec{I}. \quad (2.30)$$

This reconstruction step is then repeated for all pixels in the image with reduced field of view. While only 1D subsampling is discussed here, it is also possible to use the SENSE method in the case of 2D undersampling when a second phase encoding direction is used in 3D imaging [50].

For SENSE based image reconstruction, the coil sensitivity matrix C has to be known. The most simple method to estimate this information, which was also suggested in the original SENSE paper [3], is to perform a reference scan prior to the accelerated measurement. This is a fully sampled 3D scan with low spatial resolution and a total scantime of approximately 15

seconds. As the coil sensitivities only consist of smooth signal changes, they can be captured with such a low resolution scan, which has the additional advantage of good SNR. It is obtained with both the body coil and the phased array coil. The images from each element of the array depict a modulation of the image $\hat{\rho}$ with the corresponding coil sensitivity C^k . The underlying image $\hat{\rho}$ is also obtained with the body coil, which means that estimates of the sensitivities C^k can be obtained by a normalization of the images from the coil array by the body coil image. If it is not practical to use a body coil image, the SOS combination of the individual channels (equation 2.23) can also be used instead. The main disadvantage of this approach is the fact that patient motion between the reference scan and the accelerated scan, or during the accelerated scan, leads to incorrections in the estimated coil sensitivities. This lead to the development of autocalibrated methods (see section 2.7.5). An additional discussion about strategies to estimate the coil sensitivities and the effects of miscalibration can be found in section 2.7.6.

Even if the sensitivity matrix is known perfectly, SENSE reconstruction can only be performed if the matrix inversion in equation 2.30 is possible. It is evident that the number of superimposed pixels (corresponding to the acceleration factor) must not exceed the number of receive coils, as this results in an underdetermined system of equations. While it is possible to use the SENSE method with arbitrary coil configurations, it is important that the used phased array coil delivers independent information in the dimension that is undersampled (the independence of information in different channels of a coil array is discussed in more detail in the context of coil compression in section 2.7.3). If the different coils have a significant overlap, the matrix inversion in equation 2.30 is challenging because the rows of the sensitivity matrix C become linearly dependent. This leads to noise amplification in the reconstructed image, and can be quantified by means of the so called geometry factor (g -factor) g_l [3]:

$$g_l = \sqrt{\text{diag}\{(C^H C)^{-1}\} \text{diag}\{(C^H C)\}} \geq 1. \quad (2.31)$$

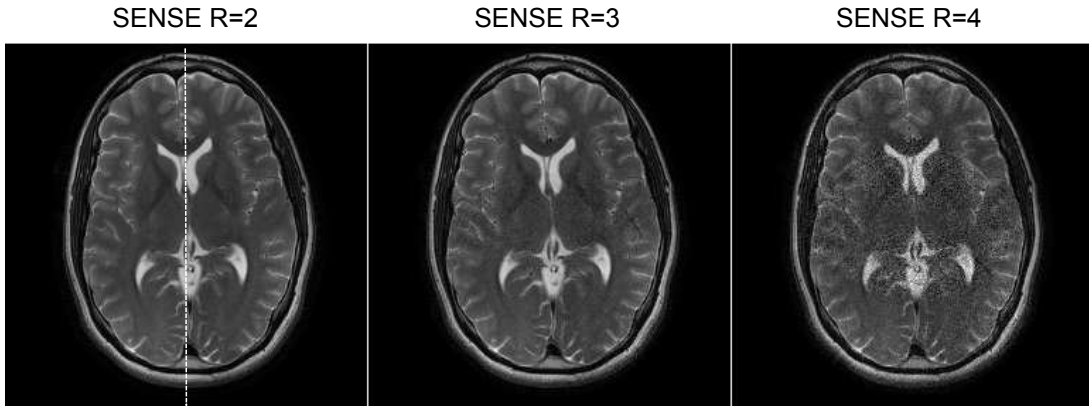
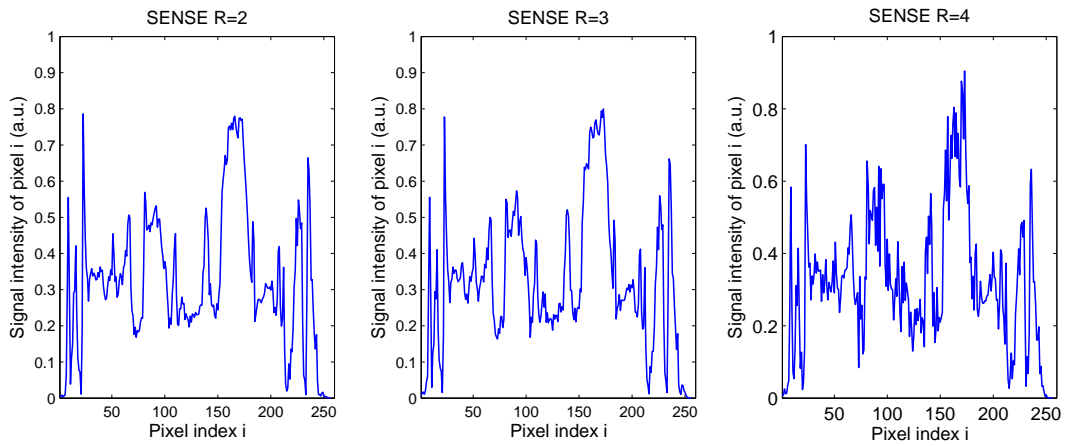
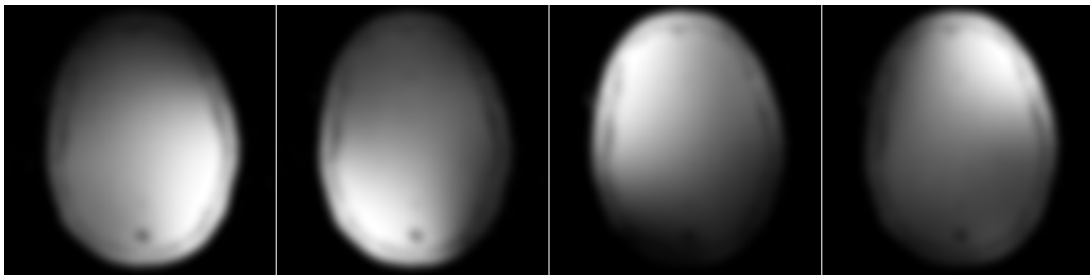
In equation 2.31 diag stands for the diagonal matrix elements. The SNR of a SENSE accelerated image (SNR^{acc}) is given by (see the original SENSE paper [3] for a derivation of these relations):

$$SNR_l^{acc} = \frac{SNR_l^{full}}{g_l \sqrt{R}}. \quad (2.32)$$

This is illustrated in Figure 2.14, which shows a SENSE reconstruction with acceleration factors $R = 2, 3, 4$ for a 4 channel data set. The coil sensitivities were estimated with a normalization of the individual coil images $\hat{\rho}_k$ by the corresponding SOS combination $\hat{\rho}_{SOS}$ (equation 2.23), followed by filtering with a 2D Gaussian low pass filter. While the reconstruction for $R = 2$ yields an almost perfect image, the result for $R = 3$ is already slightly corrupted by noise and residual aliasing artifacts. Pronounced non-uniform noise enhancement can be observed in the case of $R = 4$. Note that noise amplification is highest in the central parts of the image, due to the highest amount of overlap of the coil sensitivities in this region.

2.7.5 GRAPPA Reconstruction

In contrast to SENSE, GRAPPA [4] is a k -space based method. This means that rather than trying to unfold the aliased images, the goal is to recover the k -space coefficients that were

(a) SENSE Reconstructions for different acceleration factors R .(b) cross-section plots across a vertical line indicated in the reconstruction for $R = 2$ in (a).

(c) Sensitivities used for SENSE reconstructions in (a).

Figure 2.14: SENSE reconstruction with acceleration factors $R = 2, 3, 4$ for a 4 channel data set. While the reconstruction for $R = 2$ yields an almost perfect image, the result for $R = 3$ is already slightly corrupted by noise and residual aliasing artifacts. Pronounced non-uniform noise enhancement can be observed in the case of $R = 4$. Note that noise amplification is highest in the central parts of the image, due to the highest amount of overlap of the coil sensitivities in this region (a). This is also illustrated by cross-section plots across a vertical line (direction of acceleration) of the reconstructions (b). Coil sensitivities were estimated with a normalization of the individual coil $\hat{\rho}_k$ images by the corresponding SOS combination $\hat{\rho}_{SOS}$ (equation 2.23), followed by filtering with a 2D Gaussian low pass filter (c).

not sampled during data acquisition. The key idea of the GRAPPA method is that due to the use of phased array coils, individual coil images consist of a modulation of the underlying spin density $\hat{\rho}$ and the coil sensitivity C^k . This means that the acquired k -space data is a convolution of the Fourier transform of $\hat{\rho}$ with the Fourier transform of C^k . This operation distributes the information that is stored in a single k -space data point to its neighbors. Therefore, it is possible to recover missing points by a weighted linear combination of adjacent samples. The weights that are used during this interpolation procedure represent the influence of the coil sensitivities, and have to be estimated prior to the reconstruction. This is done with the additional acquisition of so called autocalibration-signal (ACS) lines at the center of k -space. In line with the previous section, only 1D subsampling in a single phase encoding direction (denoted as the y dimension for the remainder of the section) is considered to simplify the notation. Similar to the situation in SENSE, an extension to 2D subsampling of two phase encoding directions for 3D imaging is straightforward [51].

The signals from all coils at a certain k -space position k_y can be stacked in a single $1 \times N_c$ signal vector \vec{s} . This vector can then be fitted to an ACS sample point $\vec{s}_{acs}^{(m)}$ at the position $k_y + m \cdot \Delta k_y$, where m runs from 1 to $R - 1$:

$$\vec{s}_{acs}^{(m)} = w^{(m)} \cdot \vec{s}. \quad (2.33)$$

The matrix $w^{(m)}$ has the dimension $N_c \times N_c$ and shifts k -space data points by $m\Delta k_y$. A more general implementation fits multiple source points in the source vector \vec{s}^{src} simultaneously to multiple target points \vec{s}^{trg} . For this purpose, a GRAPPA reconstruction kernel is constructed, which consists of $N_x \times N_y$ source points that are fit to $R - 1$ target points for all coils simultaneously. This is illustrated in Figure 2.15 for $R = 4$ undersampling with 12 ACS lines and a 5×2 GRAPPA kernel. The number of source points in \vec{s}^{src} is $N_{src} = N_c \cdot N_x \cdot N_y$, and the number of target points in \vec{s}^{trg} is $N_{trg} = N_c \cdot (R - 1)$. It can be seen from Figure 2.15 that the GRAPPA kernel can be found multiple times within the ACS data block. By sliding the kernel through the ACS data, the fitting procedure becomes overdetermined, which improves the robustness of the estimated GRAPPA coefficients. If N_{rep} is the number of repetitions of the GRAPPA kernel in the ACS data block, all source data points can be assembled in a single matrix S^{src} of dimension $N_{src} \times N_{rep}$ and all target points in a matrix S^{trg} of dimension $N_{trg} \times N_{rep}$. A matrix W of GRAPPA coefficients with dimension $N_{trg} \times N_{src}$ can then be estimated by:

$$S^{trg} = W \cdot S^{src}. \quad (2.34)$$

$$W = S^{trg} \cdot pinv(S^{src}). \quad (2.35)$$

The GRAPPA coefficient matrix W can then be used to calculate missing data points from acquired samples S^{acq} :

$$S^{clc} = W \cdot S^{acq}. \quad (2.36)$$

S^{clc} is comprised of all $R - 1$ missing data points for all coils N_c . By sliding the GRAPPA kernel through all k -space positions k_x and k_y of the undersampled data set, all missing points at positions $(k_x, k_y + m\Delta k_y)$ are recovered. Therefore the result of the GRAPPA reconstruction is a complete set of k -space data for all coils. To reconstruct an image, individual coil images are

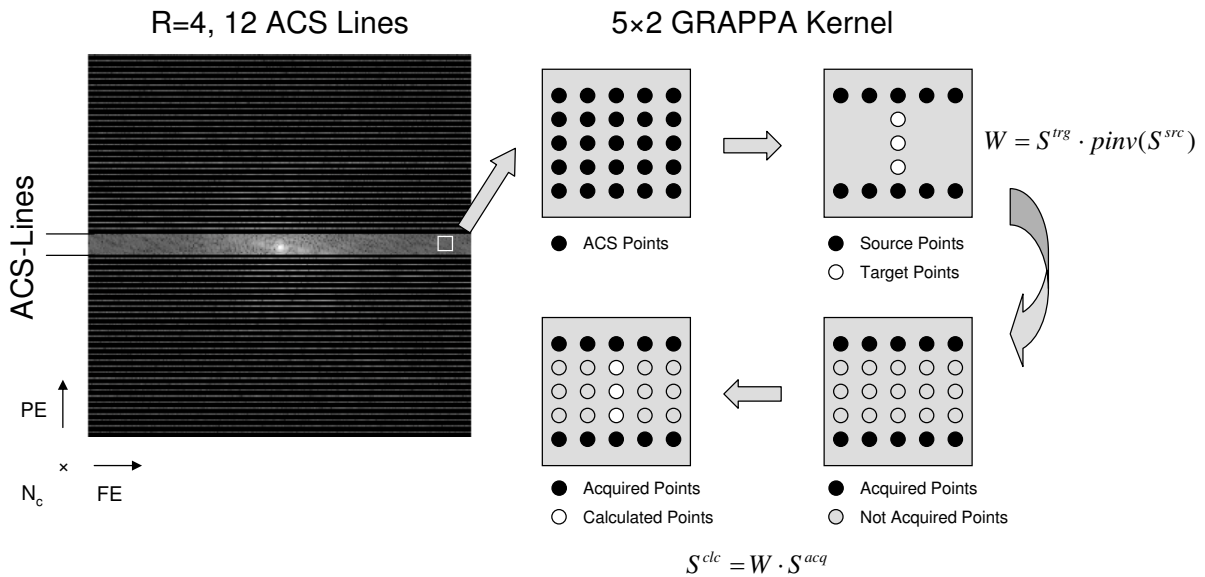


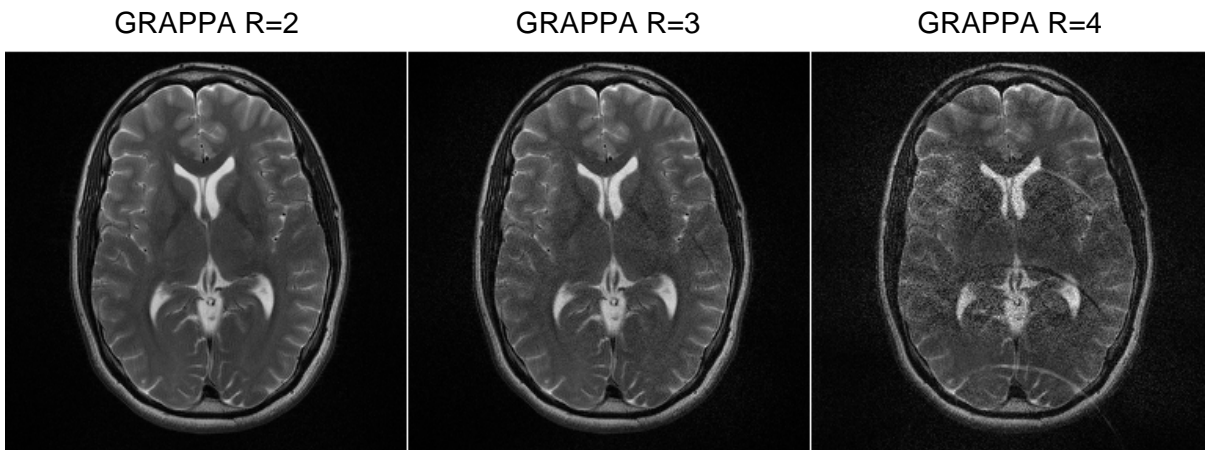
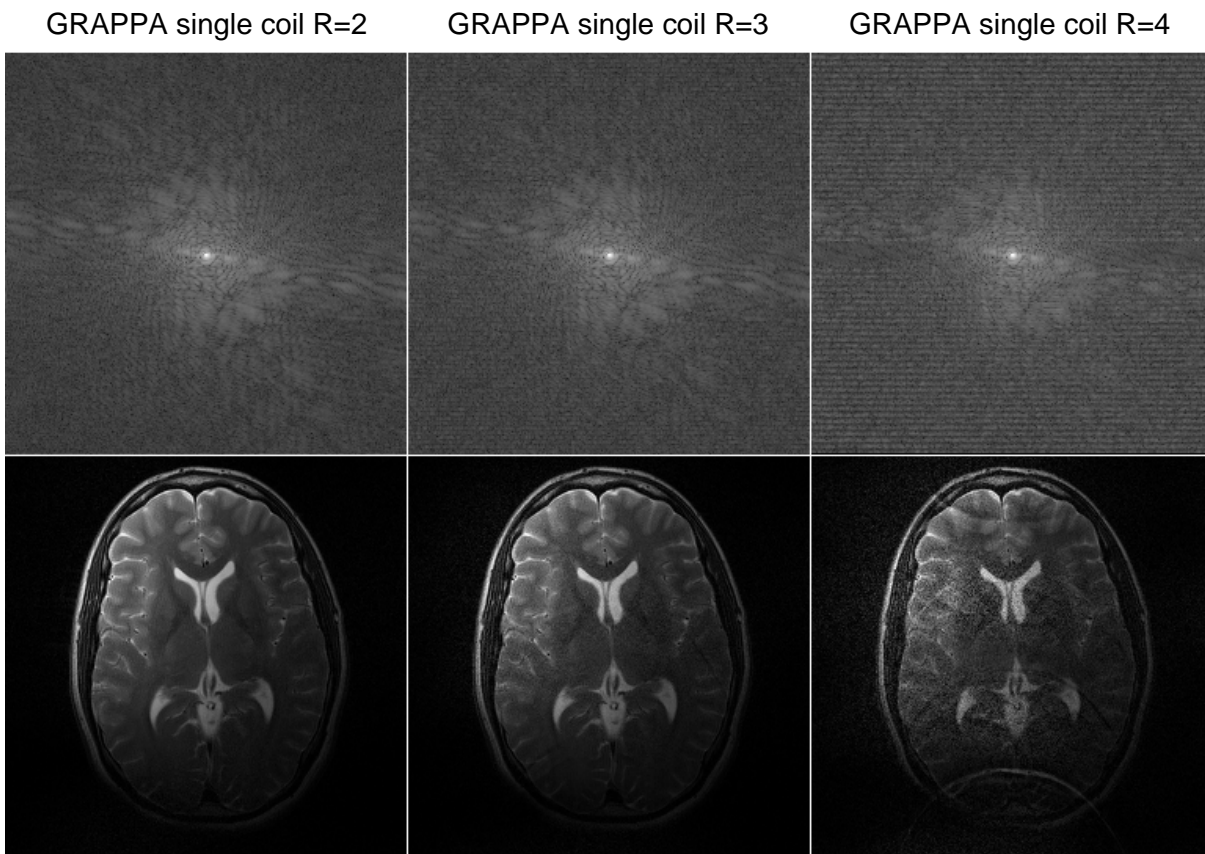
Figure 2.15: Illustration of GRAPPA reconstruction for acceleration factor $R = 4$, using 12 ACS lines and a 5×2 GRAPPA reconstruction kernel (see text for details).

generated with the use of an inverse Fourier transform, and the resulting images are combined to a single final image (e.g. by using the SOS combination of equation 2.23).

Figure 2.16 shows a GRAPPA reconstruction with acceleration factors $R \approx 2, 3, 4$ for the same 4 channel data set that was used in the SENSE section (2.7.4). 12 ACS lines at the center of k -space were used to estimate the GRAPPA coefficients, yielding slightly lower total acceleration factors than for the SENSE reconstructions of Figure 2.14. A 5×5 GRAPPA kernel was used. Similar to the SENSE case, the reconstruction for $R = 2$ yields an almost perfect image, the result for $R = 3$ is already slightly corrupted by noise and residual aliasing artifacts and pronounced non-uniform noise enhancement can be observed in the case of $R = 4$. The output of a single coil of the GRAPPA reconstruction, as well as the corresponding individual coil image, is also displayed in Figure 2.16. The striped patterns in k -space, resulting from inconsistencies between acquired data and data points that were reconstructed with GRAPPA can clearly be depicted in the cases of $R = 3$ and especially $R = 4$.

2.7.6 Estimation of coil sensitivities and extensions of SENSE and GRAPPA

One of the key steps in both SENSE and GRAPPA is an accurate estimation of the sensitivity profiles of the coil array that was used during data acquisition. One of the main differences between the two methods is that for SENSE, an explicit estimation of the sensitivities has to be performed, usually with the use of a pre-scan prior to the accelerated measurement. In contrast, no direct estimation of the the sensitivities is performed in GRAPPA, as this information is encoded in the reconstruction coefficients. As these coefficients are calculated directly from the undersampled data and individually for each reconstructed image, GRAPPA is called an auto-calibrated method. The assumption of this approach is that coil sensitivities vary only smoothly

(a) GRAPPA reconstructions for different acceleration factors R .

(b) Results of a single coil of the GRAPPA reconstruction.

Figure 2.16: GRAPPA reconstruction with acceleration factors $R = 2, 3, 4$ for a 4 channel data set. 12 ACS lines at the center of k -space were used to estimate the GRAPPA coefficients, yielding slightly lower total acceleration factors than the SENSE reconstructions of Figure 2.14 (a). Results of GRAPPA reconstructions of a single coil, as well as corresponding coil images after an inverse Fourier transform. The striped patterns in k -space, resulting from inconsistencies between acquired data and data points that were reconstructed with GRAPPA can clearly be depicted for $R = 3$ and especially $R = 4$ (b).

over the field of view and therefore can be estimated using only low frequency information located at the center of k -space. While GRAPPA is the most famous example of this approach, there are also formulations of autocalibrated SENSE, like mSENSE [52] (see [53] for a thorough review of autocalibration methods). The main advantage of this approach is that it is very robust with respect to patient motion, because all information that is needed to estimate the coil sensitivities is obtained directly from the undersampled data set. In the case of a reference-scan-based method, motion can lead to residual aliasing artifacts, as the sensitivity maps become incorrect if the patient position is not the same in the reference scan and the accelerated scans. This is illustrated in Figure 2.17 for two levels of rotational motion after the estimation of the coil sensitivities. It is notable that in the case of moderate motion (middle in Figure 2.17), the resulting aliasing artifacts do not severely deteriorate the reconstructed images. The reason is that the estimated coil sensitivities are smooth and still allow partial unfolding of the aliased pixels. Of course, if the range of motion increases, the reconstruction artifacts become more severe.

A disadvantage of autocalibration is that the actual acceleration factor that can be obtained in the accelerated scan is reduced due to the extra time needed for the encoding of the autocalibration lines. For example, the acceleration factor for a 256 matrix with $R = 4$ and a fully sampled k -space center of 12 reference lines drops from 4 to approximately 3.4. It is important to note that this is only true for Cartesian acquisitions. In radial sampling, the center of k -space is automatically oversampled, and no additional calibration lines have to be acquired. This means that radial trajectories are ideally suited for autocalibration methods. Another problem of autocalibrated methods arises if the measurement is limited in terms of SNR, e.g. for late echos in a multi-echo acquisition [54]. In these cases, as coil sensitivities are estimated directly from this data, they also exhibit low SNR and therefore limit the quality of the parallel imaging reconstruction. In contrast, even if the SNR of an individual accelerated scan is low, the coil sensitivity information is always obtained from a measurement with high SNR in the case of a reference scan based method.

A recent development was the introduction of modeling parallel imaging as a nonlinear inversion problem [6,7]. In this way, both the coil sensitivities and the image content are treated as unknowns and are jointly estimated during the iterations. The main advantage of this approach is that all available measurement data can be used in the coil estimation process, not only the dedicated autocalibration lines. This leads to an improved estimation of the sensitivities and is discussed in more detail in chapter 5.

Sections 2.7.4 and 2.7.5 only described Cartesian undersampling. In the case of SENSE, extensions to non-Cartesian sampling trajectories are possible. The first generalized approach that allowed to reconstruct data from arbitrary trajectories was called iterative- or CG-SENSE [55]. The situation is more complicated in the case of GRAPPA, as it has to be guaranteed that the undersampling pattern can be found in the ACS data block. This is a very active field of current research [56–59].

Acceleration is especially important in dynamic imaging when a high temporal resolution is required. This led to the development of specialized methods, which are tailored to dynamic applications [60–62].

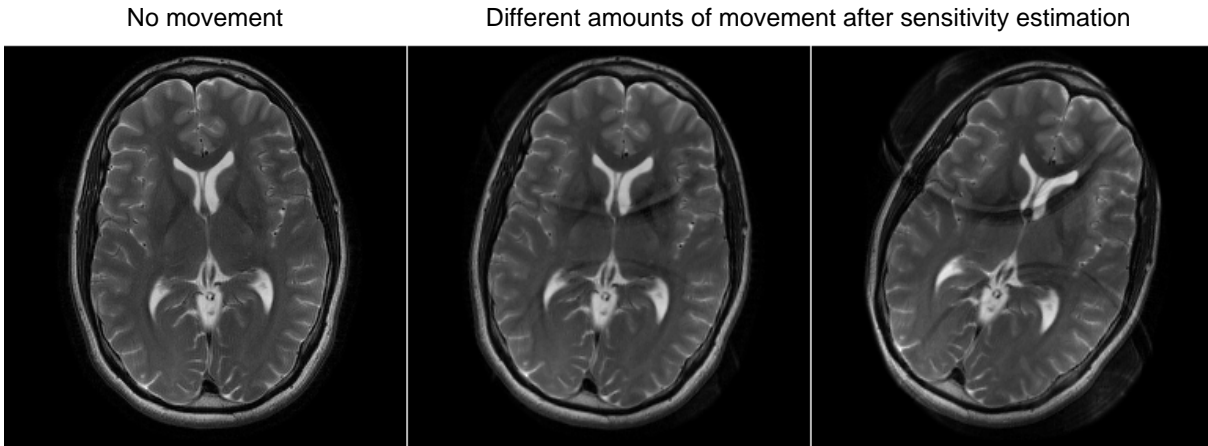


Figure 2.17: Illustration of the problem of errors in the coil sensitivity estimation due to object motion: SENSE reconstruction for undersampled data with acceleration factor $R = 2$, identical to Figure 2.14. No object movement occurred between coil sensitivity estimation and SENSE reconstruction, which yields a reasonable reconstruction (left). Using the same sensitivities after a slight rotation of the imaged object leads to residual aliasing artifacts in the reconstruction (middle). If the rotating motion is increased, aliasing artifacts become more severe (right).

2.8 Formulation of image reconstruction as an inverse problem

The last sections described the individual steps that are necessary during MR image reconstruction in detail. In this section, it is demonstrated that this process can also be formulated as an inverse problem. The advantage of this approach is that it provides a very general framework which allows to integrate non-Cartesian image reconstruction, undersampling and various parallel imaging methods. It is also possible make use of the large number of mathematical methods for regularization of inverse problems, which provide more advanced methods than the simple pseudo-inverse in equations 2.30 and 2.35. This leads to the concepts of regularized and constrained image reconstruction which are discussed in more detail in section 2.9 and chapters 4 and 5.

If all sampled discrete data points are stored in a single signal vector \vec{s} , the goal of image reconstruction is to estimate a single image vector \vec{u} consisting of N^2 pixel values in the case of an $N \times N$ image matrix. The so called forward problem describes the mapping of a reconstructed image \vec{u} to the measured k -space data \vec{s} :

$$K\vec{u} = \vec{s}. \quad (2.37)$$

As all operations that were used for parallel imaging and reconstruction from non-Cartesian data up to now are linear, they can be combined in a single matrix K , which is called is the forward operator, or system matrix. A schematic representation of the steps that are performed by K and it's adjoint matrix K^H is given in Figure 2.18. In both cases, estimations of the coil sensitivities need to be available and have to be determined in a previous step. A formulation where joint image reconstruction and estimation of the sensitivities is performed is described

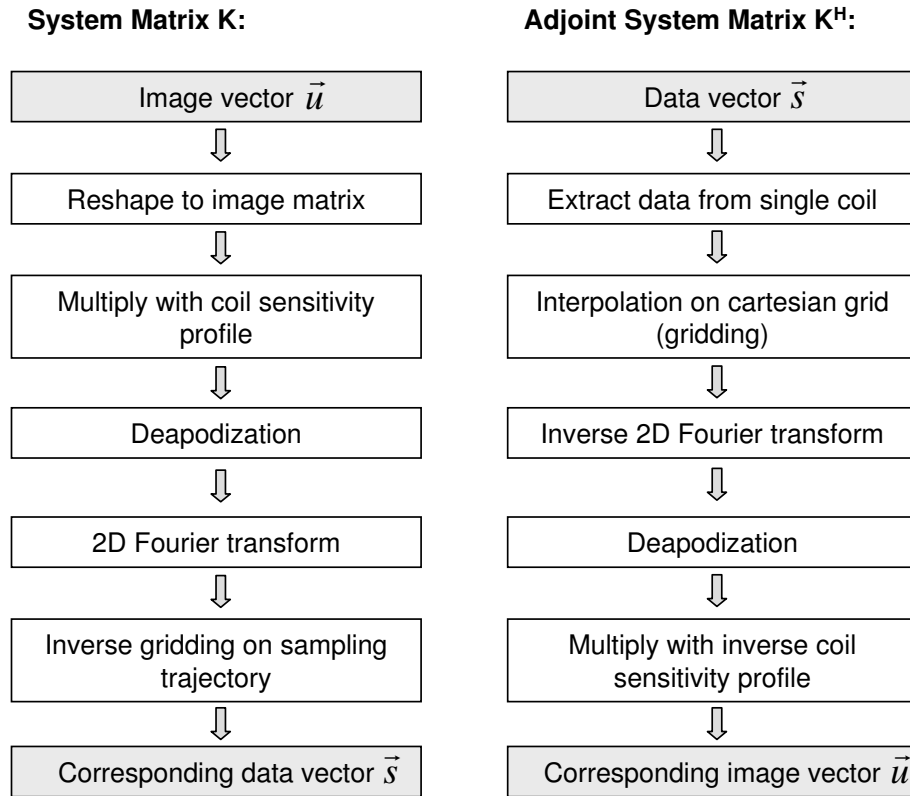


Figure 2.18: Schematic representation of the steps that are performed by the system matrix K and the adjoint matrix K^H , adapted from [1]. Input to K is an image vector \vec{u} of length $N^2 \times 1$ in the case of an $N \times N$ image matrix, and the output is a k -space data vector \vec{s} with sample points on an arbitrary trajectory from a single individual coil. The length of this vector depends on the specific sampling pattern and the amount of undersampling that was used during data acquisition. In the case of the adjoint matrix K^H , the input is a data vector \vec{s} from a single coil, and the output is an image vector \vec{u} corresponding to an $N \times N$ image matrix without modulation by the coil sensitivity. In both cases, estimations of the coil sensitivities need to be available and have to be determined in a previous step.

in chapter 5. Image reconstruction can then be seen as a solution of the corresponding inverse problem. In the case of undersampling (sections 2.5 and 2.7.1), the length of \vec{s} is smaller the length of \vec{u} , which leads to an underdetermined problem. Therefore, instead of a direct inversion of equation 2.37, it is advantageous to iteratively estimate an image vector \vec{u} that fits the data vector \vec{s} . The goal of iterative image reconstruction is to find an optimal $\hat{\vec{u}}$ that minimizes:

$$\hat{\vec{u}} = \min \frac{1}{2} \|K\vec{u} - \vec{s}\|_2^2. \quad (2.38)$$

2.9 Constrained Reconstruction

The key idea of constrained reconstruction methods is to incorporate additional a-priori knowledge about the structure of the solution of the image reconstruction problem, to compensate for the lack of sufficient measurement data. The potential danger of this approach lies in the fact that integration of the wrong a-priori information can introduce new artifacts (in the case of TV, introduction of staircasing artifacts is a typical example). Therefore, it is a very important task in constrained reconstruction to integrate the maximum amount of a-priori information that still delivers unbiased results.

The term constrained MR image reconstruction includes a wide range of strategies which date back already a considerable amount of time. Probably the simplest approach that falls into this category is half-Fourier imaging, which was already described 25 years ago [63], and exploits the fact that the frequency representation of a real valued function is redundant, and missing data can therefore be recovered based on Hermitian symmetry of acquired sample points. A comprehensive revision of early (before 1992) methods for constrained image reconstruction can be found in [64].

Keeping the notation of image reconstruction as an inverse problem, equation 2.38 can be generalized to incorporate a-priori information:

$$\hat{\vec{u}} = \min \frac{1}{2} \|K\vec{u} - \vec{s}\|_2^2 + \sum_i \lambda_i R_i(\vec{u}). \quad (2.39)$$

In equation 2.39 R_i are dedicated penalty terms, which are added to the cost function that has to be minimized, a process that is commonly known as regularization. Image reconstruction is then reformulated a constrained optimization problem. The penalty terms have to be designed such that the minimal value of the cost function that is minimized is achieved for certain solutions, which are most consistent with the a-priori information. The first term in equation 2.39 is the so called data fidelity term, which ensures that the solution of the optimization problem is still consistent with the acquired data (otherwise, the minimum of \vec{u} could be found by just setting the elements to $-\infty$). It should be noted that as real world measurement data is always corrupted by noise, it is not optimal to strictly enforce $\|K\vec{u} - \vec{s}\|_2^2$ to be exactly 0, but rather to keep it below some small scalar $\epsilon > 0$. Balancing of different penalty terms and the data consistency term is performed with the adjustment of the so called regularization parameters λ_i .

The choice of R_i is essential for the success of any approach for constrained image reconstruction from undersampled data. Chapter 4 aims to contribute to the task of developing dedicated

Table 2.1: Values of the TV penalty for the undersampled images from Figure 2.9.

Data set	TV-norm (a.u.)
Original fully sampled image	2801
Radial sampling, 256 projections	3255
Radial sampling, 128 projections	4493
Radial sampling, 64 projections	6274
Radial sampling, 32 projections	8281
Cartesian sampling, $R = 2$	3207
Cartesian sampling, $R = 4$	2993
Cartesian sampling, $R = 4$ (2D)	3973

penalty terms. A particular R_i must assign a high value to a solution that contains aliasing artifacts and, in the optimal case, the lowest value to the solution that allows clear depiction of the underlying structures without aliasing artifacts. Unfortunately, this can almost never be achieved for real world data. In contrast, it is often possible in the case of specific phantoms which are tailor-made for a specific penalty term, but such results should be interpreted with care. There are always trade-offs, most often involving a balance between preservation of fine image features, and the existence of residual aliasing artifacts in the solution.

The Total Variation (TV), which is already known in the field of image denoising for almost 20 years [18], was recently introduced as a penalty term for undersampled radial imaging [1, 19]. The TV norm is an L1 penalty of the gradient of the solution:

$$TV(u) = \int_{\Omega} |\nabla u| dx, \quad (2.40)$$

where Ω is the image domain. A more detailed discussion of TV is given in chapters 4 and 5, but basically, the assumption of TV is that an image consists of areas that are piecewise constant, and discontinuities or “jumps” of image contrast are penalized. Therefore it is ideally suited as a penalty term for undersampled radial imaging, because radial undersampling causes streaking artifacts, which are represented very well by TV. To illustrate this, the values of the TV-norm for the undersampling examples of Figure 2.9 are given in table 2.1. It can be observed that the increasing amount of streaking artifacts due to the reduction of radial projections is depicted very well with the TV-norm. On the other hand, this penalty is not particularly suited for regular Cartesian undersampling. It is especially noticeable that subsampling with $R = 4$ has a lower TV value than $R = 2$, and a lower value than radial sampling with 256 projections, where the streaking artifacts are almost unnoticeable to the eye. An essential element of TV is the use of the L1 norm in equation 2.40, which is responsible for the fact that TV preserves sharp edges in the reconstructions [18].

During the last years, the interest in constrained image reconstruction increased dramatically. This was triggered by the discovery of the theory of compressed sensing [14, 15]. MR image reconstruction of undersampled data was quickly identified to be an interesting application of

compressed sensing [16, 17]. Compressed sensing can be seen as a theoretical basis for L1-norm based image reconstruction, and it was shown that it can be applied successfully to various MRI applications [16, 17, 20, 65].

2.10 Evaluation of Image Quality and Validation of Image Reconstruction Algorithms

It was already mentioned that the introduction of a-priori knowledge can lead to new artifacts or biased results. Therefore, proper evaluation of image quality is a very important task. One of the key problems is the absence of a quantitative metric to classify the image quality of reconstructions from undersampled data, let alone the diagnostic value of the images. This is the subject of ongoing research, and first results were recently presented [66, 67]. The pixel by pixel root mean square (RMS) difference to a fully sampled gold standard image is used de-facto-standard as a measure of image quality in the literature. However, the main problem of this approach is that it cannot be used in real world applications, due to the lack of a fully sampled gold standard. Another problem is that quantitative metrics are usually integral measures. This means that they are very sensitive toward global changes of intensity values, but can be rather insensitive with respect to artifacts which only appear in a small, localized region. Unfortunately such artifacts can be misleading in terms of the diagnostic content of the image.

This means that clinical studies to investigate the potential of new image reconstruction strategies are essential, and basically the only possibility to assess the practical applicability of a specific method. For the rather young strategy of L1-constrained image reconstruction methods this is currently a very active field of research. Initial results of the first clinical study were recently reported for pediatric imaging [68].

Chapter 3

Adapted Random Sampling Patterns for Accelerated MRI¹

3.1 Introduction

Parallel Imaging (PI) is a well established strategy for scan time reduction in MRI, and methods like SENSE [3] and GRAPPA [4] are already routinely used in clinical exams. While conventional Cartesian subsampling is still the gold standard in most applications, alternative sampling patterns have been investigated for many years. Examples include non-Cartesian imaging strategies like radials [69] or spirals [70] and variable density sampling patterns [71–74]. The reason for the increasing interest in non-Cartesian trajectories are recent advances in MR-hardware, especially concerning the stability and linearity of the gradient system.

Within the framework of compressed sensing, Lustig et al. [16, 75] proposed the idea of randomized Cartesian subsampling. These randomized sampling patterns can be generated from Monte-Carlo simulations. With this approach, a probability density function (pdf) is constructed, and sampling pattern indices are drawn randomly according to that density. This leaves the problem of designing a pdf that will generate a suitable sampling pattern, and especially of determining the correct ratio of low to high frequency sample points. A common approach uses a density function which is proportional to a power of the distance from the origin in k -space. However, such strategies require optimization of one or even more design parameters which have a great influence on the reconstruction quality and depend on a suitably chosen mathematical model involving these parameters.

The goal of this work is to show that it is possible to construct an adapted random sampling pattern from a pdf that is generated by using measured k -space data as a reference, which automatically ensures an appropriate distribution of sample points. These sampling patterns are then used for conventional parallel imaging.

¹This chapter is based on the publication *Adapted Random Sampling Patterns for Highly Accelerated MRI, Magnetic Resonance Materials in Physics, Biology and Medicine (2011)* [21].

3.2 Theory

Random sampling patterns are one of the key ingredients in compressed sensing. They allow variable density sampling by distributing the sampling points according to a specified probability density function (pdf). Their main advantage is the fact that the resulting subsampling artifacts are incoherent.

In their work on compressed sensing, Lustig et al. [16] used a density function based on a polynomial function of the distance to the origin. Specifically, if k_y and k_z denote the k -space coefficients in the two phase encoding directions of a 3D data set, and N and M are the number of phase encoding steps in y and z direction, the pdf was given by $\left(1 - \frac{1}{\sqrt{2NM}} \sqrt{k_y^2 + k_z^2}\right)^p$ for a suitably chosen p . Since in general the magnitude of the Fourier coefficients of medical images does not obey a simple power law, this leaves open the question of choosing an appropriate exponent for the pdf which best approximates that distribution. Additionally, these sampling patterns usually contain an area with a user defined radius around the center of k -space where all sampling points are included. It was shown for compressed sensing that this improves the reconstruction quality, as the fully sampled low frequency k -space information can be used to estimate phase variations [16]. It is even more important for autocalibrated parallel imaging methods, because the sample points at the center of k -space are used to obtain the necessary information about the coil sensitivities. Suboptimal choice of these design parameters can lead to significantly lower image quality.

We therefore propose to generate a pdf which is directly based on the power spectrum of a template image. It is our observation that a template taken from any reasonably similar medical image data set will give good results: For the purpose of generating a suitable sampling pattern, only an estimation of the ratio of low to high frequency sample points has to be obtained. This merely depends on a similar distribution of the magnitude of k -space values, not similarity of magnitude and phase, which would require agreement in anatomical details. This also corresponds to the findings in [71] for the generalization potential of one dimensional variable density subsampling.

Specifically, the proposed method is as follows: Given a template image, we take the magnitude of its Fourier transform, scaled such that the integral is one. If multiple slices are acquired during this reference measurement, this step is repeated for all slices of the template data set and the results are averaged to increase robustness. Of course, if 3D sampling is performed for the reference measurement, an inverse Fourier transform has to be applied in the slice direction prior to the estimation of the pdf. However, as demonstrated by the results of this work, the method already has impressive generalization characteristics if only a single slice is used as a template. Using the template as a probability density function, we compute the corresponding cumulative probability density function (cdf). A random number uniformly distributed between 0 and 1 is then generated for each possible sampling point on a fixed uniform Cartesian grid defined by the desired image resolution. We accept a sampling point if the corresponding random number is less than the cdf for this coordinate. This is repeated until enough unique sampling points are generated such that the prescribed acceleration factor is reached. The whole procedure is repeated several times, and the sampling pattern with the least coherence is taken.

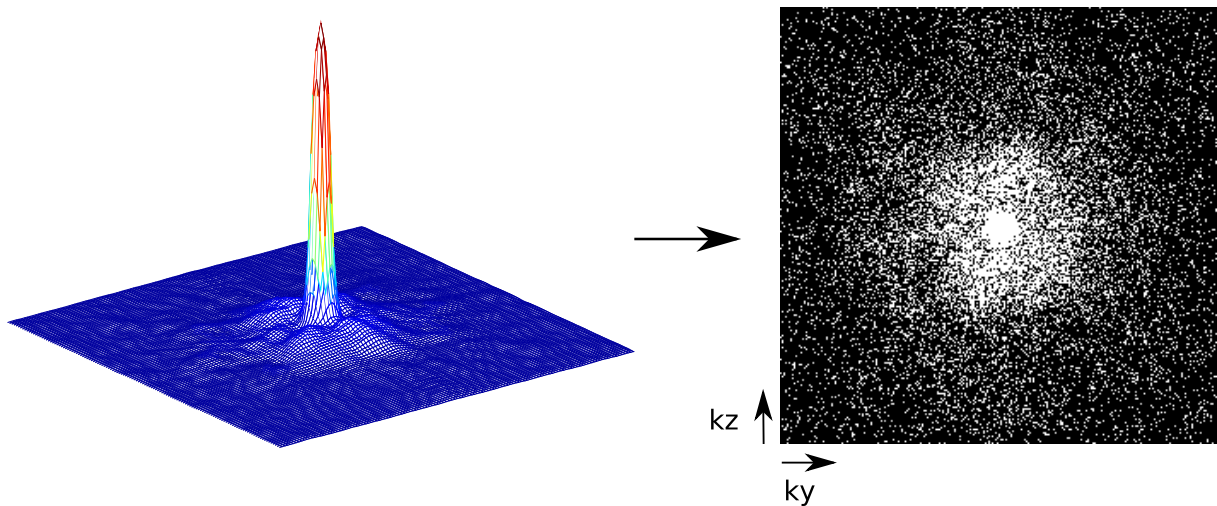


Figure 3.1: Example of a pdf (left) and a sampling pattern with subsampling factor $R = 4$ generated from it using a Monte Carlo method (right). k_y and k_z denote the two phase encoding directions; the frequency encoding direction is orthogonal to the image plane. The pdf was obtained from a reference scan and was used to generate the sampling patterns for the in vivo experiments (cf. Figure 3.5).

The relation between pdf and sampling pattern is illustrated in Figure 3.1. As described in Ref. [16], these randomized sampling trajectories can be easily implemented on MRI scanners by using 3D Cartesian encoding. The use of two phase encoding directions gives complete freedom to choose any sample point in the 2D phase encode plane (usually called the $k_y - k_z$ plane, with k_x being the direction of frequency encoding).

3.3 Materials and Methods

3.3.1 Downsampling experiments

The goal of the first experiment was to evaluate the proposed method against conventional, established sampling patterns. A fully sampled T_2 weighted 2D turbo spin echo scan of the brain of a healthy volunteer was acquired on a clinical 3T scanner (Siemens Magnetom TIM Trio, Erlangen, Germany) with a 32 channel head coil. Sequence parameters were repetition time $TR=5000\text{ms}$, echo time $TE=99\text{ms}$, turbo factor 10, matrix size $(x,y)=(256,256)$, 10 slices with a slice thickness of 4mm and an in-plane resolution of $0.86\text{mm} \times 0.86\text{mm}$. The raw data set was exported from the scanner and then subsampled, to simulate an accelerated acquisition. Downsampling was conducted with different sampling patterns, using reduction factors of $R=4$ and $R=9$. For the proposed method, the pdf was created using a data set from a scan of a different volunteer with the same sequence parameters, which was acquired several weeks earlier. The results were compared to reconstructions using established sampling patterns using the polynomial distribution [16] given above. Image reconstruction was performed using GRAPPA [4]. A $2\text{D } 5 \times 5$ GRAPPA kernel was used in all reconstructions, with Tikhonov regularization in the calibration step. To deal with random sampling patterns, the implementation described in

in [20] was used. All reconstructions were carried out slice by slice. Prior to image reconstruction, an SVD based coil compression scheme, as described in section 2.7.3, was used to reduce the computational load. 12 virtual channels were used in all experiments.

To test the generalization potential of the method, additional experiments were undertaken where different templates were used to generate the pdf. The same undersampled data set was used as in the comparison of different sampling patterns, and the following images were used as templates:

1. A single slice of the same data set, adjacent to the slice that was subsampled and reconstructed was used. Therefore, the anatomy is very similar to that in the undersampled image.
2. A 90 degree clockwise rotation of template 1.
3. A single slice from the same data set as template 1, measured at a more cranial position. This lead to slight changes in the imaged anatomy as the ventricles are no longer in the field of view, and slightly changes the size of the support of the image.
4. A single slice of a data set of a different volunteer, obtained with a different receive coil (12 channel head coil) with different image contrast. A gradient echo sequence was used with the following sequence parameters: repetition time $TR=68\text{ms}$, echo time $TE=5\text{ms}$, matrix size $(x,y)=(256,256)$, slice thickness of 5mm and an in-plane resolution of $0.89\text{mm} \times 0.89\text{mm}$.
5. A single slice of the sample data set from template 4, measured at a more caudal position. This lead to fundamental changes of the imaged anatomy and represents situations when unexpected anatomy is present in the undersampled image.

The goal of the next experiment was to test the applicability of the proposed method for a different anatomy. A fully sampled 2D spin echo scan of the knee of a healthy volunteer was acquired at 3T, using an 8 channel knee coil. Sequence parameters were repetition time $TR=1800\text{ms}$, echo time $TE=18\text{ms}$, matrix size $(x,y)=(192,192)$ covering a FOV of $150\text{mm} \times 150\text{mm}$, 10 slices with a slice thickness of 2mm. The raw data set was exported from the scanner and compressed to 4 virtual channels, again by means of an SVD based coil compression scheme after visual inspection of the singular values. A different slice from this data set was used as the template to generate the pdf. Downsampling was conducted with $R=2$ and $R=4$. This lower amount of acceleration in comparison to the previous experiments was used due to the lower number of receive channels of the knee coil.

3.3.2 Accelerated in vivo measurements

Accelerated measurements of the brain of a healthy volunteer were performed at 3T (Siemens Magnetom TIM Trio, Erlangen, Germany) with a 32 channel head coil. The 32 receive channels were again compressed to 12 virtual coils. A 3D gradient echo sequence was used which was modified by including a binary 2D mask that defined the randomized subsampled pattern. The

following sequence parameters were used: repetition time TR=30ms, echo time TE=6.4ms, flip angle FA=13°, matrix size (x,y,z)=(256,256,256), isotropic spatial resolution of 1mm. Subsampling with reduction factors R=4 and R=10 was performed. In all cases, pre-calculated sampling patterns for transversal scans of the brain were used, which were generated with the use of a pdf that was obtained from a single slice-reference scan of a different volunteer several weeks before the accelerated measurements. The reference measurement was performed with a 2D gradient echo sequence and with different sequence parameters (repetition time TR=20ms, echo time TE=3.5ms, flip angle FA=18°, matrix size (x,y)=(256,256), slice thickness 3mm) to test the robustness of the method. In addition, a 12 channel head coil was used instead of the 32 channel coil of the accelerated measurements. Raw data was exported from the scanner, a 1D Fourier transform was performed along the readout direction, and partitions orthogonal to this axis were reconstructed offline.

3.4 Results

Using the method presented in [16], random patterns with $(1 - r)^p$ polynomial distributions were generated for polynomial powers from 2 to 20 for acceleration factor R=4 and 4 to 20 for R=9, and the RMS difference of the corresponding GRAPPA reconstructions to the original unaccelerated image was calculated. All experiments were repeated three times, and the mean RMS values were calculated. The choice $p=8$ resulted in the lowest RMS error for R=4 while $p=5$ was the optimal choice for R=9.

Figure 3.2 displays undersampled k -spaces and GRAPPA reconstruction results for all tested sampling patterns and subsampling factors. To illustrate the importance of the optimization of the polynomial order p for the reconstruction quality, results are also shown for a conventional, non-optimized p . Reconstructions of optimized polynomial and template based patterns are almost free of artifacts for an acceleration factor of R=4, while the non-optimized version already shows some corruption due to incoherent aliasing. At reduction factors of R=9, all reconstructions show residual aliasing. However, optimized patterns and the proposed template based method are again comparable, while the amount of aliasing in the non-optimized case is significantly higher.

Figure 3.3 shows the comparison when different templates are used to generate the sampling pattern. The template of the first column is very close to the undersampled target image, which means that it is not surprising that the generated sampling pattern represents a proper distribution of the ratio of high to low k -space points. However, even with increasing deviation from the exact anatomy of the first template, the generated patterns still allow to reconstruct images with almost the same quality. This behavior is the same for moderate (R=4) and high acceleration (R=9), which demonstrates that exact anatomical details do not have to be known when generating sampling patterns with the proposed method.

RMS differences to an SOS image of the original fully sampled data set are given in Table 3.1. Experiments were each repeated 10 times for different sampling patterns generated from the same pdf, and mean values and standard deviations were calculated. While the results of

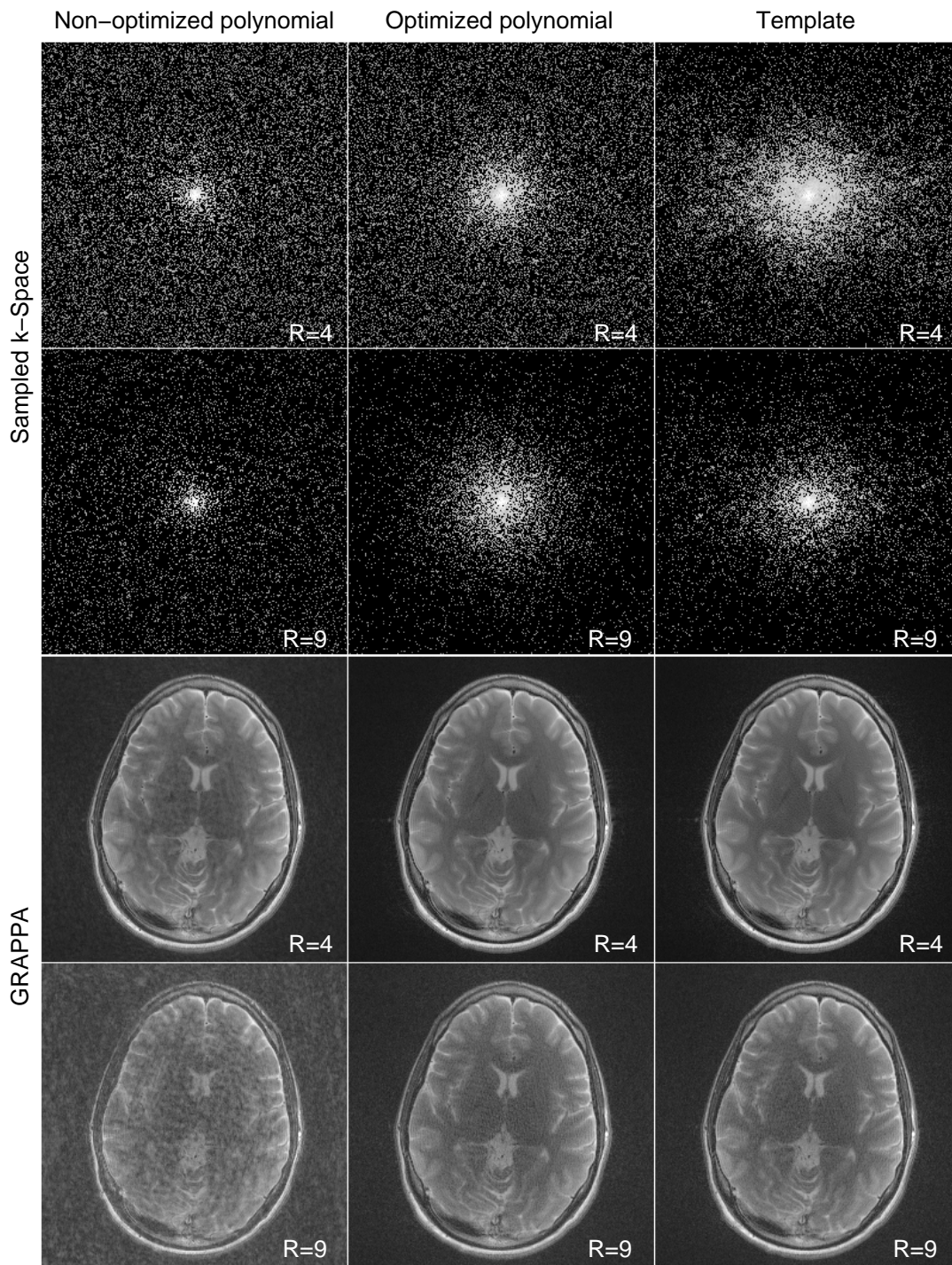


Figure 3.2: Comparison of reconstruction results for different sampling patterns: Random sampling with non-optimized (left) and optimized (middle) polynomial powers, and the proposed template based method (right) for acceleration factors of $R=4$ and $R=9$. The k -space data sets of the different sampling strategies (two top rows) and GRAPPA reconstructions (two bottom rows) are shown.

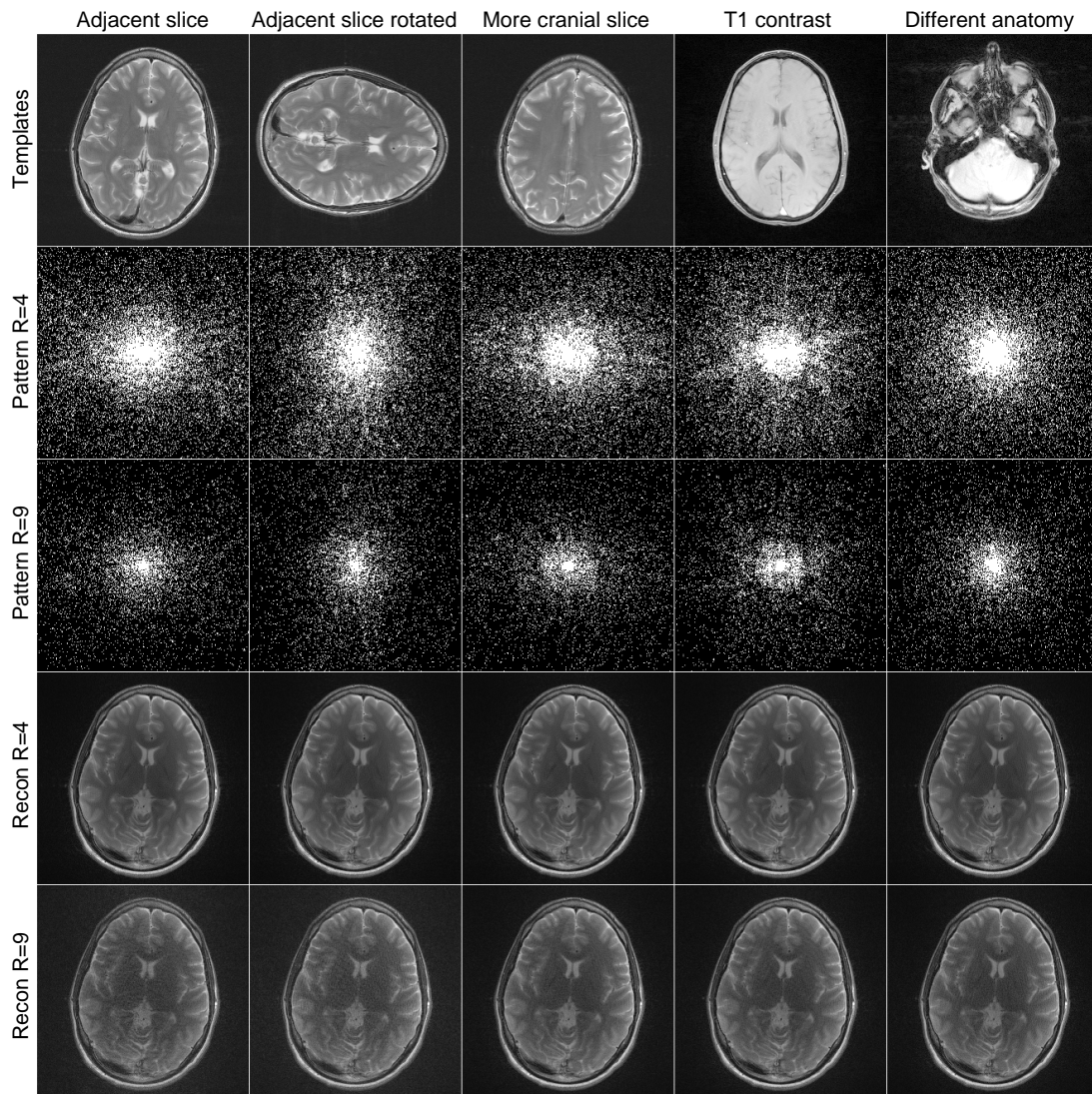


Figure 3.3: Comparison of reconstruction results when different templates are used to generate the sampling pattern. An adjacent slice of the same data set as the undersampled slice (first column), a rotation of this slice (second column), a more cranial slice with slightly different anatomy and size of the head (third column), a data set of a different volunteer with different contrast (fourth column) and completely different anatomy (fifth column) were used. The templates, corresponding sampling patterns and GRAPPA reconstructions are shown for $R=4$ and $R=9$.

optimized polynomials and the template based method are comparable, the errors of unoptimized polynomials are significantly higher.

Table 3.2 displays the results of RMS differences to the fully sampled reference data set when different templates were used. Like in the evaluation of Table 3.1, calculations were repeated 10 times for different sampling patterns generated from the same pdf. When compared with the results of Table 3.1, it can be seen that differences of the reconstruction error are far less pronounced for different templates than in the case of different sampling patterns. For both undersampling factors, the worst result was achieved in the case of the 90 degree rotation of the template. However, all errors are significantly lower than for the case of the non-optimized polynomial pattern in Table 3.1.

To illustrate the application of the proposed method in anatomic regions outside the brain, Figure 3.4 displays the template image, the fully sampled gold standard, sampling patterns, zero-filled SOS images, GRAPPA reconstructions and reconstructed k -spaces of the undersampled measurements of the knee for $R=2$ and $R=4$. RMS differences to the fully sampled gold standard are 0.049 ± 0.001 for $R=2$ and 0.077 ± 0.006 for $R=4$. Visual inspection of the results shows that reconstructions are artifact-free for $R=2$, while the results for $R=4$ already show some degradation due to reduced SNR. Due to the adapted design of the sampling pattern conventional SOS reconstructions already deliver results with surprisingly high image quality.

Figure 3.5 displays the template image, sampling patterns, zero-filled SOS images, GRAPPA reconstructions and reconstructed k -spaces of a single slice of the accelerated in-vivo experiments. The results show the same characteristics as the subsampling experiments. Reconstructions are free of artifacts for $R=4$, while results for $R=10$ already show some corruptions due to decrease of SNR and incoherent aliasing.

3.5 Discussion

The results from Figure 3.2 as well as the RMS errors (Table 3.1) demonstrate that the proposed method leads to reconstructions with an image quality that is almost identical to that of optimized polynomial patterns. It can also be seen that the quality of non-optimized polynomial distributions is clearly inferior, which illustrates the importance of the parameter optimization process for model-based strategies. However, finding an optimal parameter is a procedure with

Table 3.1: Quantitative evaluation of GRAPPA reconstruction errors of the downsampling experiments with different sampling patterns. RMS differences (a.u.) to an SOS image from the original fully sampled data set are shown. The values are means with standard deviations over 10 different patterns for the same pdf.

Pattern	R=4	R=9
Non-optimized Polynomial	0.104 ± 0.016	0.300 ± 0.071
Optimized Polynomial	0.042 ± 0.001	0.172 ± 0.037
Template	0.048 ± 0.004	0.165 ± 0.055

Table 3.2: Quantitative evaluation of the GRAPPA reconstruction errors of the experiments with different templates. RMS differences (a.u.) to an SOS image from the original fully sampled data set are shown. Means with standard deviations over 10 different patterns for the same pdf are shown.

Pattern	R=4	R=9
T2w	0.048 ± 0.004	0.147 ± 0.048
T2w rotated	0.057 ± 0.011	0.173 ± 0.082
T2w different slice	0.047 ± 0.001	0.148 ± 0.039
T1w	0.051 ± 0.001	0.111 ± 0.017
Different anatomy	0.047 ± 0.001	0.107 ± 0.027

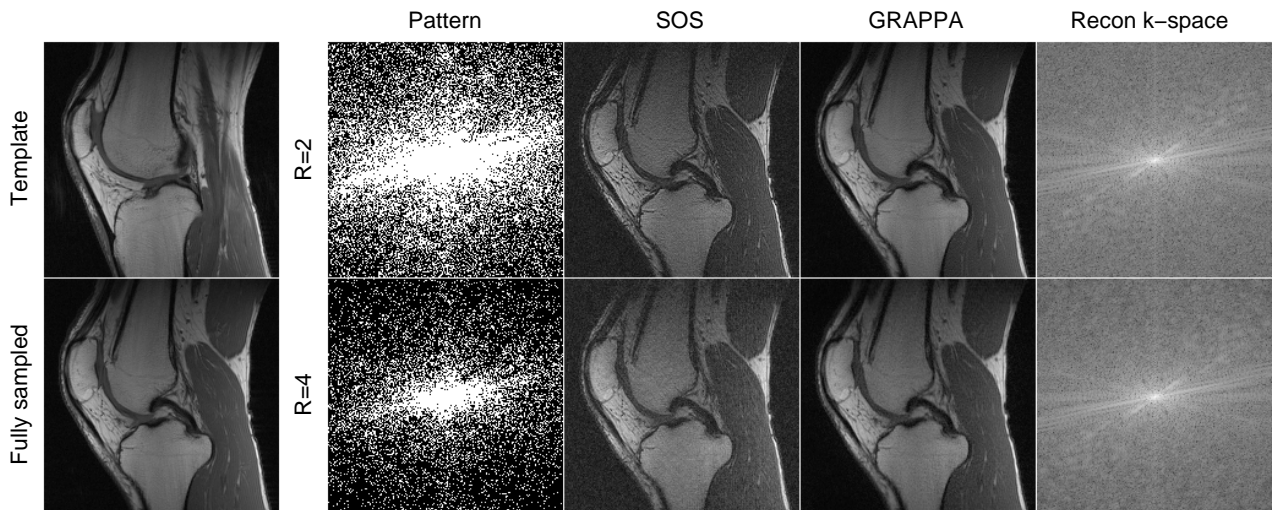


Figure 3.4: Template image used to generate the sampling pattern, fully sampled gold standard and reconstruction results of the experiments with the knee data set are shown. Left column: Used sampling pattern. Middle left column: undersampled and zero-filled (SOS) images. Middle right column: GRAPPA reconstruction. Right column: k -space of corresponding GRAPPA reconstruction. Top row: R=2. Bottom row: R=4.

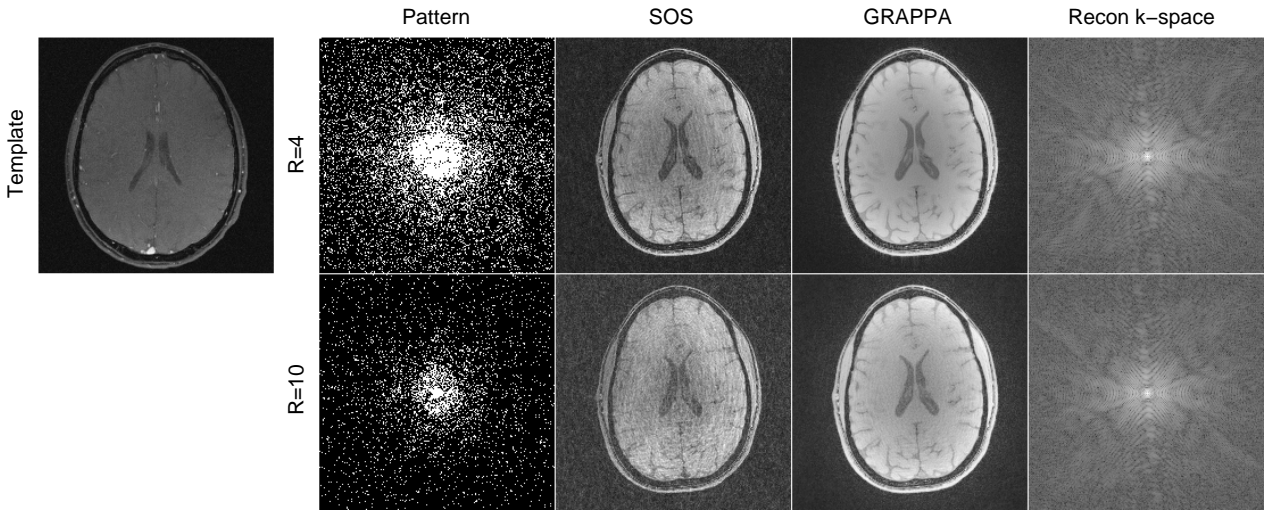


Figure 3.5: Template image used to generate the sampling pattern and reconstruction results of accelerated in-vivo measurements for different subsampling factors are shown. Left column: Used sampling pattern. Middle left column: undersampled and zero-filled (SOS) images. Middle right column: GRAPPA reconstruction. Right column: k -space of corresponding GRAPPA reconstruction. Top row: $R=4$. Bottom row: $R=10$.

a very high computational load, because image reconstruction has to be repeated multiple times for the same data set. Additionally, in contrast to the proposed method where the patterns were generated with reference data, optimization of the design parameters was performed based on the data set to be subsampled and reconstructed. This approach was chosen in order to provide optimal conditions for the reference method, but it is of course unrealistic for a truly accelerated measurement in practice.

Another difficulty in parameter tuning is the need of a quantitative metric for image quality evaluation, since optimization based on visual inspection of the images will always lead to subjective results. In this work, the RMS difference to a fully sampled reference image was used. As mentioned in section 2.10, this measure is widely used in MR image analysis but does not capture image quality or diagnostic relevance of the reconstructed images very well. It also requires a corresponding gold standard image usually not available in a clinical setting. Additionally, the success of finding suitable parameters depends on the correct choice of a mathematical model (such as $(1 - \sqrt{k_x^2 + k_y^2})^p$ as opposed to e.g. $(k_x^2 + k_y^2)^{-p}$, or even more complicated exponential models). In contrast, the proposed method does not require fixing a mathematical model a priori.

One reason for residual artifacts in the case of all random sampling patterns in this work is the fact that the distances between sample points in the outer regions of k -space increase and “holes” can appear in the sampling patterns, which are not completely covered by the extent of the GRAPPA reconstruction kernel. It is reasonable that image quality can be further increased by adding an additional constraint during the design of the sampling pattern, which ensures that a certain distance between adjacent sample points is not exceeded [20]. This will be the subject of further investigations.

As demonstrated in the results from Figure 3.3 and Table 3.2, the proposed method is very robust with respect to the choice of the reference data set, as only a similar distribution of the magnitude of k -space values is required, not similarity in image space. This distribution does not differ considerably for measurements of the same anatomical region, which is in agreement with the findings in [71]. Of course, the proposed method for generating sampling patterns is not limited to parallel imaging methods, it can also be used for compressed sensing.

3.6 Conclusion

It is demonstrated in this chapter that adapted variable density random sampling patterns can be generated with the use of template data sets. This approach yields results that are comparable to those of optimized model-based polynomial design strategies, and shows pronounced improvements in comparison to conventional, non-optimized polynomial distributions.

Chapter 4

Total Generalized Variation (TGV) for MRI¹

4.1 Introduction

Total Variation (TV) based strategies, which were originally designed for denoising of images [18] have recently gained wide interest for many MRI applications beyond denoising. Examples include regularization for parallel imaging [76, 77], the elimination of truncation artifacts [78], inpainting of sensitivity maps [79], their use as a regularization method for undersampled imaging techniques within the compressed sensing framework [16] as well as in iterative reconstruction of undersampled radial data sets [1, 19]. TV models have the main benefit that they are very well suited to remove random noise, incoherent noise-like artifacts from random subsampling and streaking artifacts from undersampled radial sampling, while preserving the edges in the image. However, the assumption of TV is that the images consist of regions, which are piecewise constant. Due to inhomogeneities of the exciting B_1 field of high field systems with 3T and above and of the receive coils, this assumption is often violated in practical MRI examinations. Additionally, even in situations when this is no severe problem, due to the assumption of piecewise constancy, the use of TV often leads to staircasing artifacts and results in patchy, cartoon-like images which appear unnatural.

This chapter introduces the new concept of Total Generalized Variation (TGV) as a penalty term for MRI problems. This mathematical theory has recently been developed [80], and while it is equivalent to TV in terms of edge preservation and noise removal, it can also be applied in imaging situations where the assumption that the image is piecewise constant is not valid. As a result, the application of TGV in MR imaging is far less restrictive. It is shown in this work that TGV can be applied for image denoising and during iterative image reconstruction of undersampled radial data sets from phased array coils, and yields results that are superior to conventional TV.

¹This chapter is based on the publication *Second Order Total Generalized Variation (TGV) for MRI, Magnetic Resonance in Medicine (2011)* [22].

4.2 Theory

4.2.1 The Concept of Total Generalized Variation

The Total Generalized Variation introduced in [80] is a functional which is capable to measure, in some sense, image characteristics up to a certain order of differentiation. In this section, we will restrict ourselves to give a short introduction which is not rigorous in the mathematical sense. The reader interested in the mathematical background may find more information in the Appendix.

First, recall the definition of the Total Variation, which is, for a given image u , usually expressed as

$$\text{TV}(u) = \int_{\Omega} |\nabla u| \, dx, \quad (4.1)$$

The Total Generalized Variation of second-order which we will use throughout this chapter bases on this definition but is generalized to represent a minimization problem itself:

$$\text{TGV}_{\alpha}^2(u) = \min_v \alpha_1 \int_{\Omega} |\nabla u - v| \, dx + \alpha_0 \int_{\Omega} |\mathcal{E}(v)| \, dx \quad (4.2)$$

Here, the minimum is taken over all complex vector fields v (e.g. including ∇u) on Ω and $\mathcal{E}(v) = \frac{1}{2}(\nabla v + \nabla v^T)$ denotes the symmetrized derivative. Such a definition provides a way of balancing between the first and second derivative of a function (which is controlled by the ratio of positive weights α_0 and α_1). In contrast to that, TV only takes the first derivative into account. For compatibility with the usual TV semi-norm we let, $\alpha_1 = 1$ throughout the chapter. Moreover, according to our experience, the default value $\alpha_0 = 2$ is suitable for most applications and does not need to be tuned, hence, one can say that no additional parameters are introduced with TGV.

Let us briefly mention some general properties of the functional. First, as TGV is the semi-norm of a Banach space, associated variational problems fit well into the well-developed mathematical theory of convex optimization problems, especially with respect to analysis and computational realization. Moreover, each function of bounded variation admits a finite TGV value, making the notion suitable for images. This means in particular that piecewise constant images can be captured with the TGV model which even extends the TV model. Finally, TGV is translation invariant as well as rotationally invariant, meaning that it is in conformance with the requirement that images are measured independent from the actual viewpoint.

It turns out that using TGV_{α}^2 as a regularizer leads to an absence of the staircasing effect which is often observed in Total Variation regularization. In the following, we like to give an intuitive explanation for this. In smooth regions of a given image u , the second derivative $\nabla^2 u$ is locally “small”. It is therefore beneficial for the minimization in problem in (4.2) to choose locally $v = \nabla u$ in these regions, resulting locally in the penalization of $\nabla^2 u$. On the other hand, in the neighborhood of edges, $\nabla^2 u$ will be considerably “larger” than ∇u , so it is beneficial for the minimization of (4.2) to choose locally $v = 0$ there. This locally results in TGV_{α}^2 measuring the first derivative which corresponds to the “jump”, i.e., the difference of the values of u on one side of an edge compared to the other. Of course, this argumentation is only intuitively valid, the values of actual minimizers v may be located anywhere “between” 0 and ∇u . This balancing

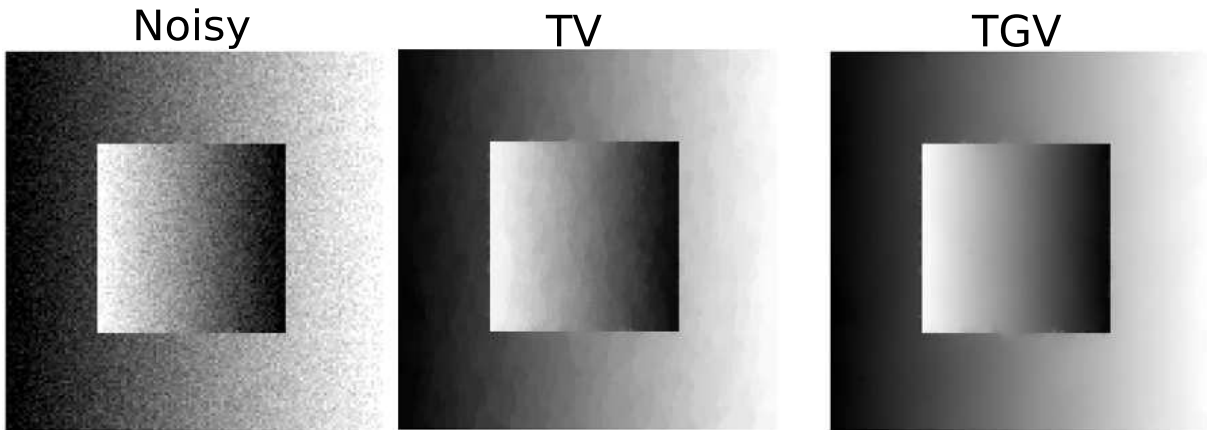


Figure 4.1: Denoising a ramp image with TV and TGV penalty. The noisy test image f (left), its Total-Variation regularization (middle) and its Total-Generalized-Variation regularization (4.3) (right). The absence of staircasing artifacts for TGV can nicely be observed here.

leads to edges measured in TGV_α^2 not being more “expensive” than a smooth function, which is similar to TV, but to smooth regions being “cheaper” than staircases in terms of TGV_α^2 , a feature which is absent in TV. Hence, Total Generalized Variation used as a penalty functional prefers images which appear more natural and, as we will see, leads to a more faithful reconstruction of MR images.

4.2.2 Application of TGV in MRI

The effects suggested in the previous subsection can in fact be observed when applied to MRI problems. One example is TGV_α^2 -based denoising which is briefly outlined in the following (for a detailed discussion of the noise suppression characteristics and a comparison with TV-based denoising, we refer to [80]). Given a noisy image $f \in L^2(\Omega)$, the denoised version u is computed as the solution of the following problem.

Method 1 (TGV image denoising)

$$\min_u \frac{1}{2} \int_{\Omega} (u - f)^2 dx + \text{TGV}_\alpha^2(u). \quad (4.3)$$

We propose (4.3) to remove noise from MR images which can include smooth signal modulations.

Testing this method with a piecewise affine artificial image (see Figure 4.1) clearly reveals its advantage over usual TV-based denoising. Here, the original image consists of regions with vanishing second derivative and since TGV_α^2 takes into account the second derivative as well as the edges, the method is able to reconstruct almost perfectly.

Besides image denoising, we propose to use TGV_α^2 for image reconstruction of undersampled data from multiple coils. It was demonstrated in [1] that iterative image reconstruction with a TV constraint efficiently eliminates streaking artifacts originating from radial subsampling:

$$\hat{u} = \min \frac{1}{2} \|Ku - s\|_2^2 + \lambda \text{TV}(u). \quad (4.4)$$

However, the tendency of TV to produce staircasing artifacts in piecewise smooth images is again present. We therefore modify the problem to incorporate TGV_α^2 .

$$\hat{u} = \min \frac{1}{2} \|Ku - s\|_2^2 + \lambda \text{TGV}_\alpha^2(u). \quad (4.5)$$

Note that estimates of the coil sensitivities are needed in both equation 4.4 and equation 4.5. A formulation where joint image reconstruction and estimation of the sensitivities is performed is described in chapter 5.

The proposed approach was tested with a noise-free numerical Shepp-Logan phantom that was modulated with a simulated coil sensitivity generated with the use of Biot Savart's law, to simulate the situation of undersampled radial multi channel acquisition. TGV yields again almost perfect reconstruction where conventional TV (4.4) suffers from staircasing artifacts (see Figure 4.2).

4.3 Materials and Methods

4.3.1 Application of TGV for denoising

Denoising was the first natural application for TGV. Two different data sets were acquired on a clinical 3T scanner (Siemens Magnetom TIM Trio, Erlangen, Germany). Written informed consent was obtained from all subjects prior to the examinations. The first measurement was a T_1 weighted 3D gradient echo scan of the prostate with injection of a contrast agent. Sequence parameters were $T_R = 3.3$ ms, $T_E = 1.1$ ms, flip angle $\alpha = 15^\circ$, matrix size $(x, y) = (256, 256)$, 20 slices, slice thickness 4 mm, in plane resolution $0.85 \text{ mm} \times 0.85 \text{ mm}$. The measurement showed severe signal inhomogeneities due to the exciting B_1 field and the surface coils used for reception [81]. Therefore, the assumption that the images consist of piecewise constant areas is violated.

The other test data set was a T_2 weighted turbo spin echo scan of the human brain, using a 32 channel receive coil. Sequence parameters were repetition time $T_R = 5000$ ms, echo time $T_E = 99$ ms, turbo factor 10, matrix size $(x, y) = (256, 256)$, 10 slices with a slice thickness of 4 mm and an in plane resolution of $0.86 \text{ mm} \times 0.86 \text{ mm}$. Complex Gaussian noise was then added to the original k -space data. The standard deviation of the added noise was chosen such that the ratio to the norm of the data was $1/15$. With this approach, a high SNR gold standard was available which allowed objective comparison of the TV and TGV results. This measurement did not show pronounced signal inhomogeneities, and the goal of the experiments with TGV was to show that even in these cases, TV introduces staircase artifacts which do not represent the underlying signal from the tissue.

Both data sets were exported, and offline denoising was performed with conventional TV, as well as with a Matlab (R2009a, The MathWorks, Natick, MA, USA) implementation of TGV (4.3).

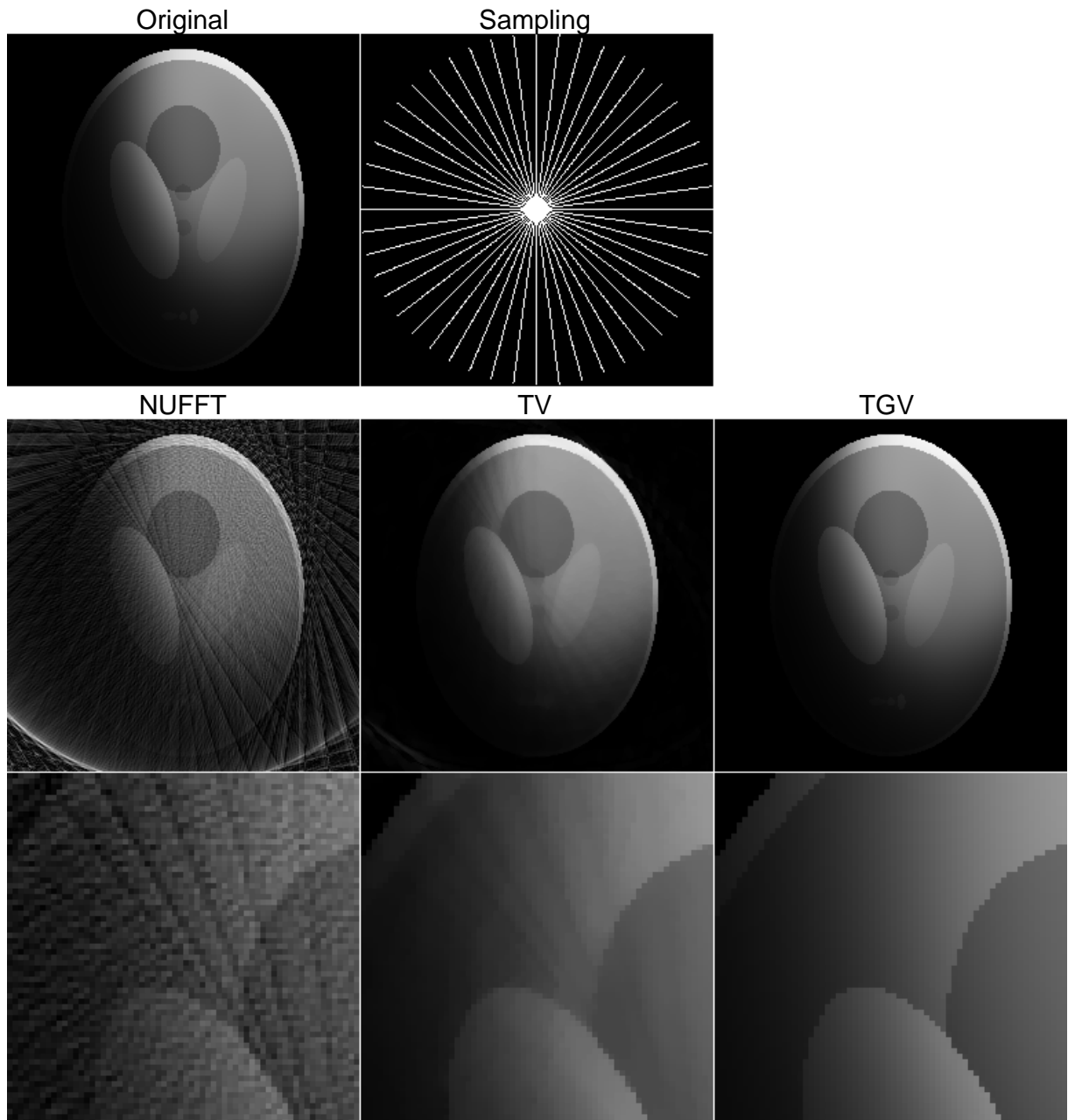


Figure 4.2: Reconstructions of a Shepp-Logan phantom from undersampled radial k -space data, modulated with a simulated coil sensitivity generated with the use of Biot-Savart's law. Top row: Original test image of size 256×256 (left) and the corresponding radial sampling pattern with 24 radial spokes (right). Middle row: Conventional NUFFT Reconstruction (left), Minimum-TV-Solution (4.4) (middle) and Minimum-TGV $_{\alpha}^2$ -Solution (4.5) (right). Bottom row: Magnified views from the middle row.

4.3.2 Image reconstruction of Subsampled Multicoil Radial Data with a TGV Constraint

Image reconstruction with TV regularization for subsampled radial data sets with removal of the intensity profiles and the phase of the individual coil elements prior to application of TV was first introduced by Block et al. [1]. Our TV reference implementation roughly follows this approach. Analogously to [1], it employs, prior to application of TV, for each coil, a reconstruction with a quadratic regularization on the derivative (H^1 -regularization) followed by the convolution with a smoothing kernel. The sensitivities are then obtained by dividing by the sum of squares image for each coil element. All results were also compared to an iterative parallel imaging method of CG-SENSE type [55], using the same coil sensitivities as in the TV experiments.

The fully sampled 32 channel TSE brain data set from the denoising experiments was subsampled retrospectively, to simulate an accelerated acquisition. Data from 32, 24, 16 and 12 radial projections was obtained. As $\frac{\pi}{2}n$, projections (402 for $n = 256$ in our case) have to be acquired to obtain a fully sampled data set in line with the Nyquist criterion according to the literature [26], this corresponds to undersampling factors of approximately 12, 16, 25 and 33.

Finally, undersampled 2D radial spin echo measurements of the human brain were performed with a clinical 3T scanner (Siemens Magnetom TIM Trio, Erlangen, Germany) using a receive only 12 channel head coil. Sequence parameters were: $T_R = 2500$ ms, $T_E = 50$ ms, matrix size $(x, y) = (256, 256)$, slice thickness 2 mm, in plane resolution 0.78 mm \times 0.78 mm. 96, 48, 32 and 24 projections were acquired, and the sampling direction of every second spoke was reversed to reduce artifacts from off-resonances [19]. Raw data was exported from the scanner, and image reconstruction was performed offline using a Matlab proof-of-principle implementation of the non-uniform fast Fourier transform (NUFFT) [33] and of the proposed TGV method (4.5).

Additionally, reconstruction was performed using an implementation which exploits the high parallelization potential of current graphic processing units (GPUs). It uses NVIDIA's compute unified device architecture (CUDA) framework [82] and leads to a significant acceleration in comparison to the Matlab implementation, which is discussed in the section "Computational requirements".

4.3.3 MR Image Reconstruction of Subsampled Spiral Data from Multiple Coils

Subsampled spiral rawdata was constructed from a different slice of the same data set that was used for radial subsampling. A variable density spiral trajectory [70] with 48 interleaves was designed such that it resulted in full sampling of k -space according to the sampling theorem. Synthetic spiral data was then obtained by inverse gridding of the measured k -space rawdata on these spiral arms. The NUFFT [33] was used for gridding and inverse gridding procedures. The data set was then subsampled by extracting subsets of 24, 16, and 12 spiral interleaves. This corresponds to undersampling of approximately 2.2, 3.3 and 4.3 in comparison to a fully sampled Cartesian scan.

The second spiral data set that was investigated in this work was provided by the International Society of Magnetic Resonance in Medicine (ISMRM) for their 2010 reconstruction

challenge (challenge: “Need for speed”, data set: “NFS_NZWA_09AUG06”). This data set was simulated from projection X-ray of an arterial bolus injection in a patient, with 512×512 resolution. B1 maps from an 8-channel head coil were derived from measurements of a water phantom and superimposed on the X-Ray data to create 8 “coil” images. Synthetic data was then generated using a variable density spiral trajectory. This approach was chosen over conventional MR-angiography or 4D CT measurements for the competition because it allowed to provide data with high SNR and very high spatiotemporal resolution while retaining some semblance of in-vivo flow dynamics. A detailed explanation of the data set is given on the ISMRM website². 37 timeframes had to be reconstructed and a single frame was reconstructed from 5 spiral interleaves, each with 2000 sample points. This corresponds to subsampling of approximately 26 in comparison to a fully sampled Cartesian scan. In this experiment, the images of all timeframes were considered to be one single 3D volume stack for the purpose of image reconstruction. Therefore the dimension of the data was $200 \times 2000 \times 8$ (number of spiral interleaves \times number of samples on a spiral trajectory \times number of coils), which was used to reconstruct a single volume of dimension $512 \times 512 \times 37$. 3D TGV was used as a penalty during image reconstruction.

4.4 Results

4.4.1 Application of TGV for Denoising

Figure 4.3 shows the results from TV and TGV for the T_1 weighted scan of the human prostate. Both methods remove noise while maintaining sharp edges efficiently. However, in regions where the assumption that the image consists of areas that are piecewise constant is violated, it is not surprising that TV results are significantly corrupted by staircasing artifacts. TGV on the other hand works equally well in these regions, as already pointed out in Figure 4.1.

The original image with high SNR, the noisy image and results with TV and TGV for the T_2 weighted brain scan are displayed in Figure 4.4. Even in this data set, where the assumption that the image consists of areas that are piecewise constant is valid because there are neither severe B_1 signal inhomogeneities nor modulations from the receive coil, TV introduces additional staircases which cannot be found in the original image. This effect is almost eliminated with TGV.

4.4.2 Image Reconstruction of Subsampled Multicoil Radial Data with a TGV Constraint

Figure 4.5 and Figure 4.7 compare the reconstructions of the undersampled radial imaging experiments from retrospective subsampling and truly accelerated imaging. For comparison, the fully sampled image corresponding to the results of Figure 4.5 can be found in Figure 4.4.

It is not surprising that conventional NUFFT reconstructions show streaking artifacts which get worse as the number of projections is reduced. Both TV and TGV reconstructions eliminate streaking artifacts efficiently. For moderate subsampling, results with CG-SENSE are of compa-

²<http://www.ismrm.org/10/recon/index.htm>

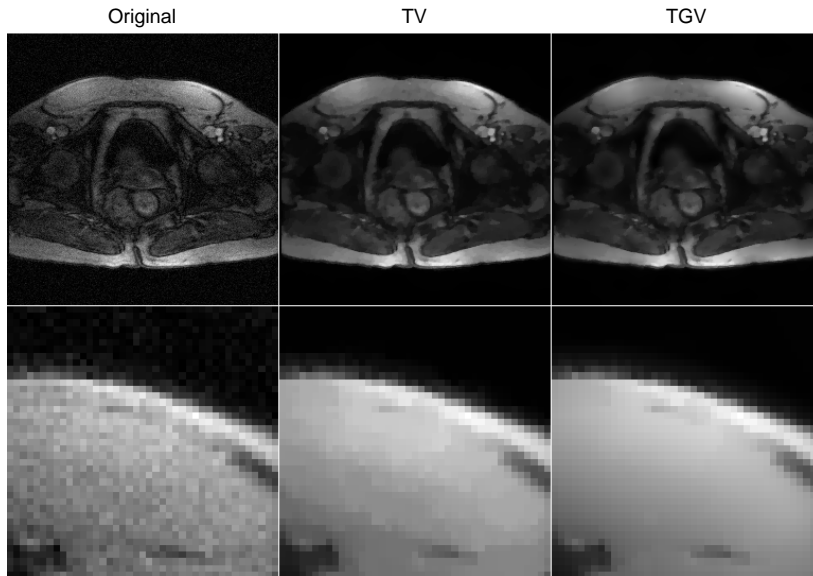


Figure 4.3: TV (middle) and TGV (right) denoising results from the contrast enhanced T_1 weighted prostate scan. The images show smooth modulations due to inhomogeneities of the exciting B_1 field and the surface coils used for signal reception which lead to significant artifacts when conventional TV is applied.

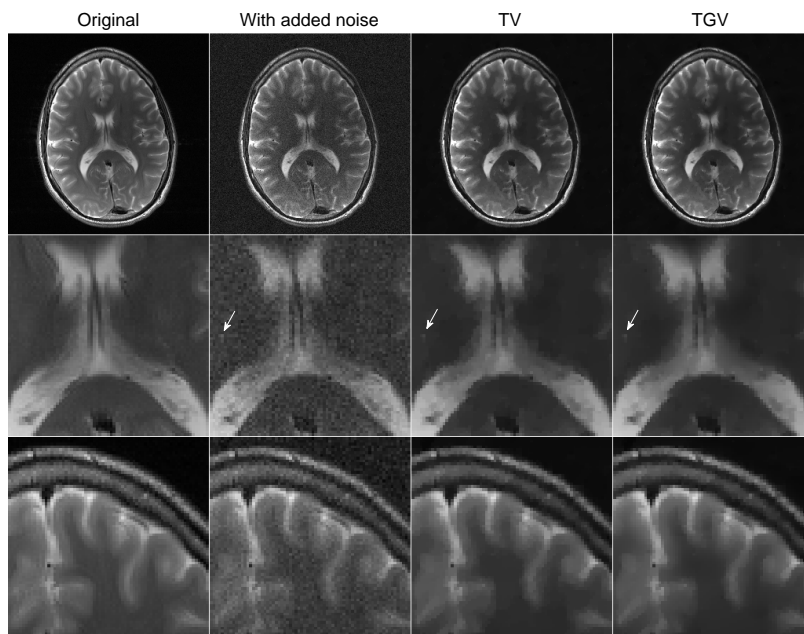


Figure 4.4: Denoising experiments for the T_2 weighted brain scan. In the top row, the original image with high SNR (left) which has been contaminated with additive Gaussian noise (middle left) is shown. TV (middle right) and TGV (right) denoising results are displayed as well as magnified views of the respective images (middle and bottom rows). An example of an unwanted image feature that is introduced during denoising is highlighted by arrows.

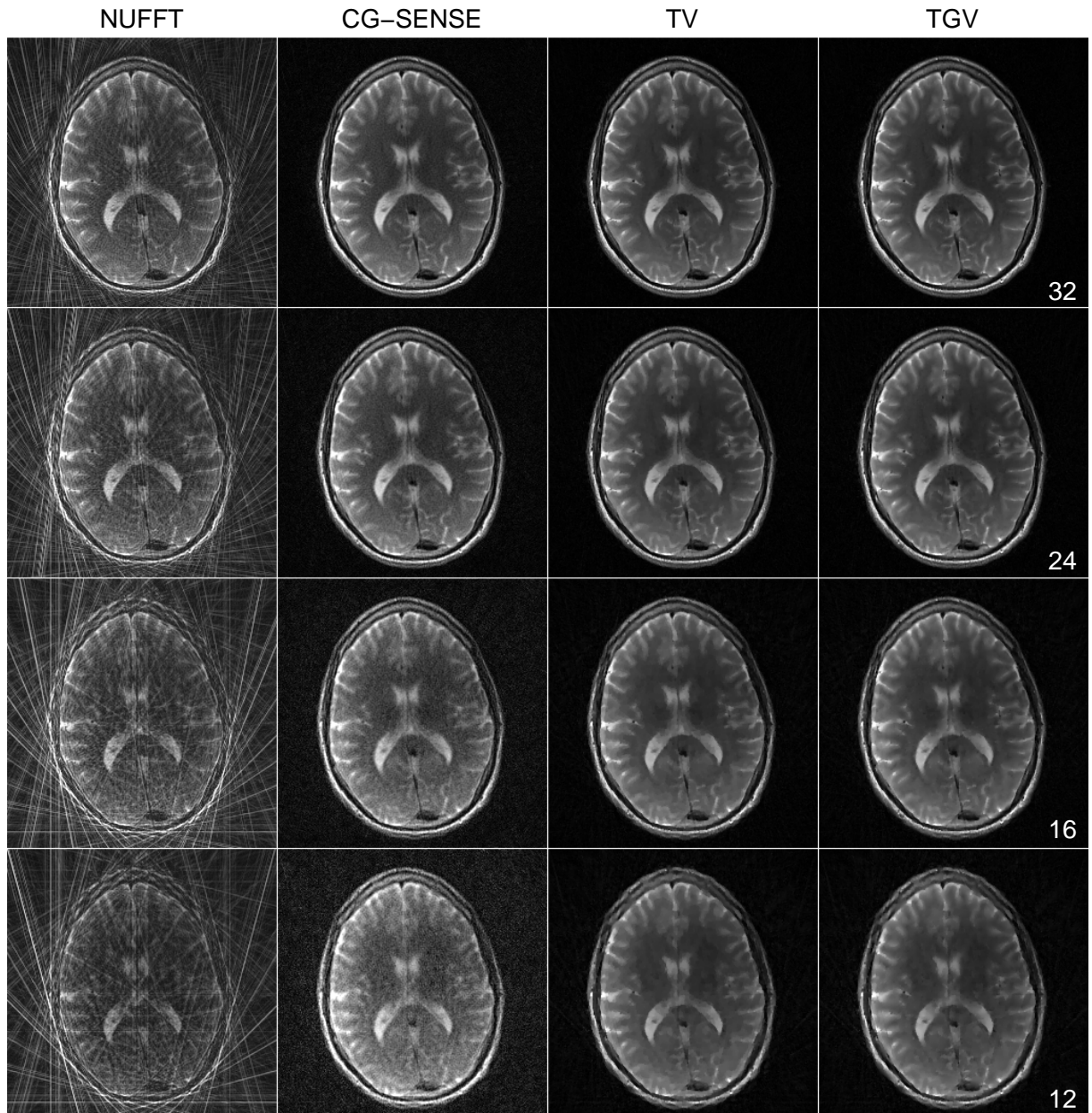


Figure 4.5: Results from experiments with the T_2 weighted brain scan (256×256 matrix) using 32, 24, 16 and 12 radial projections. The columns depict conventional NUFFT reconstructions (left), reconstructions with CG-SENSE (middle left), with a TV constraint (middle right) and with a TGV constraint (right), respectively. The original, fully sampled image is displayed in Figure 4.4.

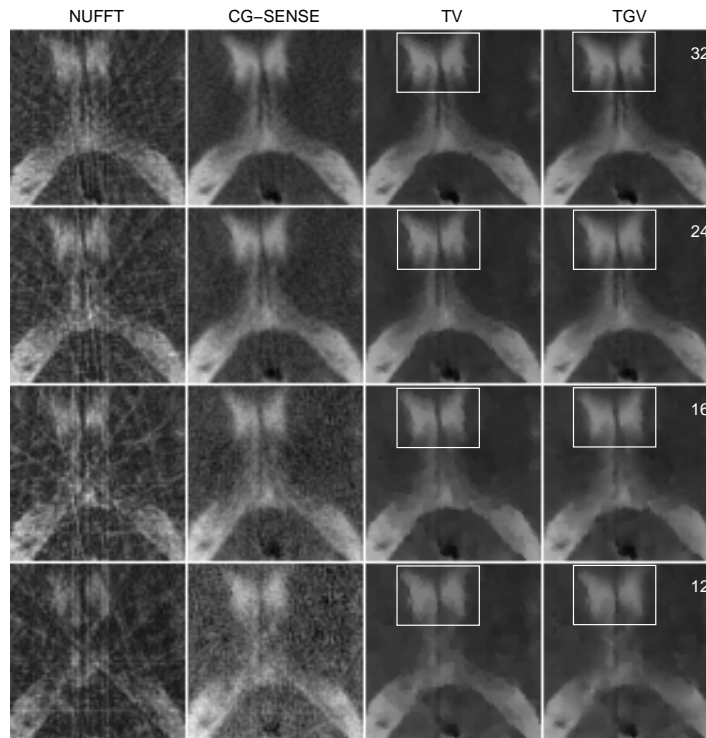


Figure 4.6: Magnified views of the same data as shown in Figure 4.5. The tendency of TV to introduce additional staircases is visible at the frontal interface of the ventricle (highlighted).

rable quality. While the results of TV and TGV are of roughly the same quality for all amounts of subsampling in all experiments, magnified views (Figure 4.6) again display staircasing artifacts in the TV results. While this is still a level of subsampling where CG-SENSE achieves acceptable results, effects of noise amplification are already visible. The difference between TV and TGV is subtle, but the tendency of TV to introduce staircases which are not present in the fully sampled image is clearly visible, e.g. at the frontal interface of the ventricle (highlighted region in Figure 4.6).

4.4.3 MR Image Reconstruction of Subsampled Spiral Data from Multiple Coils

Figure 4.8 shows the results from 2D TGV reconstruction of subsampled spiral data. As expected, conventional minimum norm solutions exhibit aliasing artifacts, which get increasingly worse as the number of interleaves is decreased. On the other hand, TGV reconstructions are artifact free for all levels of acceleration.

Figure 4.9 demonstrates the application of 3D TGV to a 3D stack of undersampled spiral angiography data. 4 different timeframes from the time series are displayed, showing the wash-in phase of the contrast agent. Again, undersampling artifacts are visible in the minimum norm solutions which are removed with TGV.

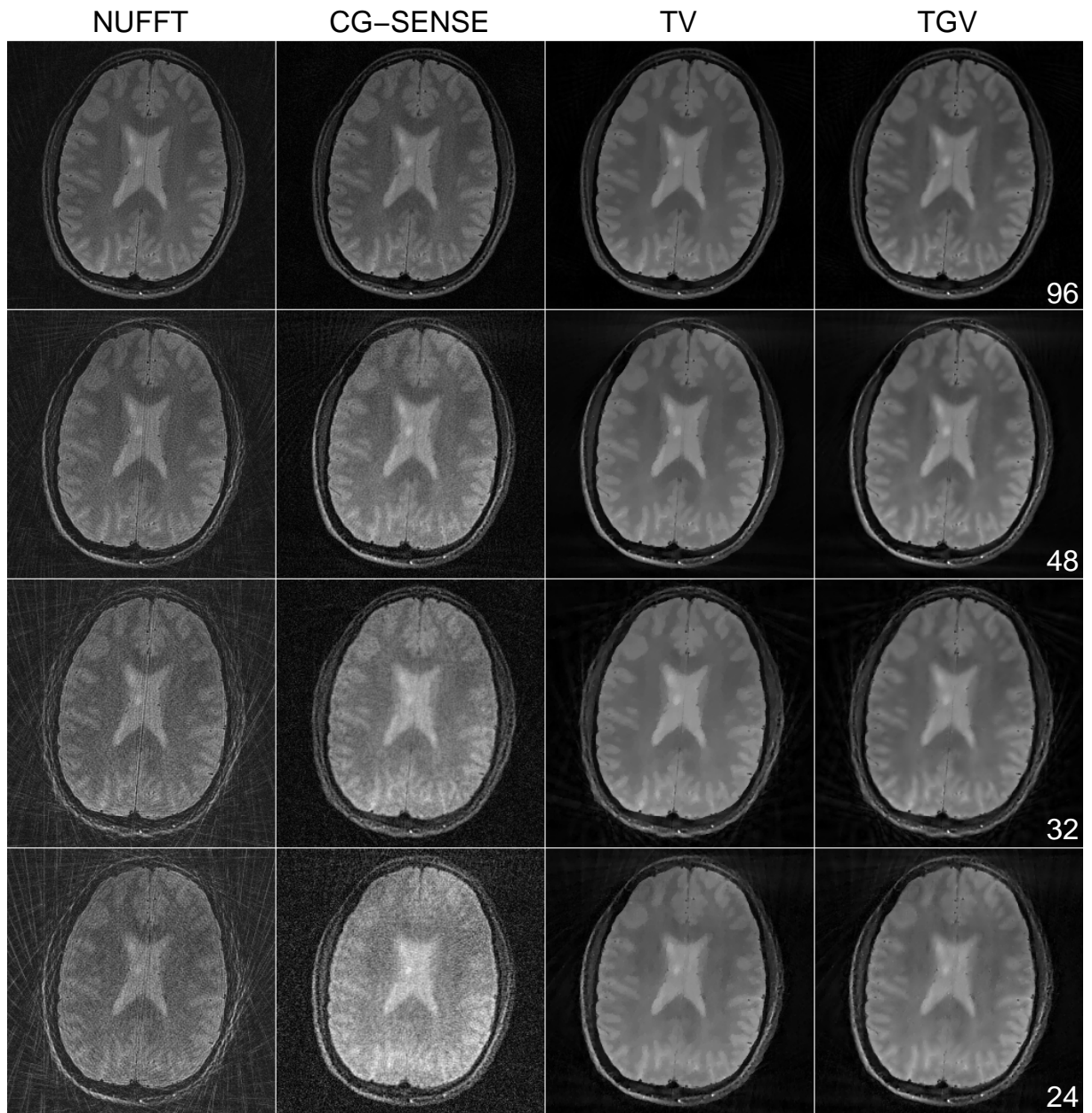


Figure 4.7: Radial image reconstructions of accelerated measurements of the human brain (256×256 matrix) from 96, 48, 32 and 24 projections. The columns depict conventional NUFFT reconstructions (left), reconstructions with CG-SENSE (middle left), with a TV constraint (middle right) and with a TGV constraint (right), respectively.

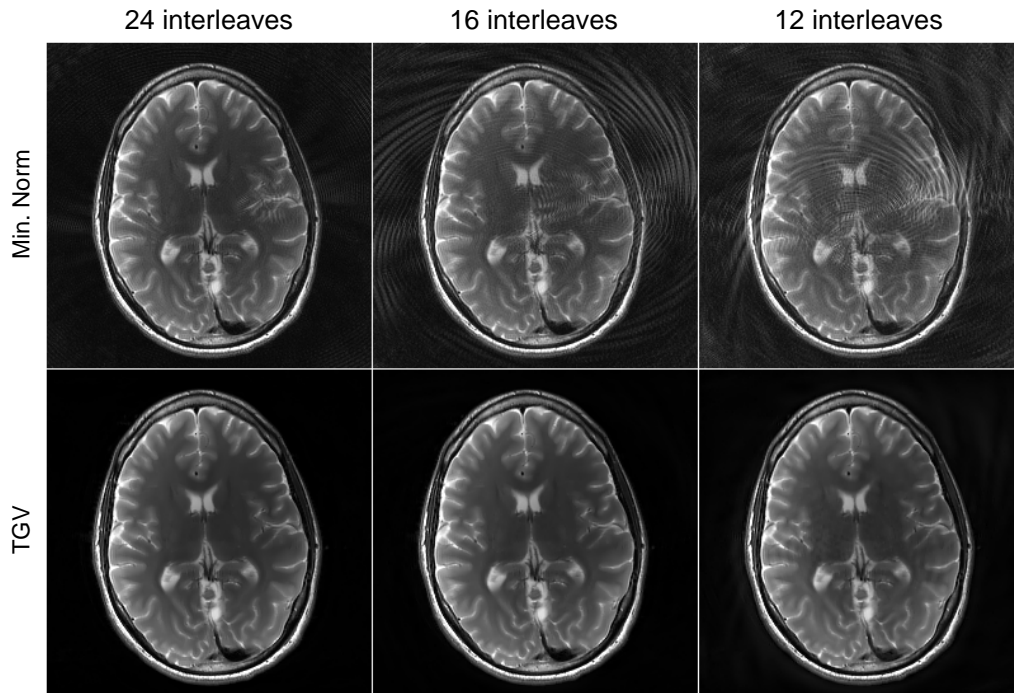


Figure 4.8: Reconstruction of subsampled spiral data of the brain. Conventional minimum norm solution (left column) and reconstruction with TGV regularization (right column). Results of undersampled data from 24, 16 and 12 spiral interleaves are shown.

4.5 Discussion

The results from this work demonstrate the advantages of TGV over conventional TV for both denoising and for constrained image reconstruction of undersampled data. While this is no real surprise for the results in Figure 4.3 because the TV assumption was violated in these cases, it is notable that even with quite homogeneous data sets like in Figures 4.4, 4.5, 4.6 and 4.7, TV introduces additional staircasing artifacts which lead to a more blocky, less faithful result when compared to the original image because the underlying assumption of piecewise constancy does not follow the underlying signal from the tissue that well. However, it must be noted that in some situations, the cartoon type, piecewise constant features of TV might actually be desirable. For example, the interfaces between gray and white matter in in the magnified view of Figure 4.4 (third row) are artificially enhanced with the use of TV. Although TGV is also edge-preserving (as can be seen by comparing the sharp edges of TV and TGV at the periphery of the brain), this effect gives TV results a slightly “sharper” visual appearance. In the case of image reconstruction this effect can be noticed in Figure 4.6. Again, the edges and piecewise constant regions introduced in the TV results are more emphasized in comparison to the TGV results and even the original image.

As both TV and TGV introduce model based a-priori information, it is possible that this leads to losses in certain parts of the image, or the introduction of unwanted features. One example is highlighted by arrows in the second row of Figure 4.4. In this particular case, noise corruption resulted in a group of bright pixels, which were not eliminated during denoising.

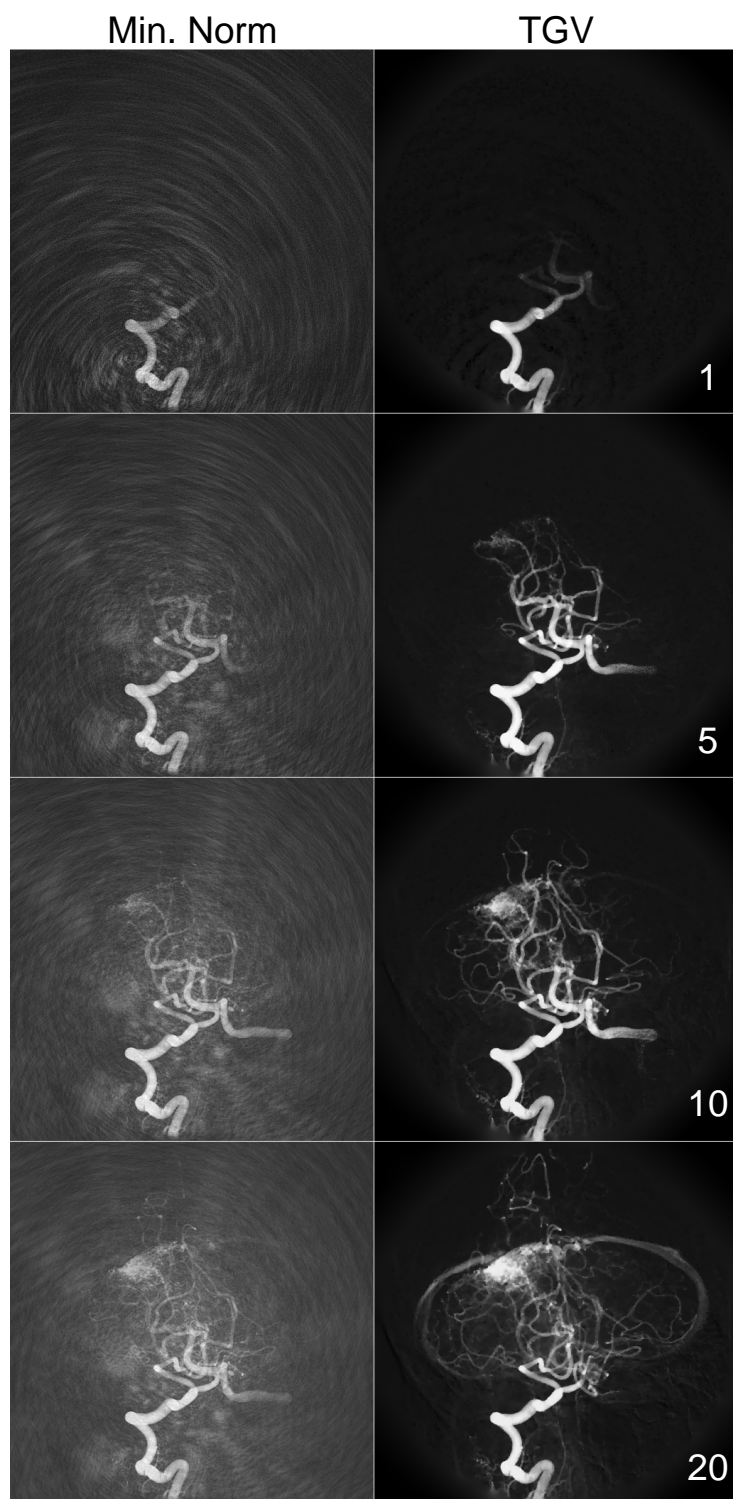


Figure 4.9: Reconstruction of subsampled spiral data of synthetic MR-angiography data generated from a projection X-ray measurement. Conventional minimum norm solution (left column) and reconstruction with TGV regularization (right column). Timeframes 1, 5, 10 and 20 are displayed.

Therefore a bright spot remains in the denoised images, which might even be misinterpreted as a lesion. Of course this spot is also visible in the noisy image, but in this case a radiologist would be aware of the low SNR and be reluctant to base a diagnosis on such an image. The same holds true for fine details that are buried below the noise level. While it is possible to eliminate the noise, these features cannot be recovered. Therefore, if denoising is used, radiologists should always have access to the noisy data, too. In this way it is possible to identify wrong image features and missing details more easily, and an unjustified overestimation of the diagnostic value of the images can be prevented.

It is obvious that both variational approaches (TV and TGV based) clearly outperform conventional L^2 based parallel imaging. Comparable image quality is only achieved for moderate undersampling (96 projections for the 12 channel data set (Figure 4.7), 32 projections in the case of the 32 channel data (Figures 4.5, 4.6). Of course, if the degree of undersampling is too high, some features may be buried without chance of recovery with either method. The cases where extremely high undersampling is performed (e.g. using only 12 projections) in Figures 4.5 and 4.6 demonstrate these limits of the method.

4.5.1 Choice of the Regularization Parameter

TGV, like TV, needs a proper balancing between the regularization term and the data fidelity term. Overweighting of the TGV term removes image features while under weighting leads to residual noise or streaking artifacts in the image. In our current implementation, the right amount of regularization is determined in the following way. We start with very low regularization and then increase the parameter step by step until noise or artifacts are eliminated from the resulting image. An alternative would be the use of automatic strategies like L-curve [83] or discrepancy principles [84], which is the subject of future investigations. For the calculations of this work, the following weights were used: $\lambda = 0.02$ for prostate denoising (Figure 4.3), $\lambda = 0.01$ for brain denoising (Figure 4.4) and $\lambda = 8 \cdot 10^{-5}$ for all image reconstruction experiments, regardless of undersampling and the selected data set (Figures 4.5, 4.6, 4.7). Figure 4.10 demonstrates the influence of the regularization parameter on the reconstructed images for denoising and image reconstruction. Results with proper regularization, over-regularized ($\lambda_{\text{high}} = 5 \cdot \lambda_{\text{proper}}$) and under-regularized ($\lambda_{\text{low}} = 1/5 \cdot \lambda_{\text{proper}}$) images are shown. In the case of denoising, overweighting causes pronounced losses of object detail while residual noise remains in the image in the under regularized case. In contrast, image reconstruction is much more robust with respect to changes of the regularization parameter, which is an important condition when considering application in clinical practice. This also explains why excellent results were achieved with a “default” parameter for two different data sets and multiple levels of subsampling in the case of image reconstruction, while individual tuning had to be performed for denoising. The reason for this behavior is that in the case of image reconstruction the constraints (TV or TGV) only augment artifact reduction, while the main a-priori information is given by the coil sensitivity maps. This is illustrated by the fact that for moderate acceleration factors (32 projections for the 32 channel data set), reasonable reconstructions can be obtained with conventional CG-SENSE. In contrast, in the case of the denoising problem, the image model (TV or TGV) is the only a-priori information that controls the reconstructed image.

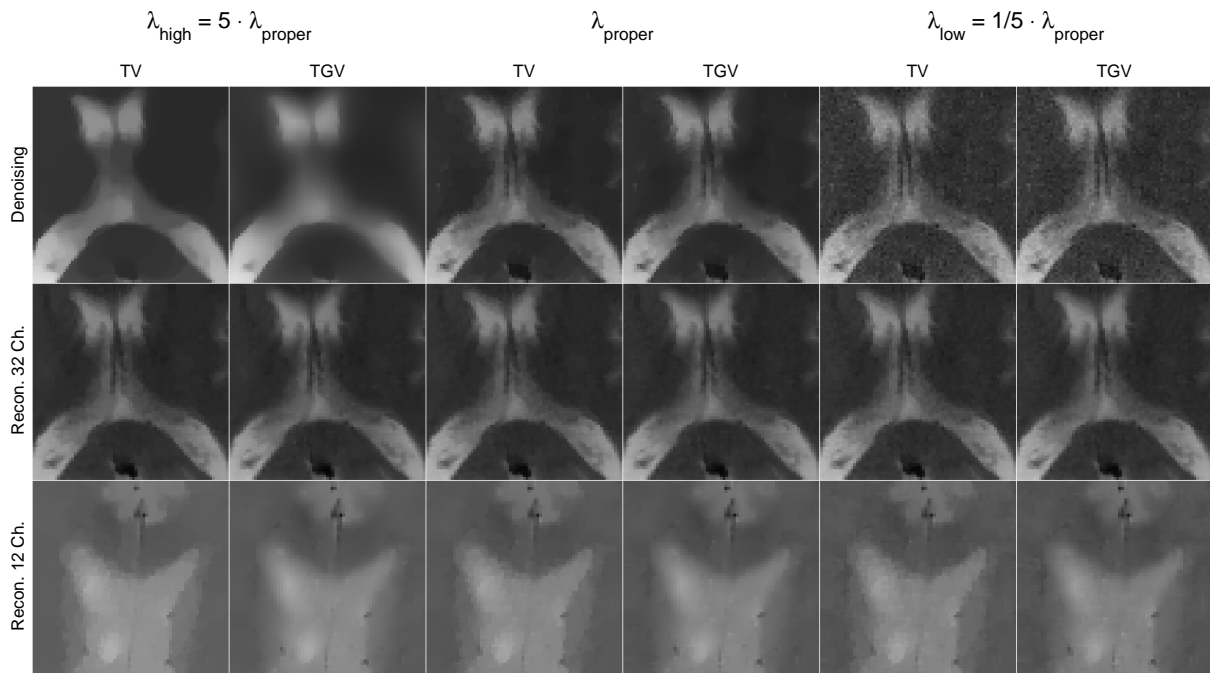


Figure 4.10: Denoising (top row) and radial image reconstruction with 32 radial projections (256×256 matrix) from the downsampled (middle row), and the in-vivo accelerated (bottom row) experiments. Results with a high regularization weight (left), an appropriate weight (middle) and a low weight (right) are shown.

4.5.2 Computational Requirements

The computational load of the proposed TGV models is essentially that of solving the respective minimization problems numerically. These constitute non smooth convex optimization problems in high-dimensional spaces with degrees of freedom determined by the number of pixels in the image. Due to the extensive mathematical study of this problem class, efficient and robust abstract algorithms are available.

In our Matlab implementation, which can be run on recent desktop PCs and notebooks, we decided to use rather simple general purpose methods in order to show that the adaptation to TGV does not require much effort in code development. This served as the basis for the CUDA implementation which was designed to run on every PC with a recent NVIDIA graphics processing unit. While the algorithms for TGV and TV are essentially similar, one minor drawback of TGV in comparison to TV is the slightly higher computational load arising from the need to update more variables in each iteration step compared to the respective TV method. Our observations are that the NUFFT constitutes the main part of the computational effort and hence, TGV reconstruction needs only slightly more computation time than TV reconstruction (roughly the factor 1.1 in our proof-of-principle implementation). While this means that TGV currently can only be used in applications where offline image reconstruction or postprocessing is acceptable, this is the case for many iterative TV or compressed sensing methods, too.

As it has also been observed for TV based artifact elimination [24], TGV offers great possibilities of acceleration through parallelization. Using our CUDA-based implementation, the TGV

reconstruction times of the radial reconstructions of the 32 channel data (Figure 4.5) and the 12 channel data (Figure 4.7) are displayed in Table 4.1. Calculations were performed on a conventional desktop PC (Intel Core 2 DUO E6600 2.40GHz, 2GB RAM). The CUDA implementation was compiled with release 3.0 of the NVCC compiler and was tested on a NVIDIA GTX480 GPU with 1536MB memory. For this test of computation time, the number of iterations of the reconstruction was based on visual inspection of the image quality. The reconstruction was stopped when further iterations did not change the visual appearance of the reconstructed image any more.

4.5.3 Extensions

Another advantage of TGV belonging to the well-examined class of convex regularization functionals is its versatile applicability to all kinds of variational problems. Roughly speaking, it can basically be used in all MRI applications in which the image is subject to optimization, in particular those where TV has already shown to work.

It is possible to use TGV as a regularizer that can be applied directly to array coil data of individual receiver channels. Thus, TGV can be used in combination with all parallel imaging reconstruction methods that first generate individual coil images, which are then combined to a single sum of squares image in the last step, like GRAPPA [4]. This is not easily possible with conventional TV because prior to the sum of squares combination, the individual coil images are still modulated with the sensitivities of the receiver coils which will lead to considerable staircasing artifacts, as illustrated in Figure 4.2.

Radial Sampling was chosen as the primary application for image reconstruction in this chapter, but of course it is also possible to use TGV as a penalty term for randomly subsampled data sets or for data that was not acquired with phased array coils, following the approach of compressed sensing [16].

Another promising application for TGV would be diffusion tensor imaging. Currently, TGV is only defined for scalar functions, but as symmetric tensor fields are inherent in the definition,

Table 4.1: CUDA Reconstruction times of experiments with radial subsampling. Data sets with 12 (Figure 4.7) and 32 (Figure 4.5) channels with different numbers of spokes were used.

Data set	Number of iterations	Reconstruction time (seconds)
32ch 32 projections	150	26.56
32ch 24 projections	200	30.47
32ch 16 projections	300	38.12
32ch 12 projections	400	45.62
12ch 96 projections	200	28.56
12ch 48 projections	400	35.40
12ch 32 projections	600	41.50
12ch 24 projections	800	47.91

it can be easily extended to higher order tensor fields and could therefore be used as a regularizer to reconstruct the diffusion tensor.

Let us finally mention that the TGV framework is independent of the space dimension and can thus as well be applied to the denoising/reconstruction of 3D image stacks taking full spatial information into account. The implementations can be extended without greater effort, however, an increase in computational complexity in comparison to sequential 2D processing has to be expected, especially in the case of image reconstruction, with 3D regridding being performed in each iteration step. For denoising applications, nevertheless, these kinds of problems do not occur.

4.6 Conclusions

This work presents TGV for MR imaging, a new mathematical framework which is a marked enhancement of the TV method. While it shares the existing desirable features of TV, it is not based on the limiting assumption of piecewise constant images. It is possible to use TGV in all applications where TV is used at the moment, and in the denoising and image reconstruction experiments of this work, it showed its important features to be able to follow the natural continuous signal changes of biological tissues and imaging methods. TGV is based on a solid mathematical theory within the framework of convex optimization, which ensures that numerical implementations are usually straightforward as a variety of numerical algorithms already exist for these types of problems. However, while both TV and TGV are effective penalty functions for denoising and image reconstruction, the use of a-priori information always introduces other biases in the images. This can lead to image content that is missed, as well as to the introduction of false image features. The diagnostic value of TGV-regularized images in clinical practice has to be investigated in future work.

Chapter 5

Parallel Imaging with Nonlinear Reconstruction using Variational Penalties¹

5.1 Introduction

It was shown recently that nonlinear inversion can be applied successfully to image reconstruction of undersampled data from multiple coils, i.e., parallel imaging [5, 6, 85, 86]. The joint estimation of images and coil sensitivities, which can be achieved with an iteratively regularized Gauss-Newton (IRGN) method, leads to more accurate estimations of the coil sensitivities, and therefore yields results with improved image quality. It was also demonstrated that this method can be extended to non-Cartesian imaging [87, 88]. In particular, radial sampling has the advantage that the sampling pattern automatically leads to an oversampling of the central frequencies of k -space, which eliminates the need to acquire additional reference lines when performing auto-calibrated parallel imaging.

Another important characteristic of radial sampling is the fact that aliasing artifacts, which are introduced in the case of undersampling, have a very different appearance than the image content. For this reason, it is possible to remove these so-called streaking artifacts during reconstruction with the integration of specific a-priori information about the structure of the image. For radial MRI, this has been demonstrated in conventional (linear) parallel imaging with the penalization of the total variation (TV) of the image [1]. The general strategy, which relies on the sparsity of the solution in some transform domain, has been formulated for pseudo random sampling patterns under the name of compressed sensing [14–16]; see also [89] for a related idea.

As demonstrated in this work, the formulation of autocalibrated parallel imaging as a nonlinear inversion problem yields a general framework that allows the integration of such additional a-priori information. This is illustrated with the integration of a TV penalty in the IRGN

¹This chapter is based on the publication *Nonlinear Parallel Imaging with Variational Penalties*, , *Magnetic Resonance in Medicine (2011)* [23].

method. The method then combines both concepts, the integration of a-priori knowledge with appropriate regularization terms and the joint estimation of coil sensitivities and image content. In general, the integration of a TV term helps to suppress the noise amplification [18] that seriously limits parallel imaging with conventional methods. When applied to data sets obtained with radial or pseudo random sampling patterns, this also leads to enhanced removal of artifacts. Additionally, it is shown that the flexibility provided by this framework easily allows replacing TV with another regularization functional in cases when the TV assumption of piecewise constant images is not reasonable; for instance, total generalized variation (TGV) of second order [22, 80] that was presented in the previous chapter.

5.2 Theory

Mathematically, parallel MR imaging can be formulated as a nonlinear inverse problem where the sampling operator \mathcal{F}_S (defined by the k -space trajectory, e.g., Fourier transform followed by multiplication with a binary mask for standard Cartesian subsampling) and the correspondingly acquired k -space data $s = (s_1, \dots, s_N)^T$ from N receiver coils are given, and the spin density u and the unknown (or not perfectly known) set of coil sensitivities $c = (c_1, \dots, c_N)^T$ have to be found such that

$$F(u, c) := (\mathcal{F}_S(u \cdot c_1), \dots, \mathcal{F}_S(u \cdot c_N))^T = s \quad (5.1)$$

holds. As was shown in [6, 87], this problem can be solved using the iteratively regularized Gauss-Newton (IRGN) method [83, 90–92], i.e., computing in each step k for given $x^k := (u^k, c^k)$ the minimum $\delta x := (\delta u, \delta c)$ of

$$\min_{\delta x} \frac{1}{2} \|F'(x^k)\delta x + F(x^k) - s\|^2 + \frac{\alpha_k}{2} \mathcal{W}(c^k + \delta c) + \beta_k \mathcal{R}(u^k + \delta u) \quad (5.2)$$

for given $\alpha_k, \beta_k > 0$, and then setting $x^{k+1} := x^k + \delta x$, $\alpha_{k+1} := q_\alpha \alpha_k$ and $\beta_{k+1} := q_\beta \beta_k$ with $0 < q_\alpha, q_\beta < 1$. Here, $F'(x^k)$ is the Jacobian of F evaluated at x^k . The term $\mathcal{W}(c) = \|Wc\|^2 = \|w \cdot \mathcal{F}c\|^2$ is a penalty on the high Fourier coefficients of the sensitivities and \mathcal{R} is a regularization term on the image. So far, the application of the IRGN method to parallel imaging has been formulated with a conventional L^2 penalty [6, 87] (i.e., $\mathcal{R}(u) = \frac{1}{2}\|u\|^2$). As demonstrated in this work, the IRGN method can also be used with other regularization terms, which can be chosen dependent on the application. For example, the stability of the method with respect to noise can be improved: Since α_k and β_k are decreasing during the iteration, the problem in (5.2) will become increasingly ill-conditioned. This leads to noise amplification, which can be counteracted by using a regularization term with stronger noise removal properties than the L^2 penalty. A typical choice is the total variation (TV) of the image, i.e.,

$$\mathcal{R}(u) = \int |\nabla u|_2 dx, \quad (5.3)$$

where $|\cdot|_2$ denotes the Euclidean norm in \mathbb{R}^2 .

Since TV regularization is known to introduce staircasing artifacts if the penalty parameter is large, we also investigated the use of second order total generalized variation (TGV) [22, 80] (see chapter 4) as a regularization functional for the IRGN method. This amounts to setting

$$\beta \mathcal{R}(u) = \inf_v \beta \|\nabla u - v\| + 2\beta \|\mathcal{E}v\|, \quad (5.4)$$

where $\mathcal{E}v = \frac{1}{2}(\nabla v + \nabla v^T)$ denotes the symmetrized gradient of the complex-valued vector field $v \in C^1(\Omega; \mathbb{C}^2)$. We refer to chapter 4 and [22, 80] for a detailed description of this functional and an explanation of its properties.

5.3 Materials and Methods

5.3.1 Data Acquisition

Experiments were performed for radial as well as pseudo random sampling patterns. All measurements were performed on a clinical 3T system (Siemens Magnetom TIM Trio, Erlangen, Germany). Written informed consent was obtained from all volunteers prior to the examination.

Pseudo random sampling was tested with phantom experiments and in-vivo measurements of the brain of healthy volunteers. A receive-only 12 channel head coil was used, and an SVD based coil compression (section 2.7.3, [49]) was applied to reduce the data to 8 virtual channels for the phantom measurements and 9 in the case of the in-vivo experiments. Measurements were performed with a 3D FLASH sequence with the following sequence parameters: TR=20ms, TE=5ms, flip angle 18° , matrix size $256 \times 256 \times 256$. The pulse sequence was modified to include a binary 2D mask defining the subsampling of both phase-encoding directions. Pseudo random patterns were generated with the adaptive procedure to account for the energy distribution in k -space that was described in chapter 3. For the phantom experiments, a resolution of $1\text{mm} \times 1\text{mm} \times 5\text{mm}$ was used. The in-vivo measurements were obtained with an isotropic spatial resolution of 1mm. Raw data was exported from the scanner, a 1D Fourier transform was performed along the readout direction, and partitions orthogonal to this axis were reconstructed.

Additionally, a fully sampled T_2 weighted 2D turbo spin echo data set of the brain of a different volunteer was acquired with a 32-channel receive coil. The data was again compressed to 12 virtual channels. Sequence parameters were TR=5000ms, TE=99ms, turbo factor 10, matrix size 256×256 , slice thickness 4mm and an in-plane resolution of $0.86\text{mm} \times 0.86\text{mm}$. Raw data was exported from the scanner and then subsampled retrospectively with an adapted pseudorandom sampling pattern. This experiment was conducted to have a fully sampled gold standard image, which can then be compared to the two different reconstruction strategies.

Radial sampling experiments were performed with an rf-spoiled radial FLASH sequence with sequence parameters TR=2.0ms, TE=1.3 ms, and a flip angle of 8° . Images of a water phantom and of the heart of a healthy volunteer were made. The acquisition of the in-vivo data was performed with a protocol designed for real-time imaging [93–95] without cardiac gating and during free breathing [88, 96, 97] using a 32-channel body array coil. After the acquisition the data was compressed to 12 virtual channels for the in-vivo experiments and 8 virtual channels for the phantom experiments. An in-plane resolution of $2\text{mm} \times 2\text{mm}$ and a slice thickness of 8mm was used in combination with 128×128 image matrices. Due to the two-fold oversampling, this resulted in 256 sample points for each radial spoke.

5.3.2 Nonlinear reconstruction

All reconstructions were performed offline using a Matlab (R2010a, The MathWorks, Natick, MA, USA) implementation of the described nonlinear inversion method. For the reconstruction of radial data sets, Fessler and Sutton's NUFFT [33] code was used. To facilitate comparison, the solution of (5.2) with $\mathcal{R}(v) = \frac{1}{2}\|v\|^2$ was computed using the same extra-gradient scheme, which can be obtained from Algorithm 3 by removing step 4 and replacing the term $-\text{div}p$ with $+\beta u + \bar{\delta}u$ in step 6. In the following, we will refer to the Gauss-Newton reconstruction using an L^2 -penalty simply as IRGN, while the reconstruction using TV and TGV penalties will be denoted by IRGN-TV and IRGN-TGV, respectively.

5.3.3 Parameter Choice

The parameters in the Gauss-Newton iteration were chosen according to a quasi-optimality criterion. The initial penalties α_0, β_0 were chosen such that the norm of the residual $\|F(u^1, c^1) - s\|$ after the first iteration was roughly 3/4 of the initial residual, and the reduction factors q_α, q_β were set such that each further iteration roughly reduced the residual by a factor of 1/2. The iteration was terminated once the achieved reduction factor fell below 3/4. This led to the choice $\alpha_0 = 1, \beta_0 = 2, q_\alpha = q_\beta = 1/10$, and 5 Gauss-Newton iterations for the radial data set. For the pseudo random data set, $\beta_0 = 1, q_\beta = 1/5$ and 6 Gauss-Newton iterations were used.

Since the TV regularization parameter is continually decreased during the Gauss-Newton iteration, the final reconstruction will typically not show strong signs of TV-filtering such as a cartoon-like appearance. A more pronounced TV-effect can be achieved if the decrease of the regularization parameter is stopped at the desired level. To illustrate this, we will also show reconstructions where we have set $\beta_{k+1} = \max(5 \cdot 10^{-3}, q_\beta \beta_k)$ for L^2 , TV and TGV regularization (with otherwise unchanged parameters).

5.4 Results

Figure 5.1 shows a partition of a water phantom reconstructed with IRGN and IRGN-TV from pseudo randomly subsampled 3D data using acceleration factors $R = 4$ and $R = 10$. The reduced noise amplification and artifact removal characteristics of IRGN-TV are clearly visible for both acceleration factors. In the case of moderate acceleration with $R = 4$, the final TV regularization parameter β_{min} was set to zero. For $R = 10$, $\beta_{min} = 5 \cdot 10^{-3}$ was used to achieve a stronger TV regularization and a better removal of artifacts. It must be noted that the phantom only consists of regions that are piecewise constant, and therefore the underlying assumption of the TV penalty is fulfilled. However, in the case of $R = 10$ with increased TV regularization, staircasing artifacts can be observed in regions where modulations caused by the inhomogeneity of the coil sensitivities affect the reconstructed image.

The above findings are confirmed for in-vivo conditions. IRGN and IRGN-TV reconstructions (with $\beta_{min} = 0$) of the pseudorandomly subsampled T2 weighted turbo spin echo data of the brain are displayed in Figure 5.2, together with a sum-of-squares image obtained from the fully sampled data. Shown are results for acceleration factors of $R = 4, R = 6$ and $R = 8$. With larger

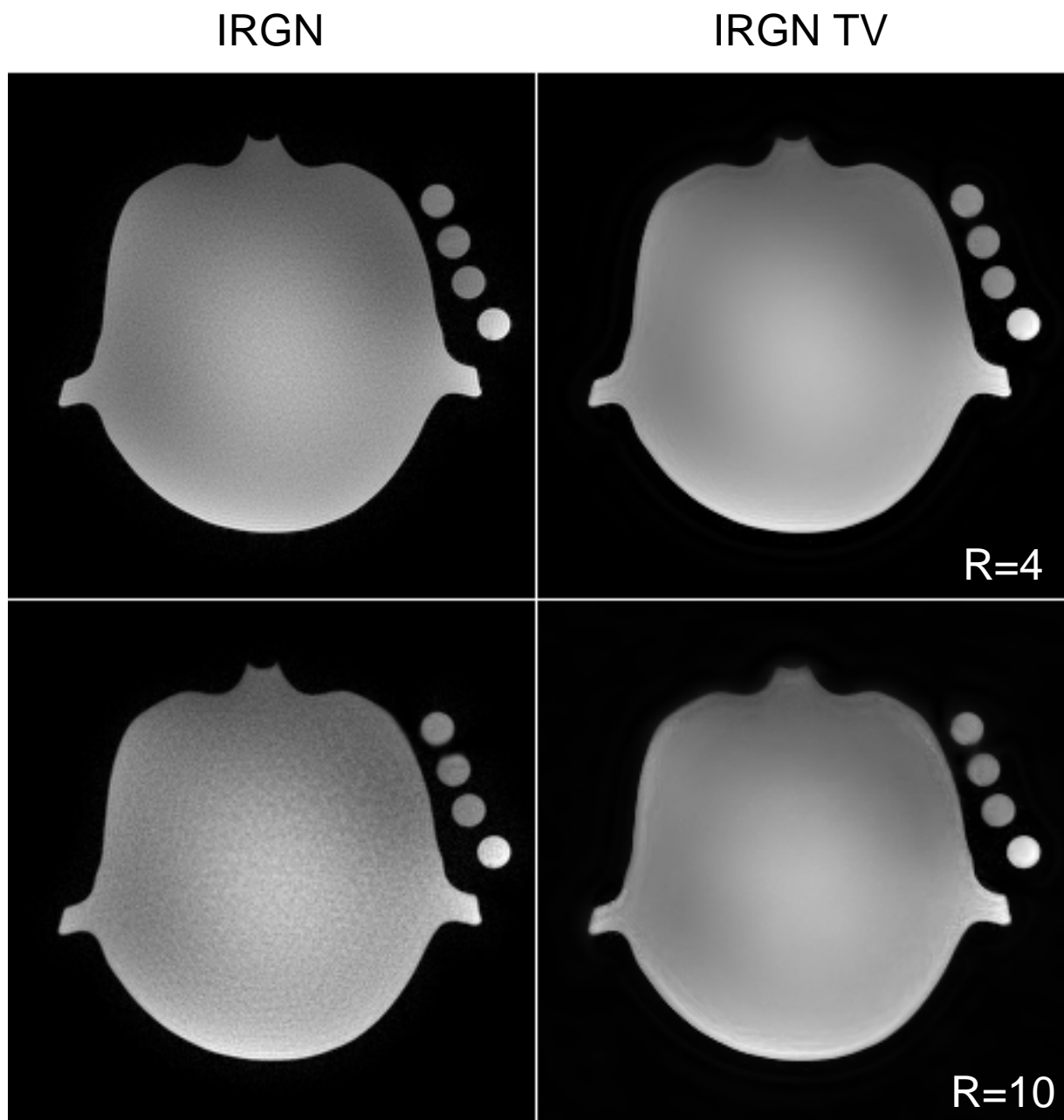


Figure 5.1: Reconstructions of pseudo random sampling, phantom data set. IRGN (left), IRGN-TV (right). Acceleration factors $R = 4$ (top, $\beta_{min} = 0$) and $R = 10$ (bottom, $\beta_{min} = 5 \cdot 10^{-3}$).

acceleration factors, an increasing amount of noise amplification and residual incoherent aliasing can be observed in the IRGN reconstructions, while this effect is reduced with IRGN-TV.

A partition of a human brain reconstructed from accelerated in-vivo pseudo randomly subsampled FLASH measurements is displayed in Figure 5.3. In this example, using a moderate acceleration of $R = 4$, β_{min} was again set to zero. Similar to the experiments with the phantom, a pronounced reduction of the noise can be observed in the image reconstructed with IRGN-TV as compared to the conventional IRGN reconstruction. As can be seen best in the enlarged image regions, image details are preserved well in the IRGN-TV reconstruction.

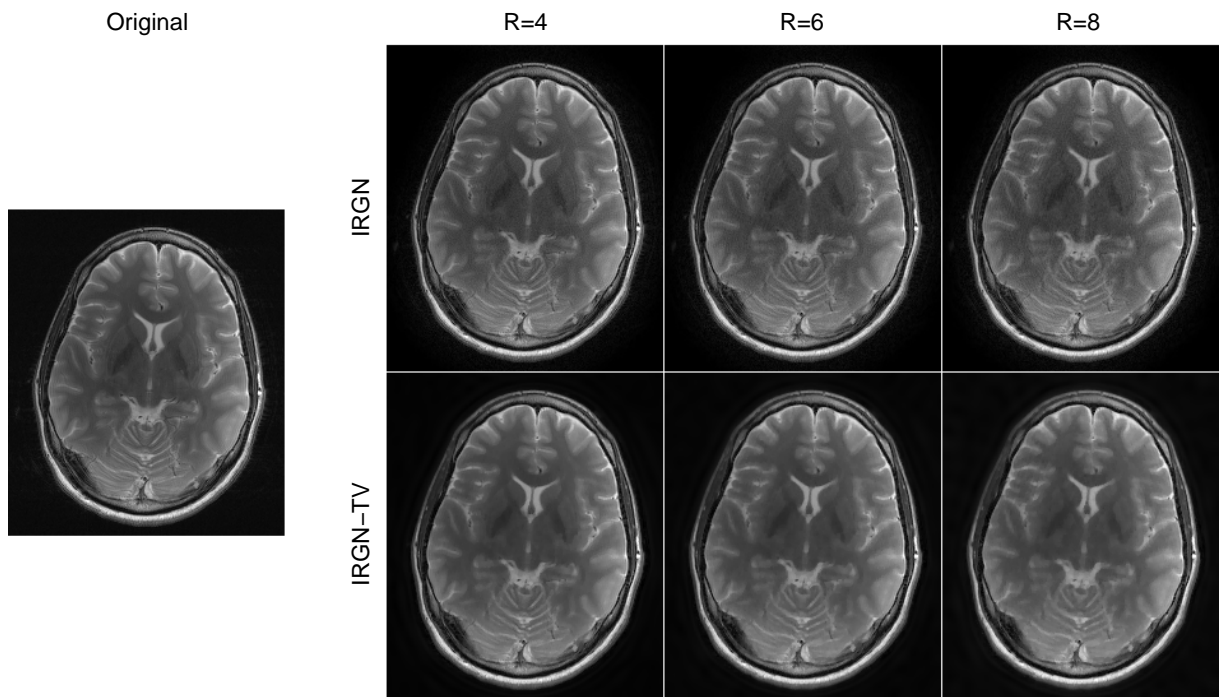
Figure 5.4 shows two slices of a water phantom acquired with subsampled radial measurements and reconstructed with IRGN and IRGN-TV. Here, 25 spokes were acquired to reconstruct a 128×128 matrix, corresponding to an undersampling factor of approximately 8 in comparison to a fully sampled radial data set ($128 \cdot \frac{\pi}{2} \approx 201$ spokes). Because of the high undersampling and due to the fact that only 8 virtual channels were used during the reconstruction, an increased value of $\beta_{min} = 5 \cdot 10^{-3}$ was used in this example. Both slices show reduced noise and streaking artifacts when IRGN-TV is used. However, one of the images (top row in Figure 5.4) again exhibits staircasing artifacts for the IRGN-TV solution.

Reconstructions of real-time images of the beating heart are displayed in Figure 5.5. Results for 25 ($R \approx 8.0$), 21 ($R \approx 9.6$) and 19 ($R \approx 10.6$) acquired spokes are shown. These acceleration rates allow image acquisition times of 50ms, 41ms and 38ms, corresponding to dynamic update rates of 20, ≈ 24 and ≈ 26 frames per second. For all reconstructions, $\beta_{min} = 5 \cdot 10^{-3}$ was used. The image reconstructed from the 25 spokes data set does not show streaking artifacts for both IRGN and IRGN-TV. However, noise amplification is much stronger in case of IRGN. In contrast, reconstructions from 21 and 19 spokes show residual streaking artifacts due to increased subsampling, which are again reduced in the images reconstructed with IRGN-TV.

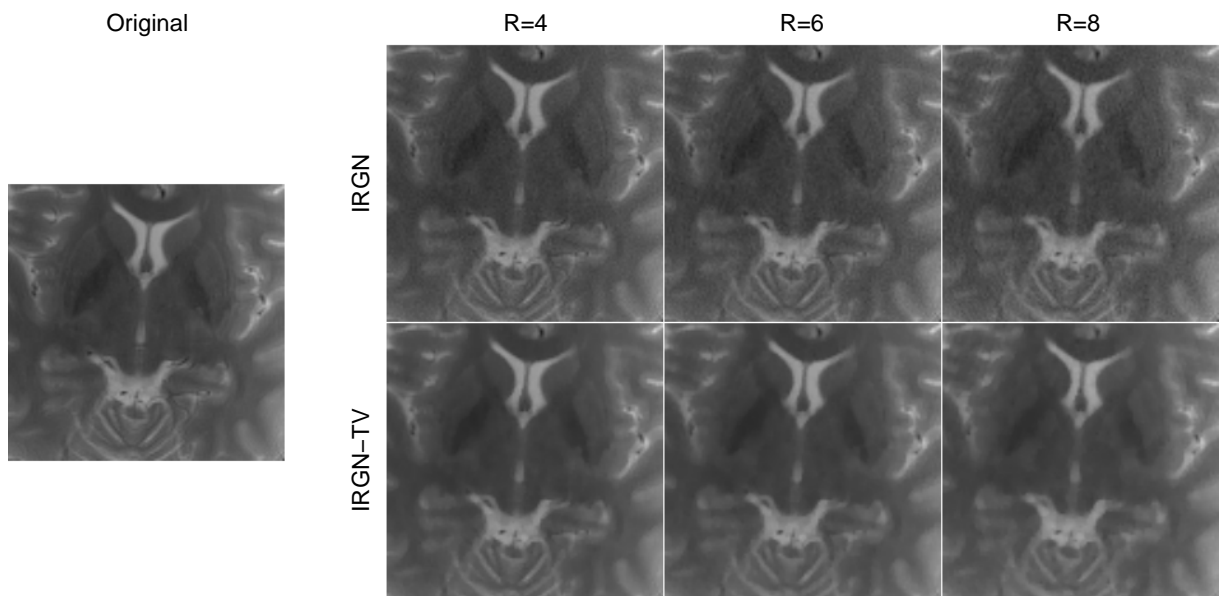
Finally, the effect of TGV regularization is demonstrated in Figure 5.6. It shows highlighted regions of both phantom images affected by staircasing artifacts (pseudo random and radial sampling, see Figures 5.1 and 5.4) using TV as well as TGV regularization, both with $\beta_{min} = 5 \cdot 10^{-3}$. The staircasing artifact is completely removed in the reconstruction with the IRGN-TGV method.

5.5 Discussion

The results from this work clearly demonstrate that pronounced improvements in reconstruction quality of parallel imaging with nonlinear inversion can be achieved with TV and TGV based regularization instead of a simple L^2 penalty. If moderate acceleration is used (Figures 5.1, case of $R = 4$, 5.2, and 5.3), TV serves as a stabilization term against noise amplification, which, otherwise, limits the practical use of parallel imaging to low acceleration factors. In cases where acceleration is pushed to its limits (Figure 5.1, case of $R = 10$; Figures 5.4 and 5.5), TV also leads to an additional removal of undersampling artifacts when combined with trajectories that produce incoherent aliasing. However, it must be noted that in this case, small image features with low contrast may also be removed during the reconstruction. This effect can be observed for some smaller structures, which are highlighted in Figure 5.5. It can be seen in the top row



(a) IRGN and IRGN-TV reconstructions.



(b) Magnified details.

Figure 5.2: Comparison of IRGN (top row) and IRGN-TV (bottom row) for pseudorandom subsampling of the T_2 weighted brain dataset ($\beta_{\min} = 0$). From left: fully sampled acquisition, acceleration factors $R = 4$, $R = 6$, $R = 8$.

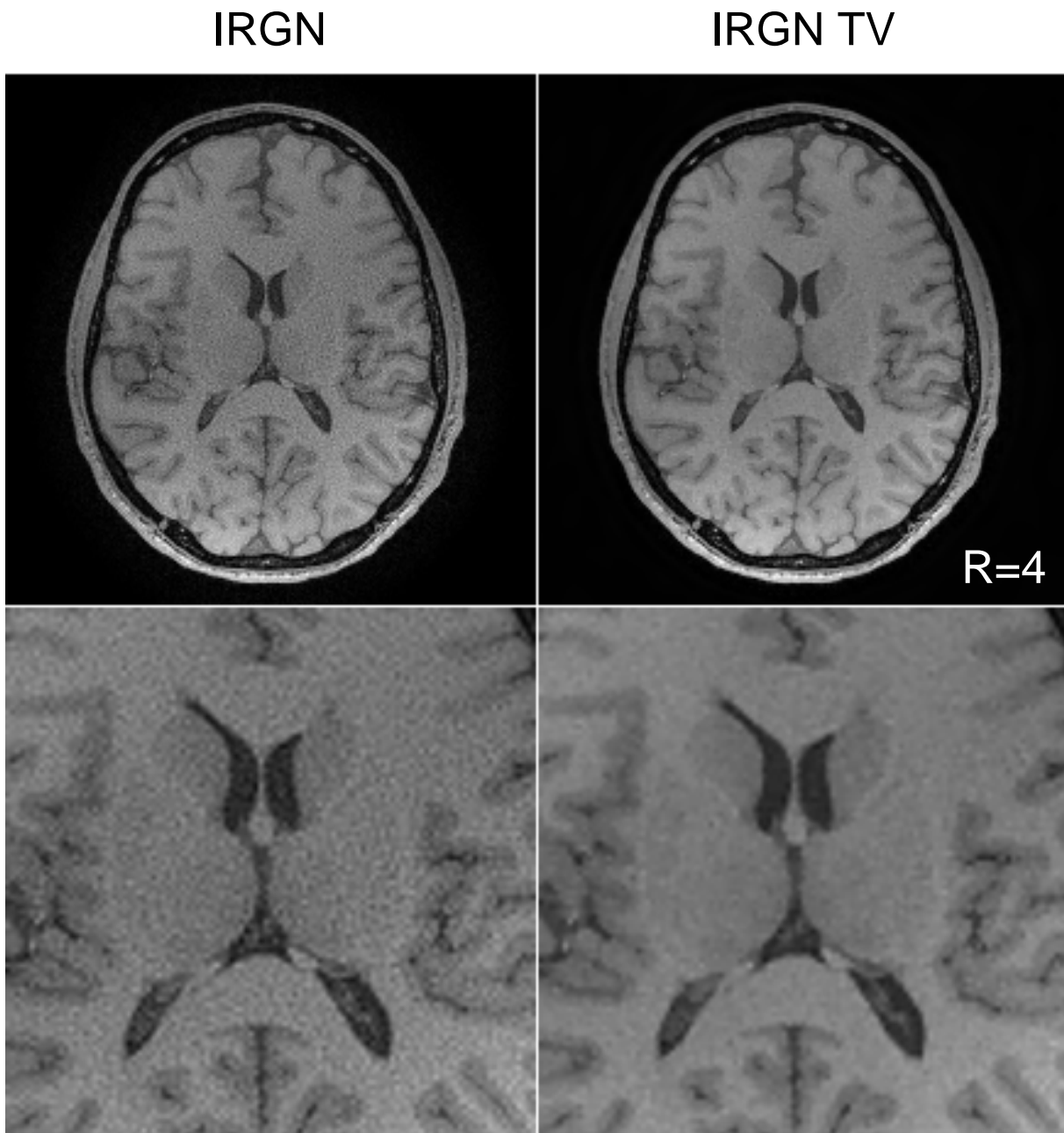


Figure 5.3: Reconstructions of pseudo random sampling, brain data set. IRGN (left) and IRGN-TV (right). Acceleration factor $R = 4$, $\beta_{min} = 0$.

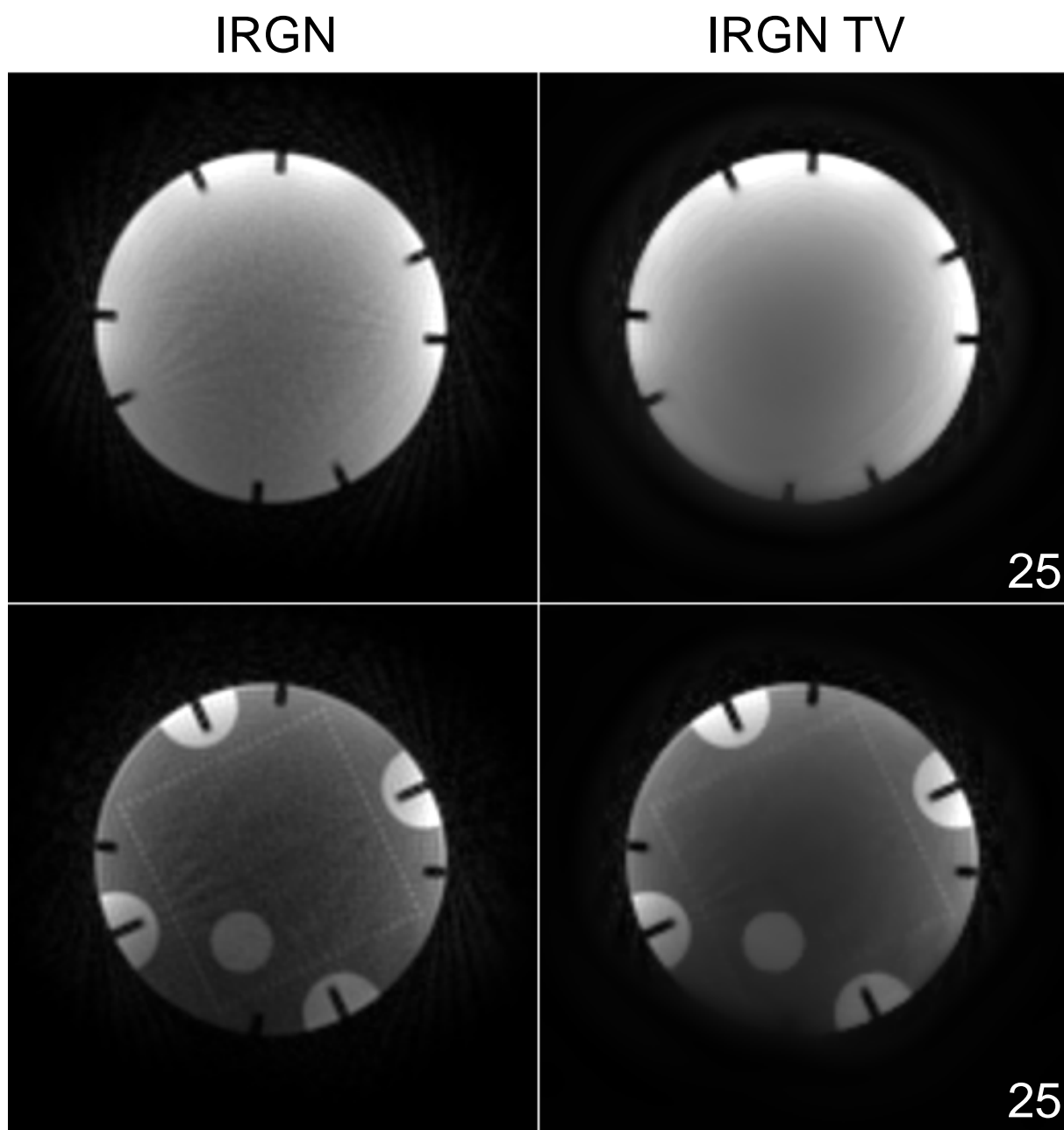


Figure 5.4: Reconstructions of radial sampling, phantom data, two different slices. IRGN (left) and IRGN-TV (right). 25 spokes were used for the reconstruction of a 128×128 image, $\beta_{min} = 5 \cdot 10^{-3}$.

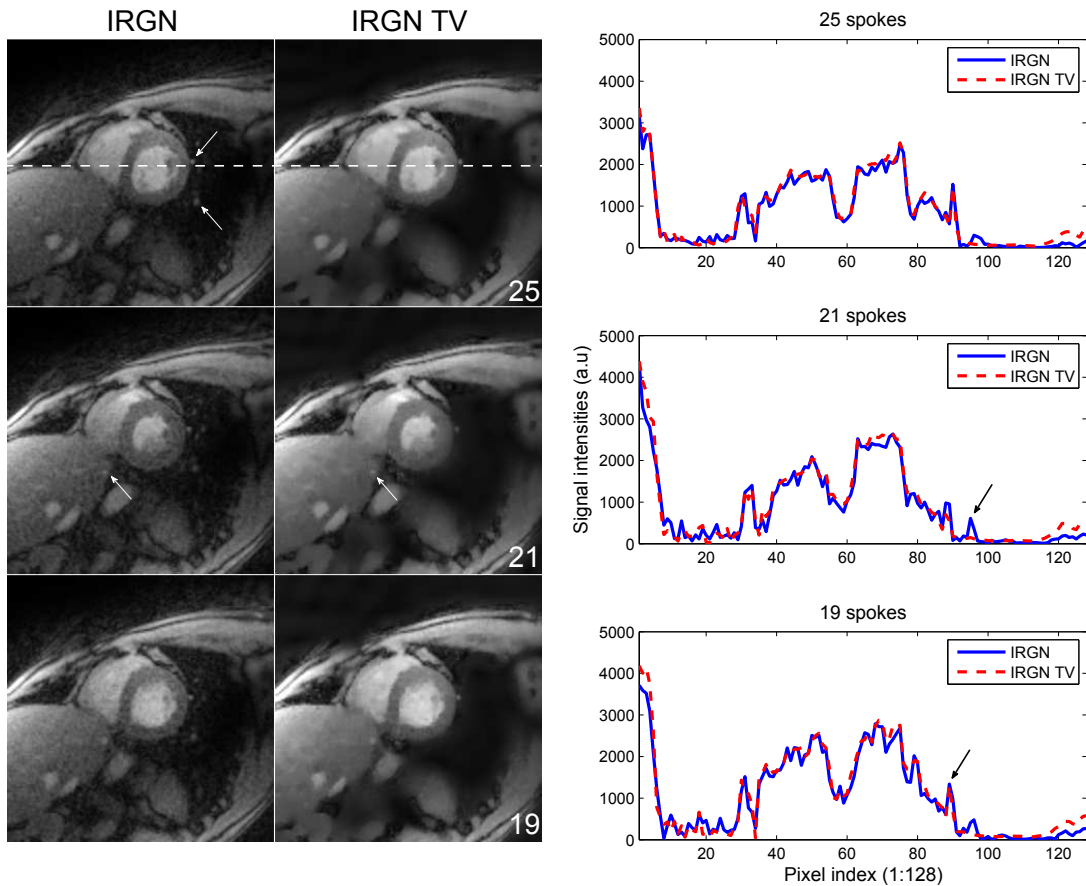


Figure 5.5: Comparison of IRGN (left) and IRGN-TV (middle) for radial real-time imaging of the beating human heart without cardiac gating and during free breathing ($\beta_{\min} = 5 \cdot 10^{-3}$). Top: 25 spokes. Highlighted are structures with little signal intensity that can be lost due to strong TV regularization. Middle: 21 spokes. Highlighted are structures of similar size but slightly higher signal intensity that are preserved even in case of TV regularization. Bottom: 19 spokes. The plots on the right show signal intensities across a horizontal line, indicated in the top row of the reconstruction results. The ability of IRGN-TV to preserve sharp edges is highlighted in the plot of the reconstruction from 19 spokes. The arrow marks the sharp border of the ventricle, which is depicted equally well with IRGN and IRGN-TV. The undesired loss of a small structure is highlighted in the plot of the reconstruction from 21 spokes. The plot crosses two adjacent vessels, which are both represented in the IRGN solution, but only the left one appears in the IRGN-TV reconstruction.

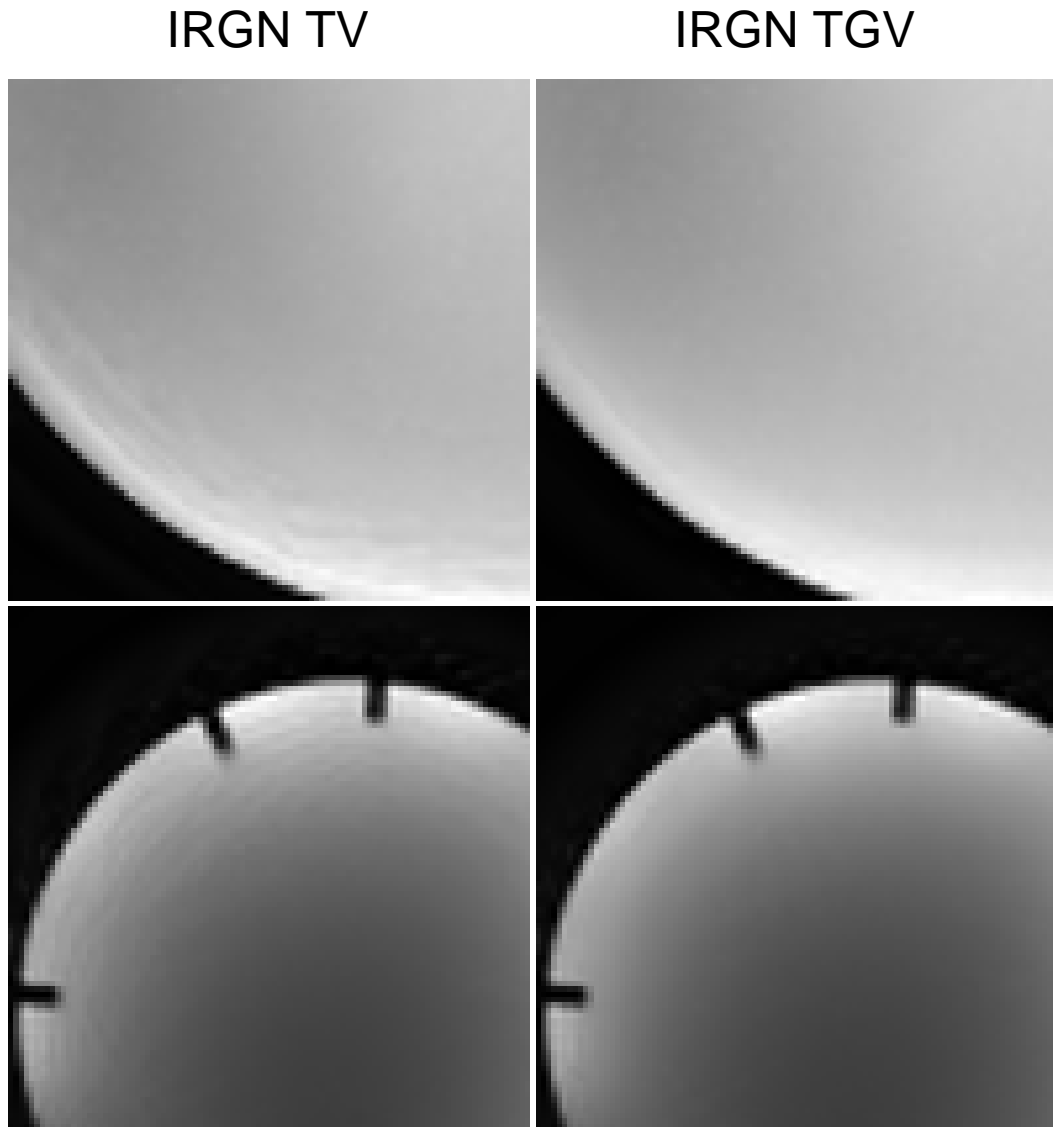


Figure 5.6: Comparison of conventional TV (left) and TGV (right) regularization for phantom experiments where modulations from the coil sensitivities lead to pronounced staircasing artifacts when TV is applied. Left: magnified regions from Figures 5.1 ($R=10$, top) and 5.4 (bottom); right: IRGN-TGV reconstruction of the same data set (with $\beta_{min} = 5 \cdot 10^{-3}$).

that structures with low signal, which are still visible in conventional IRGN reconstructions, are removed when TV is applied. However, as indicated by the highlights in the middle row, objects with a slightly higher signal intensity, even though of same size, are preserved in both reconstructions. These effects are also represented in the cross-sectional plots. The elimination of structures like noise or residual streaking artifacts is visible as a reduced amount of high frequency oscillations in the IRGN-TV plots. Note that due to the nature of TV, blurring of sharp edges does not occur. This can be observed, e.g., at the sharp border of the ventricle, which is preserved equally well with IRGN and IRGN-TV.

Our Matlab implementations reconstructed a single slice in a few minutes, where IRGN-TV took roughly 10% more time than IRGN (and similarly, IRGN-TGV was about 10% slower than IRGN-TV). It is possible to exploit the differentiability of the data consistency term to apply more efficient minimization algorithms such as the method of conjugate gradients in the case of IRGN or order optimal convex minimization methods such as those investigated in [98] for IRGN-TV and IRGN-TGV. Because this work focused on the effect of the different regularization techniques on image quality, the same primal-dual extra-gradient method was used as inner algorithm in all cases to allow a direct comparison for identical parameter choices. In this context, it should be noted that the parameters for the iteratively regularized Gauss-Newton method were independent of the chosen regularization term, and only depended on the trajectory type. Similarly, since the norm of the forward operator is estimated in the algorithm, the fixed parameters for the primal-dual extra-gradient methods were independent of the data set.

In this work, the flexibility to include different regularization terms was demonstrated on 2D examples, where each image (slice, i.e., 2D partition of a 3D data set, or frame of a time series) had been reconstructed individually. While computationally more demanding, the extension of the penalties into a third space or time dimension should further improve the image quality. For example, earlier work has shown that residual streaking artifacts in radial imaging can be removed with the use of a median filter in the time dimension when using an interleaved k-space sampling scheme [88]. Since the median filter can be interpreted as solving an L^1 minimization problem, it is expected that the inclusion of a corresponding penalty – either in the form of an L^1 penalty on the difference between the current and previous slice or frame, or of a higher-dimensional T(G)V penalty on the full data set – will yield even better results. The resulting convex minimization problems can be solved using the same primal-dual extra-gradient method as employed in this work.

Another possible extension of this work is the integration of additional information about the physical signal model into the functional in (5.2). An important application is mapping of relaxation parameters in multi echo sequences [99,100]. Here, the framework of nonlinear inverse problems makes it straightforward to perform parameter identification during the reconstruction.

5.6 Conclusions

This chapter describes an approach to include additional variational penalties in parallel imaging with nonlinear inversion. The presented algorithms combine the advantages of nonlinear inver-

sion, i.e., improved image quality through a better estimation of the coil sensitivities, with the advantageous properties of TV-based regularization terms. In addition to reducing the noise, the regularization is able to remove undersampling artifacts when combined with sampling strategies that produce incoherent aliasing, such as radial and pseudo random sampling.

Chapter 6

Fast Reduction of Undersampling Artifacts in Radial MR Angiography with 3D Total Variation on Graphics Hardware¹

6.1 Introduction

The time window for data acquisition in contrast enhanced MR angiography (CE-MRA) is limited due to the passage of the contrast agent. Additionally, a high spatial resolution is needed to visualize small vessels, while high temporal resolution is necessary to capture the dynamics of the contrast agent bolus. However, due to fundamental properties of MRI, there is always a trade off between spatial and temporal resolution. As MRI data acquisition is sequential, it can be accelerated by reducing the number of measurement steps, but this leads to artifacts in the reconstructed images because the Nyquist criterion (equation 2.12 in chapter 2) is violated.

The reconstruction strategies that were presented in the previous chapters use tailored acquisition strategies like radial sampling or randomized 3D sampling patterns and include a priori knowledge about the imaged objects and the coil sensitivities during the reconstruction process (see chapters 2 to 5). These algorithms allow the reconstruction of high quality images from highly undersampled data sets, but at the price of long computation times. While this is not a severe limitation during research, it makes them currently impossible to use in daily clinical practice.

Hansen et al. [101] and Sorensen et al. [102] have shown recently that it is possible to use the massively parallel streaming processor architecture of modern graphic processing units (GPUs) to speed up image reconstruction for parallel imaging and for the reconstruction of non-Cartesian data. The goal of this work was to show that for the special case of CE-MR angiography data sets, which feature a high contrast to noise ratio, it is possible to use TV algorithms with data fi-

¹This chapter is based on the publication *Fast reduction of undersampling artifacts in radial MR angiography with 3D total variation on graphics hardware*, *Magnetic Resonance Materials in Physics, Biology and Medicine (2010)* [24].

delity terms in image space, instead of integrating TV regularization in the image reconstruction process as in the previous chapters. As this eliminates the time consuming step of regridding the data in each iteration, primal-dual based TV formulations can be implemented very efficiently on the GPU, with computation times that make interactive elimination of undersampling artifacts possible. This is especially important for the interactive determination of the regularization parameter because a proper choice usually depends on patient-specific conditions like the geometry of the imaged anatomy, and therefore predefined settings may not deliver optimal results. It is also shown in this chapter that by using a special type of radial sampling, 3D a priori information can be included in the regularization process, which significantly improves image quality. While this leads to an even higher computational complexity, it becomes feasible with the GPU implementation.

6.2 Theory

6.2.1 Undersampled Radial Imaging and Total Variation

It is well known [26] that in order to reconstruct an $n \times n$ image matrix from a fully sampled radial data set, $\frac{\pi}{2} \cdot n$ radial projections have to be acquired. Reducing the number of projections accelerates data acquisition, but leads to characteristic streaking artifacts in the reconstruction. It was shown by Block et al. [1] that these streaking artifacts can be reduced efficiently by using a TV regularization in conjunction with a data fidelity term in k-space, a strategy that is comparable with compressed sensing approaches [16]. In contrast, the method that is presented in this chapter is based on the original TV approach formulated in image space. TV based minimization problems were originally designed for elimination of Gaussian noise, and were first used by Rudin, Osher and Fatemi [18] in 1992. The denoising model using a TV regularization together with a L^2 data term in image space is therefore often referred to as the ROF model. It is defined as the following minimization problem:

$$\min_u \left\{ \int_{\Omega} |\nabla u| dx + \frac{\lambda}{2} \int_{\Omega} (u - f)^2 dx \right\}, \quad (6.1)$$

where f is the original, corrupted image data. In the original work [18], the corruption is due to Gaussian noise, while in our case, it comes from streaking artifacts due to subsampling. The minimizer u is the reconstructed image, and Ω is the image domain. The regularization parameter λ controls the balance between artifact removal – minimizing the TV penalty – and faithfulness to the original image – minimizing the data fidelity term, – and so the proper choice of this parameter is a major challenge in any regularization based reconstruction method. The L^2 norm of the data fidelity term makes the removal of structures contrast dependent: Low contrast regions are removed, but strong contrast regions of the same size are kept. While this is desirable for high-contrast data such as CE-MR angiography, it is not appropriate for other data sets with low contrast features. For such applications, it is possible to extend the proposed approach to include an L^1 data fidelity term, which is better suited due to its contrast invariance. The TV regularization has the advantage of removing noise while preserving sharp edges in the image. Therefore, vessels with their strong contrast-to-noise-ratio are preserved,

while undersampling artifacts are efficiently removed. The main difference to the reconstruction strategies that were presented in the previous chapters of this thesis is that a two step procedure is used here: First, a Fourier transform is applied to the MRI raw data, giving a reconstructed image containing aliasing artifacts. This image is then filtered through TV minimization. A detailed comparison of these two approaches is given in the section 6.5 of this chapter.

The minimization of the ROF model is a well studied problem. As the functional defined in (6.1) is convex, the unique global minimizer can be calculated. In the original formulation, this was done using explicit time marching [18]. Other methods employ a linearization of the Euler-Lagrange equation [103], [104]. Duality based methods have shown greatly improved performance and were, among others, proposed in [105], [106], [107] and [108]. Recently, very fast primal-dual (PDU) approaches were proposed by Zhu et al. in [109] and [110], although they were already used for saddle point problems by Popov in [111]. In [112], a Split Bregman algorithm is used for the minimization. Discrete methods using graph cuts also can be used to solve the ROF model [113]. As shown in [114], continuous methods have the advantage of their inherent parallelization potential, a low memory consumption and no discretization artifacts. Recently, continuous methods have become applicable for large 3D data sets by implementing them on the GPU [114]. It is shown in this work that by adapting the PDU approach from [109] to 3D and by implementing it on the GPU, even large volume data sets can be processed in a reasonable time.

To benefit from the TV constraint in the third dimension, the streaking artifacts must appear in a different pattern in adjacent kz -planes. This can be achieved easily with a modification of the sampling trajectory. Currently, most radial acquisition patterns use a so called “stack of stars” trajectory [115] with radial sampling in the xy -plane and Cartesian encoding or multi slice acquisition in the z -direction. This sampling pattern uses the same projection angles in all kz -planes, which creates streaking artifacts in the image volume which are two-dimensional (specifically, independent of z) and therefore difficult to eliminate by TV minimization (which is chosen precisely for the fact that it preserves jumps over two-dimensional sets, such as artery boundaries). On the other hand, if the projection angles of adjacent kz -planes are shifted by $\frac{\pi}{2k}$, where k is the number of projections (see Figure 6.1), the aliasing artifacts have a different, line-like, structure which is much more easily removed. This should be compared with the 2D situation, where point-like artifacts (like noise) are smoothed, while edges in the image are preserved. A similar trajectory was already described in the context of kt -BLAST [11], where the third dimension was time instead of the kz -direction. This effect is illustrated in Figure 6.2. A stack of stars acquisition with these modified angles now benefits from the TV filtering in z -direction, which improves the overall artifact reduction capability of the ROF model.

6.2.2 GPU Implementation

Computing hardware have shown a clear tendency toward more and more parallelization over the last years. While modern CPUs already use 4 cores, modern GPUs like the Nvidia GeForce GTX 280 (Nvidia, Santa Clara, CA) utilize 240 cores. It should be noted that CPUs offer more programming flexibility, and GPUs use SIMD (single instruction, multiple data) architectures that require data-parallel algorithms. Additionally, GPUs utilize pipelining principles

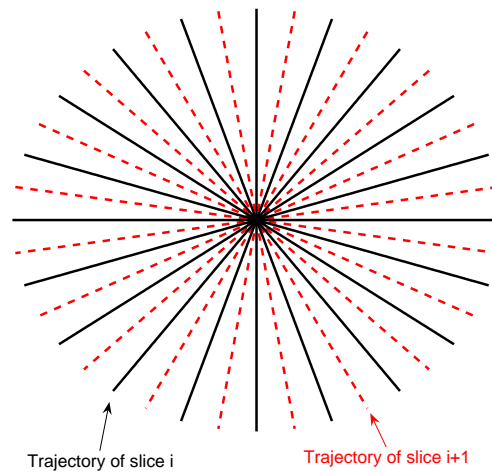


Figure 6.1: Stack of stars trajectory with shifted projection angles, 10 radial projections are displayed.

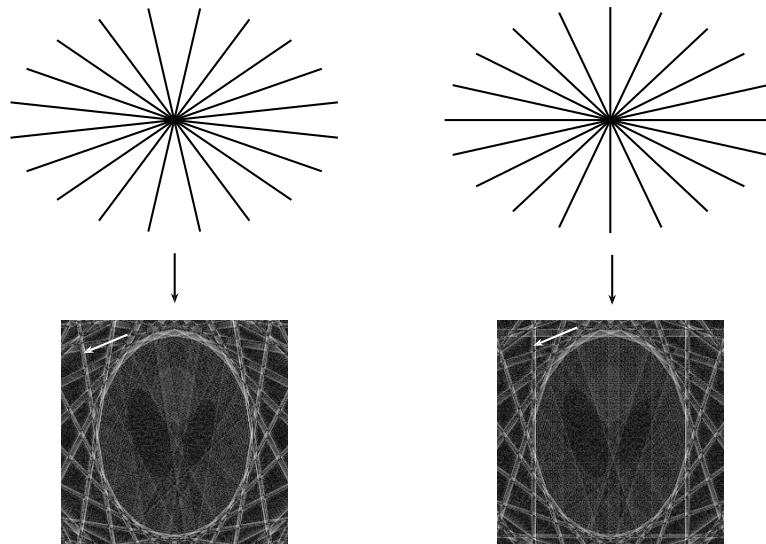


Figure 6.2: Illustration of the effect of shifted projection angles on the streaking artifacts in the reconstructed image for a numerical phantom. The phantom was sampled using 10 radial projections, and the projection angles were shifted by $\frac{\pi}{2k}$ between the two reconstructions. This leads to changes in the structure of the streaking artifacts which can easily be seen by the orientation of the specific streak that is highlighted by the arrows.

to optimize data throughput, the Nvidia GeForce GTX 280 offering a memory bandwidth of 141.7 GB/s. To utilize this high bandwidth, an efficient memory management is a crucial part of GPU implementations.

Our implementation was done using the CUDA [82] framework, which allows C-like programming on the GPU. Variational methods have an inherent parallelism, and are therefore perfectly suited for modern GPUs. For each voxel a single thread is created on the GPU, and synchronization is performed after each iteration. Special care was taken to maintain coalesced memory access during the whole computation. The GPU is organized in multiprocessors consisting of 8 single cores that have access to a fast local memory. This memory is organized in 16 banks which can be accessed simultaneously, and is as fast as registers when no bank conflicts occur. We make heavy use of this local memory by first loading a small patch from global memory, performing one iteration on this patch, and writing the patch back to global memory.

6.3 Materials and Methods

6.3.1 Phantom Measurements

The proposed radial stack of stars sequence with shifted projection angles was implemented on a clinical MR scanner (Siemens Magnetom TIM Trio, Erlangen, Germany).

An angiography phantom was constructed by inserting a plastic tube filled with with a Gd-DTPA (Magnevist, Schering AG) solute in a bottle of distilled water doped with MnCl_2 . The T_1 relaxation time of the tube is approximately 50 ms, which is comparable to a typical relaxation rate in the vessel system during the first passage of a contrast agent. The surrounding water in the bottle has a T_1 time of approximately 800 ms, comparable to the relaxation time of white matter in the brain. The phantom therefore represents the situation of a CE-MRA measurement of the brain vessels.

A 2D multi slice gradient echo sequence with the following sequence parameters, which ensured a strong T_1 contrast, was used to acquire the phantom images: $\text{TR} = 12$ ms, $\text{TE} = 5$ ms, $\text{FA} = 60^\circ$, matrix size $(x,y) = 256 \times 256$, 11 slices with a slice thickness of 2.5 mm, imaging field of view $\text{FOV} = 150 \text{ mm} \times 150 \text{ mm}$. All measurements were conducted at 3 T, using a transmit and receive birdcage resonator head coil. Measurements were performed with 64, 32 and 24 projections, resulting in undersampling factors of $R = 4$, $R = 8$ and $R \approx 10$ below the Nyquist limit in comparison to a fully sampled Cartesian data set. The corresponding MRI acquisition times are 8.4 s (64 projections), 4.2 s (32 projections) and 3.2 s (24 projections).

Raw data was exported from the scanner and offline image reconstruction was performed using a MATLAB (The MathWorks, Natick, MA) implementation of the non-uniform fast Fourier transform (NUFFT) [33]. Afterwards, these images were processed with the proposed 3D TV GPU method.

6.3.2 In vivo Angiography Measurements

The 3D TV GPU method was also evaluated with an in vivo data set, and the results were compared with reconstructions using alternative strategies. To assess image quality quantitatively,

a fully sampled contrast enhanced MR angiography (CE-MRA) data set of the carotid arteries was acquired on a clinical MR scanner at 3 T (Siemens Magnetom TIM Trio, Erlangen, Germany) using a 3D FLASH sequence. Sequence parameters were repetition time $TR = 3.74$ ms, echo time $TE = 1.48$ ms, flip angle $FA = 20^\circ$, matrix size $(x,y,z) = 448 \times 352 \times 40$, voxel size $(\Delta x, \Delta y, \Delta z) = 0.55 \text{ mm} \times 0.55 \text{ mm} \times 0.70 \text{ mm}$. The data set was exported and retrospectively subsampled in the xy -plane to simulate an accelerated acquisition. The fully sampled data set served as the gold standard reference for quantitative evaluations. Acquisitions with 80 and 40 projections, corresponding to undersampling factors of $R = 5.6$ and $R = 11.2$ in comparison to a fully sampled Cartesian data set, were simulated. These undersampling rates were chosen to illustrate situations when the TV reconstruction is able to eliminate almost all streaking artifacts (80 projections) and scenarios where the amount of undersampling is too high and residual artifacts remain after TV reconstruction (40 projections). For these sequence parameters, MRI acquisition times of the accelerated acquisitions would be 12.0 s (80 projections) and 6.0 s (40 projections). The MATLAB implementation of the non-uniform fast Fourier transform (NUFFT) [33] was again used during offline image reconstruction, and the images were then processed with the 3D TV filter.

To show the benefits of the proposed shifted spokes trajectory together with 3D TV, the results were compared to the application of the algorithm to a conventional not-shifted stack of stars trajectory and to 2D slice by slice TV filtering. Additionally, TV reconstruction with a k -space data fidelity term [1] was implemented using the nonlinear conjugate gradient algorithm from [16]. The regularization parameter λ was chosen according to visual inspection of the reconstruction quality. In each experiment, we started with very low regularization and gradually increased it until artifacts started to disappear. This iterative procedure was stopped when the last streaking artifact was removed. As this could not be achieved for the 40 projections in vivo data set for some methods, the increase of the regularization was stopped as soon as pronounced image features were lost. Approximately 5-10 runs, depending on the data set, were performed in that way for each method.

Image quality was quantified by means of the root-mean-square (RMS) difference to the fully sampled data set, normalized by the RMS intensities of the fully sampled images. RMS differences were evaluated slice by slice. Additionally, mean value and standard deviation over all 40 slices were calculated.

6.3.3 Reconstruction Time of the GPU Implementation

The proposed PDU 3D TV algorithm was implemented on the GPU. As the goal of this work was to evaluate the speedup that can be gained with the GPU implementation and not a comparison of reconstruction times for different algorithms, computation times were only evaluated for the proposed method. While the analysis of multiple methods is important in the case of image quality to show the benefits of 3D regularization, the most important test to evaluate speedup is a comparison to a fast C++ implementation of the same primal-dual algorithm on the CPU. Experiments were performed on an Intel Core 2 Duo 6700, while the GPU implementation was tested on an Nvidia GeForce GTX 280 using CUDA 2.0. All CPU times are reported for computations on a single core, in order to allow accurate timing and to disregard any scheduling

overhead. Of course, an implementation on multi-core architectures would be parallelized in practice (e.g., using OpenMP), yielding a higher performance corresponding to the number of cores.

6.4 Results

Figure 6.3 compares the results of conventional NUFFT reconstructions and the proposed TV method for the phantom experiments. It is not surprising that the conventional NUFFT reconstructions suffer from characteristic streaking artifacts which become increasingly worse as the number of projections is reduced. Artifacts are efficiently reduced by application of the TV filter. Additionally, the scans of the phantom are significantly deteriorated by noise, which in the TV reconstructions is also reduced due to its inherent noise cancellation properties. The final regularization parameters were $\lambda_{64proj} = 10$, $\lambda_{32proj} = 7$ and $\lambda_{24proj} = 5$. Here, smaller parameters amount to stronger regularization (i.e., the influence of the data fidelity term is reduced).

Figures 6.4 and 6.5 shows the reconstruction results of all tested methods for the downsampled angiography data set with 80 and 40 projections. Similar to the phantom experiments, conventional NUFFT reconstructions show streaking artifacts. While all TV methods reduce artifacts, only the 3D TV method with shifted projections is nearly artifact free for the 80 projections data set. In contrast, residual artifacts can be seen in all results of the 40 projections data set, but best image quality is again achieved with the 3D TV method with shifted projections. The final regularization parameters were $\lambda_{80proj} = 0.03$ and $\lambda_{40proj} = 0.08$ for 2D ROF TV, $\lambda_{80proj} = 0.35$ and $\lambda_{40proj} = 0.45$ for the implementation with a k -space data fidelity term, $\lambda_{80proj} = 15$ and $\lambda_{40proj} = 10$ for 3D TV with conventional and shifted radial sampling. It must be pointed out that these parameters cannot be compared directly between the methods due to the different formulation. Particularly, for the 3D methods, smaller parameters amount to stronger regularization as noted. On the other hand, the parameter λ in the 2D implementations corresponds to $\frac{1}{\lambda}$ in the ROF formulation, so that larger values of λ indicate higher regularization. Additionally, the relation between L^2 and L^1 norms is different in 2D and 3D, and so the parameter value for a given balance changes with dimension.

The results of the quantitative analysis of image quality for all methods are displayed in Table 6.1. In the case of 80 projections, all TV reconstruction methods show comparable RMS differences which are significantly lower than for the conventional NUFFT reconstruction. This is also true for the 40 projections data set, but both conventional 3D TV and especially 3D TV with shifted projections show significantly lower RMS differences than the other methods.

A compilation of computation times of 3D PDU TV for all tested data sets can be found in Table 6.2. With the GPU implementation, a computation speed of 718 iterations per second for the phantom data set and 129 iterations per second for the in vivo data set was achieved. In comparison, the computation speed of the CPU implementation was 3.78 iterations per second for the phantom data set and 0.46 iterations per second for the in vivo data set. This corresponds to speedup factors of 190 (phantom data) and 280 (in vivo data) with the GPU.

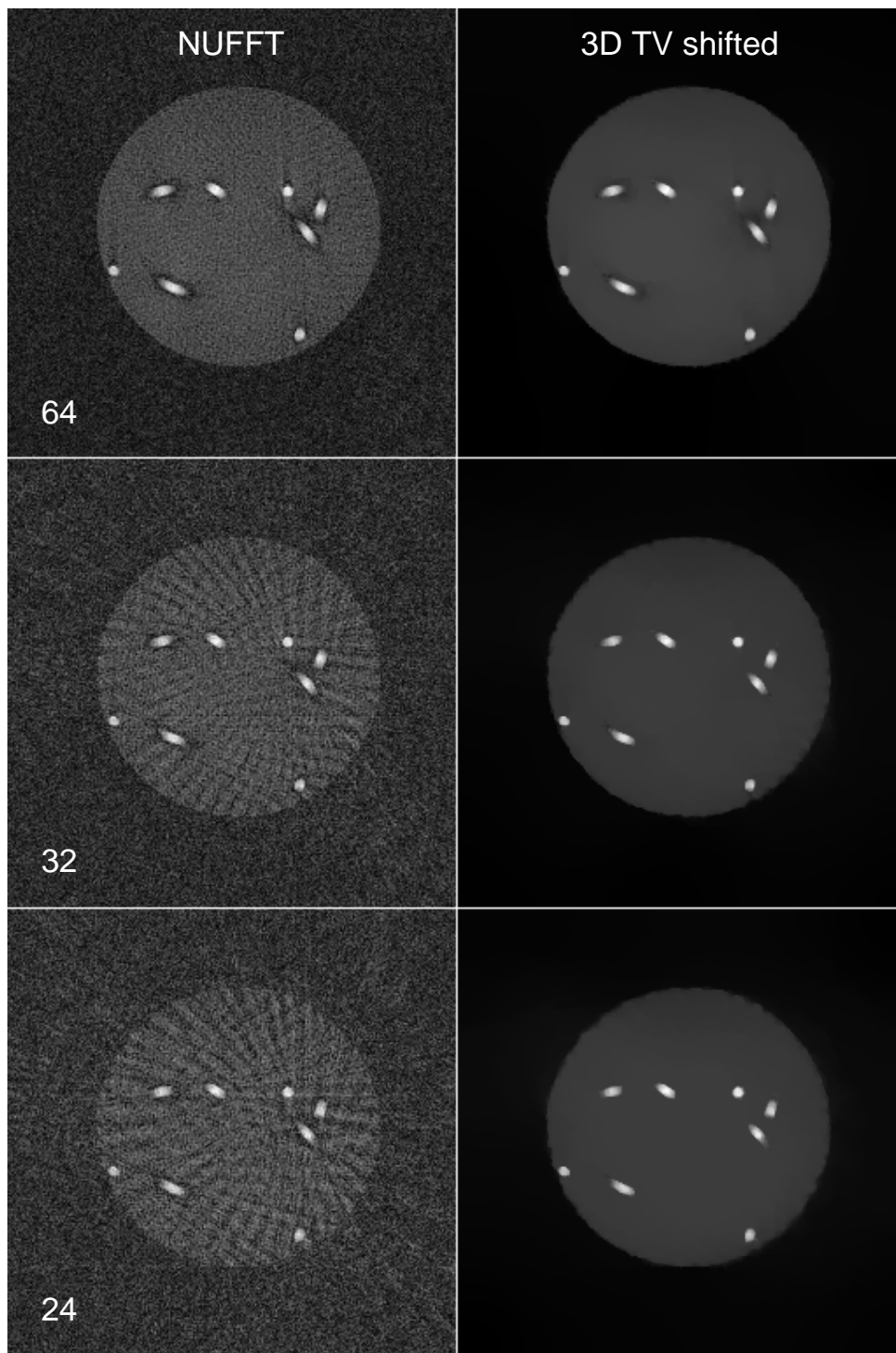


Figure 6.3: A single slice from the data set of the phantom measurements using 64 (top row, $\lambda = 10$), 32 (middle row, $\lambda = 7$) and 24 (bottom row, $\lambda = 5$) shifted projections. Conventional NUFFT reconstruction (left) and reconstruction with the proposed 3D TV method.

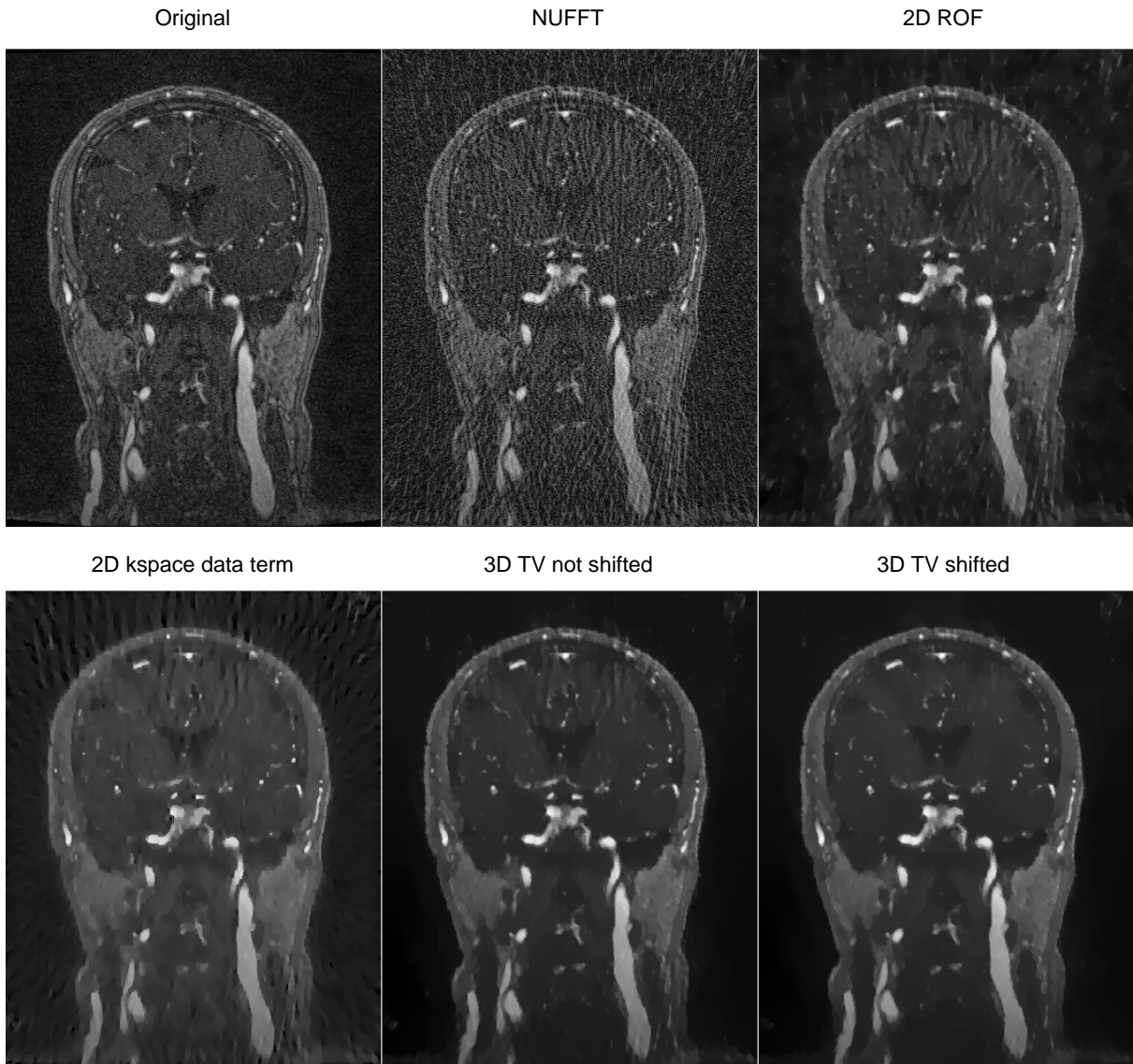


Figure 6.4: A single slice from the angiography data set with 80 projections ($\lambda_{2DROF} = 0.03$, $\lambda_{2Dk_{space}} = 0.35$, $\lambda_{3D} = 15$). Shown are original, fully sampled data set, conventional NUFFT reconstruction with zero filling, 2D slice by slice ROF TV filtering, TV reconstruction with data fidelity term in k -space, proposed 3D TV filtering using a conventional stack of stars trajectory, proposed 3D TV filtering using the shifted stack of stars trajectory

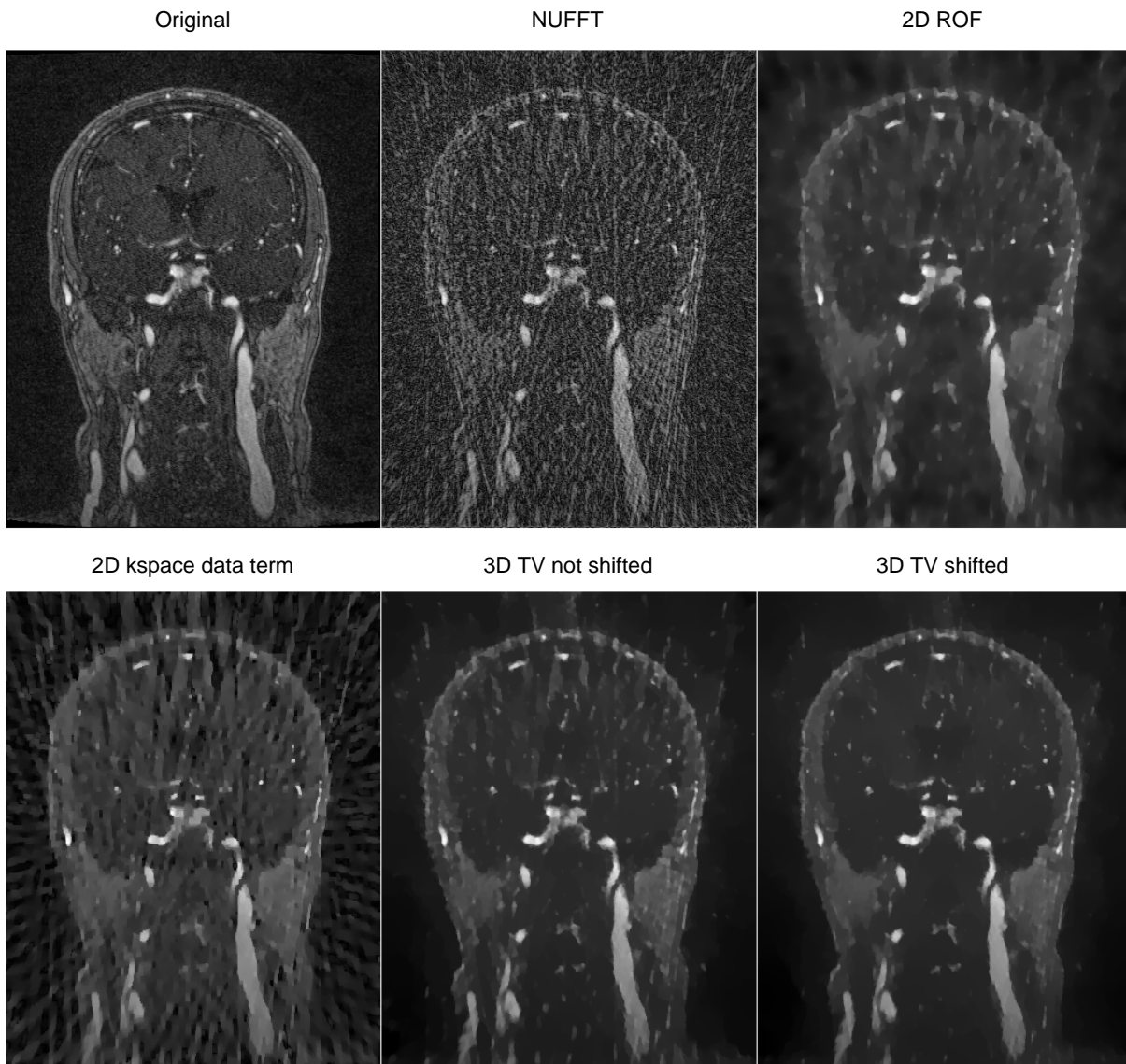


Figure 6.5: A single slice from the angiography data set with 40 projections ($\lambda_{2DROF} = 0.08$, $\lambda_{2Dkspace} = 0.45$, $\lambda_{3D} = 10$). Shown are original, fully sampled data set, conventional NUFFT reconstruction with zero filling, 2D slice by slice ROF TV filtering, TV reconstruction with data fidelity term in k -space, proposed 3D TV filtering using a conventional stack of stars trajectory, proposed 3D TV filtering using the shifted stack of stars trajectory

Table 6.1: Quantitative evaluation of the following reconstruction methods for the in vivo angiography data: Conventional NUFFT reconstruction with zero filling, 2D slice by slice ROF TV filtering, TV reconstruction with data fidelity in k -space, proposed 3D TV filtering using a conventional stack of stars trajectory, proposed 3D TV filtering using the shifted stack of stars trajectory that is introduced in this chapter. Mean value and standard deviation of RMS differences (a.u.) to the fully sampled data set for 40 slices are displayed using the 80 and 40 projections subsampled data.

Data set	NUFFT	2D TV	2D k -space	3D TV	3D TV shift.
80 proj.	0.40 ± 0.03	0.25 ± 0.02	0.26 ± 0.02	0.26 ± 0.02	0.25 ± 0.02
40 proj.	0.64 ± 0.06	0.39 ± 0.03	0.35 ± 0.02	0.34 ± 0.01	0.31 ± 0.01

Table 6.2: Computation times of PDU 3D TV on the GPU for all tested data sets.

Data set	Size	Time (s)	Iterations
Phantom 64 projections	$256 \times 256 \times 11$	0.556	400
Phantom 32 projections	$256 \times 256 \times 11$	0.697	500
Phantom 24 projections	$256 \times 256 \times 11$	0.836	600
In vivo 80 projections	$448 \times 352 \times 40$	1.546	200
In vivo 40 projections	$448 \times 352 \times 40$	1.552	200

6.5 Discussion

Our reconstructions with 3D TV and the shifted spokes sampling pattern show excellent removal of undersampling artifacts even at high acceleration factors. Due to the nature of the ROF functional (6.1), vessels with their strong contrast are preserved because the L^2 norm in the data fidelity term makes the removal of structures contrast dependent. Current work is concerned with extending the proposed approach to L^1 data fidelity terms, which are contrast invariant and thus better suited to images with low contrast features. Of course it must be mentioned that the results from the experiments with the angiography phantom represent an optimal situation for our algorithm as the phantom only consists of piecewise constant areas. This explains why all artifacts could be eliminated even for an undersampling factor of $R \approx 10$, which was not possible for the in vivo angiography data set. Future work will be necessary to evaluate TV methods in clinical studies.

Visual inspection of the image quality for the in vivo data set showed that 3D TV, together with the shifted spokes acquisition, significantly improved removal of streaking artifacts for both subsampling factors considered. Quantitative analysis also resulted in significantly lower RMS differences for the 40 projections data set, while RMS differences were similar for all TV-based methods in the case of 80 projections. However, the images clearly show different levels of artifact corruption. As mentioned in section 2.10, RMS difference cannot be considered

an optimal metric to describe image quality of MR images. However, due to the lack of a better quality metric, it is usually used in the literature and hence is included here to facilitate comparison with other works.

As already mentioned in section 6.2, the biggest difference between this approach and the methods recently described in chapters 2 to 5 is that the data fidelity term in the ROF model is evaluated in image space. In particular, equation 6.1 can be considered a special case of the more general formulation in equation 2.39 (section 2.9), where the forward operator is the identity matrix. As a consequence, the computation times of the two methods cannot be compared directly. While the image space based approach has the advantage of much lower computational complexity as the time consuming regridding step (section 2.6) does not have to be performed in each iteration, it must be noted that it limits the algorithm to applications such as angiography where the structures of interest have a high contrast-to-noise-ratio. On the other hand, angiography is an application which benefits significantly from the possibility of real-time imaging. For the in vivo angiography data set that was investigated in this chapter, no improvement in image quality was observed with a data fidelity term in k -space over conventional 2D ROF TV. It is also important to note that the two different approaches can be used in completely different situations. Image reconstruction is performed immediately after data acquisition, and MR-rawdata from the individual coil elements has to be available. On the other hand, the filtering approach is a postprocessing method. Of course it can also be integrated directly in the image reconstruction chain, but it can also be separated completely from data acquisition. MR image data is archived in the DICOM (Digital Imaging and Communications in Medicine) [116] standard, and with postprocessing, it is of course possible to enhance DICOM images that were obtained in a study that was performed in the past. In contrast, rawdata is usually not archived in a clinical setting, and if the use of an alternative reconstruction strategy is not planned already data acquisition, it can never be reconstructed again.

One important point concerning the comparison of different reconstruction strategies in this chapter is that the regularization parameter was chosen based on visual inspection of the image quality. This was performed individually for each different method to compare best-case results for each method. In the absence of robust and objective metrics for medical image quality which could be used as a basis for automatic regularization parameter choice rules, visual inspection by medical experts is still the most sensible criterion. It is important to note that for our GPU-based method, this becomes a practicable approach, since this step can be performed with a tool which allows interactive adjustment of the parameter and continuously displays the effect on the image quality. This means that regularization can be adjusted similar to the way windowing is performed at the moment. In this way, selection of an optimal parameter could be done in less than 20 seconds for the in vivo data set. In comparison, each run of the CPU implementation takes approximately 7 minutes, which is clearly not suitable for practical use. Of course, while visual inspection was our method of choice for this work, the GPU speedup can similarly be exploited in other parameter choice strategies that require multiple runs of the same optimization problem, such as heuristics of L-curve type and discrepancy principles [83], [84]. Inadequate image evaluation metrics are a major problem in automatic parameter selection strategies. It can be seen in Figures 6.4, 6.5 and Table 6.1 that even in cases where RMS differences are very

close to each other (e.g. between 2D ROF and 3D TV with shifted trajectories in the case of 80 projections, where the scores are in fact identical), visual inspection shows significant differences in terms of artifact suppression. Therefore an automatic parameter selection criterion based on RMS differences will in general not deliver optimal results. This means that the design of objective image perception metrics is one of the most important future tasks in the development of reliable automatic determination of regularization weights.

Finally, while 3D regularization was studied in this work, undersampling was only applied in the xy plane. Goals of future work will include the application to data sets where additional acceleration is included in the z-direction or for full 3D projection acquisition strategies like VIPR [29] where the aliasing pattern becomes more complicated.

On current graphics hardware with 1 GB of memory, data sets of a maximum size of $512 \times 512 \times 204$ can be calculated at once, which is sufficient for typical MRI data sets. For bigger data sets, Nvidia Tesla cards could be used or computation could be split up on multiple GPUs.

With computation times of approximately 1.5s for a $448 \times 352 \times 40$ data set, the GPU implementation allows TV filtering that is faster than the corresponding data acquisition times (12s and 6s for 80 and 40 projections, respectively), even in the case that multiple runs have to be performed to tune the regularization parameter. Therefore, the application of TV based artifact removal is no longer the time limiting step in the imaging chain. The goal of future work is to connect dedicated GPU computation hardware directly to the MR scanner, as was already described in the context of parallel imaging [117]. This will allow interactive TV artifact elimination already during data acquisition.

6.6 Conclusions

The results from this work show that the extension of TV filtering to 3D in combination with the proposed shifted stack of stars sampling trajectory leads to pronounced improvements in image quality for CE-MRA data. However, it must be noted that it cannot be expected that these results will generalize for arbitrary types of scans. With GPU implementations, TV computation times can be accelerated significantly and even allow interactive elimination of the regularization parameter for 3D TV. We believe that this can pave the way for TV based regularization strategies, currently promising research topics, to become powerful tools in daily clinical practice.

Chapter 7

Summary and Future Work

7.1 Summary

This thesis deals with the challenges that arise in the context of image reconstruction of accelerated measurements. Established strategies from the literature, some of them (like SENSE and GRAPPA) already used successfully in daily clinical practice, are summarized in chapter 2. Afterwards, the more recent concept of iterative image reconstruction, especially in combination with nonlinear L1 based regularization terms is introduced. Chapters 3 to 6 then describe the main contributions of this work. In a summarized form, these are:

- While image reconstruction from randomly sampled data has been a hot research topic in the last years, little work was done to address the problem of designing pseudo-random sampling patterns. An approach is presented that uses training data to estimate the power distribution in k -space, which then leads to the design of tailored sampling patterns for specific anatomic regions.
- The introduction of a new image model (TGV) that can be used as a regularizer for iterative image reconstruction of undersampled data. It is demonstrated in simulations and with in-vivo measurements that this approach efficiently removes undersampling artifacts, eliminates the well known problem of staircasing and preserves fine details and sharp edges in the reconstructed images.
- The successful concept of modelling image reconstruction as a nonlinear inversion problem is extended to a general framework which allows the integration of variational constraints. In combination with sampling trajectories that lead to incoherent undersampling artifacts like radial or pseudo-random sampling, this approach leads to a pronounced improvement of image quality when compared to methods that are currently described in the literature. The result is a flexible framework for image reconstruction that can easily be extended to include new image models.
- The use of parallel implementations of the proposed iterative methods on graphics hardware. This approach, which allows a significant reduction of computation time, is an important step for the transition of algorithms from the research lab to application in daily clinical routine.

7.2 Future Work

Based on the results of this work, there are a number of interesting points that should be the target of future research, and will be investigated in the second funding period of the SFB.

The general framework introduced in chapter 5 is very well suited to introduce additional a-priori information about the measured data set, which can serve as an additional constraint during the reconstruction. One very interesting idea is the extension of the method to quantitative imaging. Current approaches use a two step procedure where image reconstruction is performed prior to a post-processing fitting procedure. The proposed nonlinear inversion framework allows to include the parameter estimation step directly in the image reconstruction process. Biophysical models of the MR signal, e.g. exponential functions in the case of relaxation terms, can be directly integrated as additional constraints in the reconstruction process. First results of related ideas were recently published for iterative image reconstruction from radial data with T2 mapping [99] and compressed sensing with T1 and T2 mapping [100].

A similar expansion can be performed by integrating the correction of artifacts in the image reconstruction process. This task can also be integrated in the framework of nonlinear inversion similar to the problem of joint parameter estimation and image reconstruction. It has recently been demonstrated that the effect of motion on the k-space representation of the measured object [118,119] can be utilized for direct correction of motion related artifacts. With information about object motion integrated into the image reconstruction pipeline [120,121] it is also possible to correct for complex influences resulting from breathing and cardiac motion. This leads to coupled inverse problems, as image reconstruction and minimization of the motion effect have to be solved simultaneously. However, current approaches still need additional information to calibrate the motion model, like optical tracking, recording of the ECG, or the use of navigator scans and respiratory bellows. This prolongs MR scan time, reduces patient comfort and is challenging in terms of instrumentation, as all additional devices must operate in the environment of the MR-scanner. Therefore a long term goal is the vision of image reconstruction of undersampled data, including joint estimation of the coil sensitivities, calculation of quantitative parameters and elimination of artifacts, without the need of additional inputs other than the undersampled data and without any additional postprocessing steps.

TGV constrained reconstruction was first described in this work. It is expected that this approach can be used successfully to improve imaging speed and reconstruction quality in many different applications. TGV was already applied successfully to contrast enhanced MR-angiography data, as demonstrated during the ISMRM 2010 image reconstruction challenge. This is a particularly interesting application, especially in combination with state of the art pulse sequences designed for real-time imaging [96], because there is always a trade-off between spatial and temporal resolution. However, the application of TGV to CE-MRA has yet to be validated in clinical studies. An exciting goal that is worth pursuing is on-line monitoring of the distribution of contrast agent in the vessel system, with high spatial resolution, without the use of ECG gating and during free breathing. Another interesting extension of TGV is the application to diffusion tensor imaging (DTI). As the TGV definition is based on tensor functions, application of TGV regularization to the reconstruction of the diffusion tensor in DTI is a natural expansion.

While parallel implementations on graphics hardware were investigated in this thesis and significant improvements in terms of computation time have been achieved, this work is far from complete. The new possibilities of accelerated imaging like real-time imaging or imaging with much higher temporal and spatial resolution, together with the constant increase of receiver channels of phased array coils, leads to a dramatic increase of data that is generated during a measurement. The amount of acquired rawdata can easily exceed a few gigabytes. This leads to new challenges in terms of data transfer and memory management, especially for the use of GPUs, where available memory is limited.

Finally, while nonlinear methods for image reconstruction have shown to deliver excellent results, exhaustive validation is still an open topic. The robustness of these strategies for a wide range of applications has yet to be assessed in clinical studies.

Appendix A

Appendix: Numerical Algorithms

A.1 Algorithms for TGV

Both the denoising problem (4.3) and the undersampling reconstruction problem (4.5) constitute non-smooth convex optimization problems for which several numerical algorithms are available. In order to implement any numerical algorithm on a digital computer, we have to consider the discrete setting of the proposed reconstruction method (4.5). For discretization, we use a two dimensional regular Cartesian grid of size $M \times N$ and mesh size $h > 0$. For more information on the discrete setting we refer to [80]. From now on we will use the superscript h to indicate the discrete setting. The differential operators $\text{div}^h, \mathcal{E}^h, \nabla^h$ are approximated using first order finite differences. These operators are chosen adjoint to each other, i.e.

$$(\text{div}_2^h)^* = -\mathcal{E}^h, \quad (\text{div}_1^h)^* = -\nabla^h.$$

With $U^h = \mathbf{C}^{MN}$, the discrete version of the denoising problem (4.3) is given by

$$\min_{u^h \in U^h} \frac{1}{2} \|u^h - f^h\|_2^2 + \text{TGV}_\alpha^2(u^h), \quad (\text{A.1})$$

where $f^h \in U^h$ is the noisy input data and TGV_α^2 the discrete total generalized variation according to (4.2) using the corresponding discrete divergence operators. Unfortunately, this formulation involves a rather complicated convex set which is hard to deal with in numerical algorithms. It is therefore favorable to employ the alternative formulation (4.2). Doing so, problem (A.1) becomes

$$\min_{u^h \in U^h, v^h \in V^h} \frac{1}{2} \|u^h - f^h\|_2^2 + \alpha_1 \|\nabla^h u^h - v^h\|_1 + \alpha_0 \|\mathcal{E}^h(v^h)\|_1 \quad (\text{A.2})$$

where $V^h = \mathbf{C}^{2MN}$. Note that in this formulation, only first order differential operators are involved.

As recent trends in convex optimization [122,123] indicate and as they turn out to be suitable for our purposes, it is sensible to use first order algorithms since they are easy to implement, have a low memory print and can be efficiently parallelized. Furthermore, these methods come along with global worst case convergence rates. This allows to estimate the required number of iterations which are needed to reach a certain accuracy. Here, we employ the first-order primal dual algorithm of [98].

A.1.1 TGV denoising

The primal-dual algorithm we employed for solving the discretization of the TGV-constrained denoising problem (A.1) bases on the formulation of (A.2) as a convex-concave saddle-point problem which is derived by duality principles:

$$\min_{u^h \in U^h, v^h \in V^h} \max_{p^h \in P^h, q^h \in Q^h} \frac{1}{2\lambda} \|u^h - f^h\|_2^2 + \langle \nabla^h u^h - v^h, p \rangle + \langle \mathcal{E}^h(v^h), q \rangle, \quad (\text{A.3})$$

where p^h, q^h are the dual variables. The sets associated with these variables are given by

$$P^h = \{p^h \in \mathbf{C}^{2MN} \mid \|p^h\|_\infty \leq \alpha_1\}, \quad Q^h = \{q^h \in \mathbf{C}^{3MN} \mid \|q^h\|_\infty \leq \alpha_0\}.$$

We denote by $\text{proj}_{P^h}(\tilde{p}^h)$ and $\text{proj}_{Q^h}(\tilde{q}^h)$ the Euclidean projectors onto the convex sets P^h and Q^h . The projections can be easily computed by pointwise operations

$$\text{proj}_{P^h}(\tilde{p}^h) = \frac{\tilde{p}^h}{\max\left(1, \frac{|\tilde{p}^h|}{\alpha_1}\right)}, \quad \text{proj}_{Q^h}(\tilde{q}^h) = \frac{\tilde{q}^h}{\max\left(1, \frac{|\tilde{q}^h|}{\alpha_0}\right)}.$$

We further denote by $\text{prox}_1^\tau(\tilde{u}^h)$ the proximal map

$$\text{prox}_1^\tau(\tilde{u}^h) = \underset{u^h \in U^h}{\text{argmin}} \frac{\|u^h - \tilde{u}^h\|_2^2}{2\tau} + \frac{\|u^h - f^h\|_2^2}{2\lambda}.$$

which can easily identified as the pointwise operation

$$\text{prox}_1^\tau(\tilde{u}^h) = \frac{\lambda \tilde{u}^h + \tau f^h}{\lambda + \tau}.$$

The primal-dual algorithm for the denoising problem (A.1) reads as follows:

Algorithm 1 (Primal-dual method for TGV denoising)

- 1: **function** TGV_DENOISE(f^h)
- 2: $u^h, \bar{u}^h \leftarrow f^h, v^h, \bar{v}^h \leftarrow 0, p^h \leftarrow 0, q^h \leftarrow 0$, choose $\tau, \sigma > 0$.
- 3: **repeat**
- 4: $p^h \leftarrow \text{proj}_{P^h}(p^h + \sigma(\nabla^h \bar{u}^h - \bar{v}^h))$
- 5: $q^h \leftarrow \text{proj}_{Q^h}(q^h + \sigma \mathcal{E}^h \bar{v}^h)$
- 6: $u_{\text{old}}^h \leftarrow u^h$
- 7: $u^h \leftarrow \text{prox}_1^\tau(u^h + \tau \text{div}_1^h p^h)$
- 8: $\bar{u}^h \leftarrow 2u^h - u_{\text{old}}^h$
- 9: $v_{\text{old}}^h \leftarrow v^h$
- 10: $v^h \leftarrow v^h + \tau(p^h + \text{div}_2^h q^h)$
- 11: $\bar{v}^h \leftarrow 2v^h - v_{\text{old}}^h$
- 12: **until** convergence of u^h
- 13: **return** u^h
- 14: **end function**

Note that iterations are very simple and can therefore be efficiently implemented on parallel hardware such as graphics processing units. The algorithm is known to converge for step-sizes $\sigma\tau \leq 2h^2/(16 + h^2 + \sqrt{32h^2 + h^4})$, in particular for mesh-size $h = 1$, the choice $\sigma = \tau = 1/\sqrt{12}$ leads to convergence, see [98] for details.

A.1.2 TGV undersampling reconstruction

A discrete version of the reconstruction problem (4.5) can be derived as follows: Let $R^h = \mathbf{C}^{QP}$ represent the vector space associated with Q k -space measurements for P coils and denote by $K^h : U^h \rightarrow R^h$ and $(K^h)^*$ the linear operators which realize the NUFFT and its adjoint on the discrete data, respectively. We assume that K^h is normalized such that $\|K^h\| \leq 1$. Furthermore, denote by g^h the measured discrete radial sampling data. The continuous problem (4.5) then becomes

$$\min_{u^h \in U^h} \frac{1}{2\lambda} \|K^h u^h - g^h\|_2^2 + \text{TGV}_\alpha^2(u^h). \quad (\text{A.4})$$

The main difference in (A.4) to the denoising problem (A.1) is that the linear operator K^h is involved in the data fitting term. However, the method introduced in [98] can be easily adapted to this setting by introducing an additional dual variable. With a straightforward adaptation of Algorithm 1, however, one needs to compute the proximal map with respect to the data fitting term. Such an approach involves the solution of a linear system of equations which is quite costly. In order to circumvent this, we also dualize with respect to the data fitting term. The resulting convex-concave saddle-point problem is obtained as

$$\min_{u^h \in U^h, v^h \in V^h} \max_{p^h \in P^h, q^h \in Q^h, r^h \in R^h} \left\langle \nabla^h u^h - v^h, p^h \right\rangle + \left\langle \mathcal{E}^h(v^h), q^h \right\rangle + \left\langle K^h u^h - g^h, r^h \right\rangle - \frac{\lambda}{2} \|r^h\|_2^2, \quad (\text{A.5})$$

where $r^h \in R^h$ is the dual variable with respect to the data fitting term. Further, let $\text{prox}_2^\sigma(\tilde{r}^h)$ be the proximal map

$$\text{prox}_2^\sigma(\tilde{r}^h) = \underset{r^h \in R^h}{\text{argmin}} \frac{\|r^h - \tilde{r}^h\|_2^2}{2\sigma} + \frac{\lambda}{2} \|r^h\|_2^2 \quad \Leftrightarrow \quad \text{prox}_2^\sigma(\tilde{r}^h) = \frac{\tilde{r}^h}{1 + \sigma\lambda}.$$

The primal-dual algorithm for the reconstruction problem (4.5) is as follows:

Algorithm 2 (PD method for TGV undersampling reconstruction)

- 1: **function** TGVRECONSTRUCT(g^h)
- 2: $u^h, \bar{u}^h \leftarrow 0, v^h, \bar{v}^h \leftarrow 0, p^h \leftarrow 0, q^h \leftarrow 0, r^h \leftarrow 0$, choose $\tau, \sigma > 0$.
- 3: **repeat**
- 4: $p^h \leftarrow \text{proj}_{P^h}(p^h + \sigma \nabla^h(\bar{u}^h - \bar{v}^h))$
- 5: $q^h \leftarrow \text{proj}_{Q^h}(q^h + \sigma \mathcal{E}^h \bar{v}^h)$
- 6: $r^h \leftarrow \text{prox}_2^\sigma(r^h + \sigma(K^h \bar{u}^h - g^h))$
- 7: $u_{\text{old}}^h \leftarrow u^h$
- 8: $u^h \leftarrow u^h + \tau(\text{div}_1^h p^h - (K^h)^* r^h)$
- 9: $\bar{u}^h \leftarrow 2u^h - u_{\text{old}}^h$
- 10: $v_{\text{old}}^h \leftarrow v^h$
- 11: $v^h \leftarrow v^h + \tau(p^h + \text{div}_2^h q^h)$
- 12: $\bar{v}^h \leftarrow 2v^h - v_{\text{old}}^h$
- 13: **until** convergence of u^h
- 14: **return** u^h
- 15: **end function**

Again, this algorithm is convergent provided that $\sigma\tau < h^2/(h^2 + \sqrt{8}h + 8)$, in particular for mesh-size $h = 1$, the choice $\sigma = \tau = 1/\sqrt{12}$ is sufficient.

A.2 Algorithms for IRGN T(G)V

A.2.1 Solution of the IRGN-TV sub-problem

To calculate the solution of (5.2), we make use of the dual characterization of the TV semi norm:

$$\beta \int |\nabla u|_2 dx = \sup_{p \in C_\beta} \langle u, -\text{div}p \rangle, \quad (\text{A.6})$$

where $p = (p_1, p_2)^T$, $\text{div}p = \partial_x p_1 + \partial_y p_2$ with appropriate boundary conditions and

$$C_\beta = \{p \in L^2(\Omega; \mathbb{C}^2) : \text{div}p \in L^2(\Omega; \mathbb{C}), |p(x)|_2 \leq \beta \text{ for almost all } x \in \Omega\}. \quad (\text{A.7})$$

The problem in (5.2) then becomes a non-smooth convex-concave saddle-point problem

$$\min_{\delta u, \delta c} \max_{p \in C_{\beta_k}} \frac{1}{2} \|F'(x^k)\delta x + F(x^k) - s\|^2 + \frac{\alpha_k}{2} \mathcal{W}(c^k + \delta c) + \langle u^k + \delta u, -\text{div}p \rangle, \quad (\text{A.8})$$

which can be solved efficiently using a projected primal-dual extra-gradient method [98, 124], given as Algorithm 3 in the appendix. Since this requires only application of $F'(x^k)$ and its adjoint $F'(x^k)^*$, the algorithm can be implemented efficiently on modern multi-core hardware such as graphics processing units (GPUs). Due to the bilinear structure of F , the action of $F'(x^k)$ and $F'(x^k)^*$ can be calculated explicitly in terms of the subsampling operator \mathcal{F}_S and its adjoint \mathcal{F}_S^* . The projection onto the convex set C_β can be calculated point wise by setting for all $x \in \Omega$

$$\text{proj}_\beta(q)(x) = \frac{q(x)}{\max(1, \beta^{-1}(|q(x)|_2)}. \quad (\text{A.9})$$

The algorithm of the IRGN-TV subproblem ((A.8)) reads as follows:

Algorithm 3 (Solution of the IRGN-TV sub-problem)

- 1: **function** TVSOLVE(u, c, g, α, β)
- 2: $\delta u, \bar{\delta}u, \delta c, \bar{\delta}c, p \leftarrow 0$, choose $\sigma, \tau > 0$
- 3: **repeat**
- 4: $p \leftarrow \text{proj}_\beta(p + \tau \nabla(u + \bar{\delta}u))$
- 5: $\delta u_{old} \leftarrow \delta u, \delta c_{old} \leftarrow \delta c$
- 6: $\delta u \leftarrow \delta u - \sigma(\sum_{i=1}^N c_i^* \cdot \mathcal{F}_s^*(\mathcal{F}_s(u \cdot \bar{\delta}c_i + c_i \cdot \bar{\delta}u) + F(u, c) - g) - \text{div}p)$
- 7: $\delta c \leftarrow \delta c - \sigma(u^* \cdot \mathcal{F}_s^*(\mathcal{F}_s(u \cdot \bar{\delta}c_i + c_i \cdot \bar{\delta}u) + F(u, c) - g) + \alpha W^*W(c_i + \bar{\delta}c_i))$
- 8: $\bar{\delta}u \leftarrow 2\delta u - \delta u_{old}$
- 9: $\bar{\delta}c \leftarrow 2\delta c - \delta c_{old}$
- 10: **until** convergence
- 11: **return** $\delta u, \delta c$
- 12: **end function**

A.2.2 Solution of the IRGN-TGV sub-problem

Using again the dual representation of the norms, the Gauss-Newton step ((5.2)) is equivalent to the saddle point problem

$$\min_{\delta u, \delta c, v} \max_{\substack{p \in C_{\beta_k}^1 \\ q \in C_{\beta_k}^2}} \frac{1}{2} \|F'(x^k)\delta x + F(x^k) - s\|^2 + \frac{\alpha_k}{2} \mathcal{W}(c^k + \delta c) + \langle \nabla u^k + \delta u - v, p \rangle + \langle \mathcal{E}v, q \rangle, \quad (\text{A.10})$$

where

$$C_{\beta}^2 = \left\{ q \in \mathcal{C}_c(\Omega, \mathcal{S}^{2 \times 2}) : (|q_{11}(x)|^2 + |q_{22}(x)|^2 + 2|q_{12}(x)|^2)^{1/2} \leq 2\beta \forall x \in \Omega \right\} \quad (\text{A.11})$$

and $\mathcal{S}^{2 \times 2}$ denotes the set of symmetric complex matrices. The corresponding extra-gradient method is given as Algorithm 4, where the projection proj_{β}^2 onto C_{β}^2 can again be computed point wise.

The algorithm of the IRGN-TGV subproblem ((A.10)) reads as follows:

Algorithm 4 (Solution of the IRGN-TGV sub-problem)

- 1: **function** TGV_{SOLVE}(u, c, g, α, β)
- 2: $\delta u, \bar{\delta}u, \delta c, \bar{\delta}c, v, \bar{v}, p, q \leftarrow 0$, choose $\sigma, \tau > 0$
- 3: **repeat**
- 4: $p \leftarrow \text{proj}_{\beta}(p + \tau(\nabla(u + \bar{\delta}u) - v))$
- 5: $q \leftarrow \text{proj}_{\beta}^2(q + \tau(\mathcal{E}v))$
- 6: $\delta u_{old} \leftarrow \delta u, \delta c_{old} \leftarrow \delta c, v_{old} \leftarrow v$
- 7: $\delta u \leftarrow \delta u - \sigma(\sum_{i=1}^N c_i^* \cdot \mathcal{F}_s^*(\mathcal{F}_s(u \cdot \bar{\delta}c_i + c_i \cdot \bar{\delta}u) + F(u, c) - g) - \text{div}p)$
- 8: $\delta c \leftarrow \delta c - \sigma(u^* \cdot \mathcal{F}_s^*(\mathcal{F}_s(u \cdot \bar{\delta}c_i + c_i \cdot \bar{\delta}u) + F(u, c) - g) + \alpha W^*W(c_i + \bar{\delta}c_i))$
- 9: $v \leftarrow v - \sigma(-p + \mathcal{E}^*q)$
- 10: $\bar{\delta}u \leftarrow 2\delta u - \delta u_{old}$
- 11: $\bar{\delta}c \leftarrow 2\delta c - \delta c_{old}$
- 12: $\bar{v} \leftarrow 2v - v_{old}$
- 13: **until** convergence
- 14: **return** $\delta u, \delta c$
- 15: **end function**

A.2.3 Parameter Choice

The parameters in Algorithm 3 were chosen according to the convergence theory for the projected extra-gradient scheme. The step lengths σ and τ were chosen such that $\sigma\tau L^2 < 1$ holds, where L is the Lipschitz constant of the gradient of the functional to be minimized. This constant depends on the subsampling strategy and the iterates u^k, c^k , but can be estimated using a few iterations of the power method to approximately compute the norms of the partial Fréchet derivatives of the linearized operator $F'(x)$. As the norm of the finite difference approximation of the divergence and gradient operators with mesh size 1 is $\sqrt{8}$, we set $\tau = \sigma = 1/\sqrt{8 + 2 \max(|\tilde{L}_u|, |\tilde{L}_c|)}$ in Algorithm 3, where \tilde{L}_u, \tilde{L}_c are the estimates from the power method. The step lengths in

Algorithm 4 were set to $\tau = \sigma = 1/\sqrt{12 + 2\max(|\tilde{L}_u|, |\tilde{L}_c|)}$ based on the norm of the linear operator involving the symmetrized derivative. The iteration was terminated after a fixed number of iterations, since the efficiency estimate for the extra-gradient method gives an upper bound on the required number of iterations to achieve a given accuracy. Since a high accuracy is not necessary during the initial Gauss-Newton iterations with large penalties, we started with $N_0 = 20$ iterations and set $N_k = 2N_{k+1}$. These choices were stable and yielded good results for all data sets.

Bibliography

- [1] Block KT, Uecker M, Frahm J. Undersampled radial MRI with multiple coils. Iterative image reconstruction using a total variation constraint. *Magn Reson Med* 2007;57(6):1086–1098.
- [2] Sodickson DK, Manning WJ. Simultaneous acquisition of spatial harmonics (SMASH): fast imaging with radiofrequency coil arrays. *Magn Reson Med* 1997;38(4):591–603.
- [3] Pruessmann KP, Weiger M, Scheidegger MB, Boesiger P. SENSE: sensitivity encoding for fast MRI. *Magn Reson Med* 1999;42(5):952–962.
- [4] Griswold MA, Jakob PM, Heidemann RM, Nittka M, Jellus V, Wang J, Kiefer B, Haase A. Generalized autocalibrating partially parallel acquisitions (GRAPPA). *Magn Reson Med* 2002;47(6):1202–1210.
- [5] Ying L, Sheng J. Joint image reconstruction and sensitivity estimation in SENSE (JSENSE). *Magn Reson Med* 2007;57(6):1196–1202.
- [6] Uecker M, Hohage T, Block KT, Frahm J. Image reconstruction by regularized nonlinear inversion—joint estimation of coil sensitivities and image content. *Magn Reson Med* 2008; 60(3):674–682.
- [7] Uecker M. Nonlinear Reconstruction Methods for Parallel Magnetic Resonance Imaging. Ph.D. thesis, Georg-August-Universitaet Goettingen, 2009.
- [8] van Vaals JJ, Brummer ME, Dixon WT, Tuithof HH, Engels H, Nelson RC, Gerety BM, Chezmar JL, den Boer JA. "Keyhole" method for accelerating imaging of contrast agent uptake. *J Magn Reson Imaging* 1993;3(4):671–675.
- [9] Hanson JM, Liang ZP, Magin RL, Duerk JL, Lauterbur PC. A comparison of RIGR and SVD dynamic imaging methods. *Magn Reson Med* 1997;38(1):161–167.
- [10] Tsao J, Boesiger P, Pruessmann KP. k-t BLAST and k-t SENSE: dynamic MRI with high frame rate exploiting spatiotemporal correlations. *Magn Reson Med* 2003;50(5):1031–1042.
- [11] Hansen MS, Baltus C, Tsao J, Kozerke S, Pruessmann KP, Eggers H. k-t BLAST reconstruction from non-Cartesian k-t space sampling. *Magn Reson Med* 2006;55(1):85–91.
- [12] Mistretta CA, Wieben O, Velikina J, Block W, Perry J, Wu Y, Johnson K, Wu Y. Highly constrained backprojection for time-resolved MRI. *Magn Reson Med* 2006;55(1):30–40.

- [13] Huang Y, Wright GA. Time-resolved MR angiography with limited projections. *Magn Reson Med* 2007;58(2):316–325.
- [14] Candes EJ, Romberg J, Tao T. Robust uncertainty principles: exact signal reconstruction from highly incomplete frequency information. *IEEE Transactions on Information Theory* 2006;52(2):489–509.
- [15] Donoho DL. Compressed sensing. *IEEE Transactions on Information Theory* 2006; 52(4):1289–1306.
- [16] Lustig M, Donoho D, Pauly JM. Sparse MRI: The application of compressed sensing for rapid MR imaging. *Magn Reson Med* 2007;58(6):1182–1195.
- [17] Lustig M. Sparse MRI. Ph.D. thesis, Stanford University, 2008.
- [18] Rudin LI, Osher S, Fatemi E. Nonlinear total variation based noise removal algorithms. *Phys D* 1992;60(1-4):259–268.
- [19] Block T. Advanced Methods for Radial Data Sampling in MRI. Ph.D. thesis, Georg-August-Universitaet Goettingen, 2008.
- [20] Lustig M, Pauly JM. SPIRiT: Iterative self-consistent parallel imaging reconstruction from arbitrary k-space. *Magn Reson Med* 2010;64(2):457–471.
- [21] Knoll F, Clason C, Diwoky C, Stollberger R. Adapted random sampling patterns for accelerated mri. *MAGMA* 2011;24(1):43–50.
- [22] Knoll F, Bredies K, Pock T, Stollberger R. Second order total generalized variation TGV for MRI. *Magn Reson Med* 2011;65(2):480–491.
- [23] Knoll F, Clason C, Bredies K, Uecker M, Stollberger R. Nonlinear parallel imaging with variational penalties. *Magn Reson Med* 2011;In Press.
- [24] Knoll F, Unger M, Diwoky C, Clason C, Pock T, Stollberger R. Fast reduction of under-sampling artifacts in radial MR angiography with 3D total variation on graphics hardware. *MAGMA* 2010;23(2):103–114.
- [25] Haacke ME, Brown RW, Thompson MR, Venkatesan R. *Magnetic Resonance Imaging: Physical Principles and Sequence Design*. John Wiley & Sons, 1999.
- [26] Bernstein MA, King KF, Zhou XJ. *Handbook of MRI Pulse Sequences*. Academic Press, 2004.
- [27] Liang ZP, Haacke EM. *Encyclopedia of Electrical and Electronics Engineering*, volume 2. John Wiley & Sons, 1999; 412–426.
- [28] Lauterbur PC. Image formation by induced local interactions: Examples employing nuclear magnetic resonance. *Nature* 1973;242:190–191.

- [29] Barger AV, Block WF, Toropov Y, Grist TM, Mistretta CA. Time-resolved contrast-enhanced imaging with isotropic resolution and broad coverage using an undersampled 3D projection trajectory. *Magn Reson Med* 2002;48(2):297–305.
- [30] Liang ZP, Lauterbur PC. *Principles of Magnetic Resonance Imaging: A Signal Processing Perspective*. Wiley-IEEE Press, 1999.
- [31] O’Sullivan JD. A fast sinc function gridding algorithm for fourier inversion in computer tomography. *IEEE Trans Med Imaging* 1985;4(4):200–207.
- [32] Rasche V, Proksa R, Sinkus R, Brnert P, Eggers H. Resampling of data between arbitrary grids using convolution interpolation. *IEEE Trans Med Imaging* 1999;18(5):385–392.
- [33] Fessler JA, Sutton BP. Nonuniform fast Fourier transforms using min-max interpolation. *IEEE Transactions on Signal Processing* 2003;51(2):560–574.
- [34] Beatty PJ, Nishimura DG, Pauly JM. Rapid gridding reconstruction with a minimal oversampling ratio. *IEEE Trans Med Imaging* 2005;24(6):799–808.
- [35] Jackson JI, Meyer CH, Nishimura DG, Macovski A. Selection of a convolution function for fourier inversion using gridding [computerised tomography application]. *IEEE Trans Med Imaging* 1991;10(3):473–478.
- [36] Kaiser JF. Nonrecursive digital filter design using the i_0 -sinh window function. In *In Proc. IEEE Int. Symp. on Circuits and Syst.* 1974; 20–23.
- [37] Aurenhammer F. Voronoi diagrams - a survey of a fundamental geometric data structure. *ACM Computing Surveys* 1991;23(3):345405.
- [38] Ramachandran GN, Lakshminarayanan AV. Three-dimensional reconstruction from radiographs and electron micrographs: application of convolutions instead of fourier transforms. *Proc Natl Acad Sci U S A* 1971;68(9):2236–2240.
- [39] Roemer PB, Edelstein WA, Hayes CE, Souza SP, Mueller OM. The NMR phased array. *Magn Reson Med* 1990;16(2):192–225.
- [40] Hutchinson M, Raff U. Fast MRI data acquisition using multiple detectors. *Magn Reson Med* 1988;6(1):87–91.
- [41] Lin FH, Wald LL, Ahlfors SP, Hmlinen MS, Kwong KK, Belliveau JW. Dynamic magnetic resonance inverse imaging of human brain function. *Magn Reson Med* 2006;56(4):787–802.
- [42] Bammer R, Schoenberg SO. Current concepts and advances in clinical parallel magnetic resonance imaging. *Top Magn Reson Imaging* 2004;15(3):129–158.
- [43] Blaimer M, Breuer F, Mueller M, Heidemann RM, Griswold MA, Jakob PM. SMASH, SENSE, PILS, GRAPPA: how to choose the optimal method. *Top Magn Reson Imaging* 2004;15(4):223–236.

- [44] Hoge WS, Brooks DH, Madore B, Kyriakos WE. A tour of accelerated parallel MR imaging from a linear systems perspective. *Concepts in Magnetic Resonance Part A* 2005; 27A:17–37.
- [45] Breuer FA. Development and Application of Efficient Strategies for Parallel Magnetic Resonance Imaging. Ph.D. thesis, Julius-Maximilians-Universitaet Wuerzburg, 2006.
- [46] Walsh DO, Gmitro AF, Marcellin MW. Adaptive reconstruction of phased array MR imagery. *Magn Reson Med* 2000;43(5):682–690.
- [47] Bydder M, Larkman DJ, Hajnal JV. Combination of signals from array coils using image-based estimation of coil sensitivity profiles. *Magn Reson Med* 2002;47(3):539–548.
- [48] Wiggins G, Potthast A, Triantafyllou C, Lin FH, Benner T, Wiggins C, Wald L. A 96-channel MRI system with 23- and 90-channel phase array head coils at 1.5 Tesla. In *Proceedings of the 13th Scientific Meeting and Exhibition of ISMRM, Miami Beach, FL*. 2005; 671.
- [49] Buehrer M, Pruessmann KP, Boesiger P, Kozerke S. Array compression for MRI with large coil arrays. *Magn Reson Med* 2007;57(6):1131–1139.
- [50] Weiger M, Pruessmann KP, Boesiger P. 2D SENSE for faster 3D MRI. *MAGMA* 2002; 14(1):10–19.
- [51] Blaimer M, Breuer FA, Mueller M, Seiberlich N, Ebel D, Heidemann RM, Griswold MA, Jakob PM. 2D-GRAPPA-operator for faster 3D parallel MRI. *Magn Reson Med* 2006; 56(6):1359–1364.
- [52] Wang J, Kluge T, Nittka M, Jellus V, Kuehn B, Kiefer B. Parallel acquisition techniques with modified SENSE reconstruction mSENSE. In *Proceedings of the First Wurzburg Workshop on Parallel Imaging*. 2001; 92.
- [53] Griswold MA, Breuer F, Blaimer M, Kannengiesser S, Heidemann RM, Mueller M, Nittka M, Jellus V, Kiefer B, Jakob PM. Autocalibrated coil sensitivity estimation for parallel imaging. *NMR Biomed* 2006;19(3):316–324.
- [54] Poon CS, Henkelman RM. Practical T2 quantitation for clinical applications. *J Magn Reson Imaging* 1992;2(5):541–553.
- [55] Pruessmann KP, Weiger M, Brnert P, Boesiger P. Advances in sensitivity encoding with arbitrary k-space trajectories. *Magn Reson Med* 2001;46(4):638–651.
- [56] Seiberlich N, Breuer FA, Blaimer M, Barkauskas K, Jakob PM, Griswold MA. Non-Cartesian data reconstruction using GRAPPA operator gridding (GROG). *Magn Reson Med* 2007;58(6):1257–1265.
- [57] Seiberlich N, Breuer F, Blaimer M, Jakob P, Griswold M. Self-calibrating GRAPPA operator gridding for radial and spiral trajectories. *Magn Reson Med* 2008;59(4):930–935.

- [58] Seiberlich N, Breuer F, Heidemann R, Blaimer M, Griswold M, Jakob P. Reconstruction of undersampled non-Cartesian data sets using pseudo-Cartesian GRAPPA in conjunction with GROG. *Magn Reson Med* 2008;59(5):1127–1137.
- [59] Seiberlich N, Breuer FA, Ehses P, Moriguchi H, Blaimer M, Jakob PM, Griswold MA. Using the GRAPPA operator and the generalized sampling theorem to reconstruct undersampled non-Cartesian data. *Magn Reson Med* 2009;61(3):705–715.
- [60] Kellman P, Epstein FH, McVeigh ER. Adaptive sensitivity encoding incorporating temporal filtering (tsense). *Magn Reson Med* 2001;45(5):846–852.
- [61] Breuer FA, Kellman P, Griswold MA, Jakob PM. Dynamic autocalibrated parallel imaging using temporal GRAPPA (TGRAPPA). *Magn Reson Med* 2005;53(4):981–985.
- [62] Huang F, Akao J, Vijayakumar S, Duensing GR, Limkeman M. k-t grappa: a k-space implementation for dynamic mri with high reduction factor. *Magn Reson Med* 2005;54(5):1172–1184.
- [63] Margosian P, Schmitt F, D DP. Faster MR imaging: imaging with half the data. *Health Care Instrum* 1986;1:195–197.
- [64] Liang ZP, Boada F, Constable R, Haacke E, Lauterbur P, Smith M. Constrained reconstruction methods in MR imaging. *Rev Magn Reson Med* 1992;4:67–185.
- [65] Gamper U, Boesiger P, Kozerke S. Compressed sensing in dynamic MRI. *Magn Reson Med* 2008;59(2):365–373.
- [66] Huo D, Xu D, Liang ZP, Wilson D. Application of perceptual difference model on regularization techniques of parallel MR imaging. *Magn Reson Imaging* 2006;24(2):123–132.
- [67] Miao J, Huo D, Wilson DL. Quantitative image quality evaluation of MR images using perceptual difference models. *Med Phys* 2008;35(6):2541–2553.
- [68] Vasanawala SS, Alley MT, Hargreaves BA, Barth RA, Pauly JM, Lustig M. Improved pediatric MR imaging with compressed sensing. *Radiology* 2010;256(2):607–616.
- [69] Glover GH, Noll DC. Consistent projection reconstruction (CPR) techniques for mri. *Magn Reson Med* 1993;29(3):345–351.
- [70] Lee JH, Hargreaves BA, Hu BS, Nishimura DG. Fast 3D imaging using variable-density spiral trajectories with applications to limb perfusion. *Magn Reson Med* 2003;50(6):1276–1285.
- [71] Marseille, de Beer R, Fuderer, Mehlkopf, van Ormondt D. Nonuniform phase-encode distributions for MRI scan time reduction. *J Magn Reson B* 1996;111(1):70–75.
- [72] Nayak KS, Nishimura DG. Randomized trajectories for reduced aliasing artifact. In *Proceedings of the Scientific Meeting and Exhibition of ISMRM, Sydney, Australia. 1998;*

- [73] Tsai CM, Nishimura DG. Reduced aliasing artifacts using variable-density k-space sampling trajectories. *Magn Reson Med* 2000;43(3):452–458.
- [74] Greiser A, von Kienlin M. Efficient k-space sampling by density-weighted phase-encoding. *Magn Reson Med* 2003;50(6):1266–1275.
- [75] Lustig M, Donoho DL, Santos JM, Pauly JM. Compressed sensing MRI. *IEEE Signal Processing Magazine* 2008;25(2):72–82.
- [76] Liu B, King K, Steckner M, Xie J, Sheng J, Ying L. Regularized sensitivity encoding (SENSE) reconstruction using Bregman iterations. *Magn Reson Med* 2009;61(1):145–152.
- [77] Wald MJ, Adluru G, Song HK, Wehrli FW. Accelerated high-resolution imaging of trabecular bone using total variation constrained reconstruction. In *Proceedings of the 17th Scientific Meeting and Exhibition of ISMRM, Honolulu, HI. 2009; .*
- [78] Block KT, Uecker M, Frahm J. Suppression of MRI truncation artifacts using total variation constrained data extrapolation. In *Proceedings of the 16th Scientific Meeting and Exhibition of ISMRM, Toronto, Canada. 2008; .*
- [79] Huang F, Chen Y, Duensing GR, Akao J, Rubin A, Saylor C. Application of partial differential equation-based inpainting on sensitivity maps. *Magn Reson Med* 2005;53(2):388–397.
- [80] Bredies K, Kunisch K, Pock T. Total generalized variation. *SIAM Journal on Imaging Sciences* 2010;3(3):492–526.
- [81] Merwa R, Reishofer G, Feiweier T, Kapp K, Ebner F, Stollberger R. Improved quantification of pharmacokinetic parameters at 3 tesla considering B1 inhomogeneities. In *Proceedings of the 17th Scientific Meeting and Exhibition of ISMRM, Honolulu, HI. 2009; 4363.*
- [82] NVIDIA. *NVIDIA CUDA Programming Guide 2.0*. NVIDIA Cooperation, 2008.
- [83] Engl HW, Hanke M, Neubauer A. *Regularization of inverse problems, volume 375 of Mathematics and its Applications*. Dordrecht: Kluwer Academic Publishers Group, 1996.
- [84] Morozov VA. On the solution of functional equations by the method of regularization. *Soviet Math Dokl* 1966;7:414–417.
- [85] Bauer F, Kannengiesser S. An alternative approach to the image reconstruction for parallel data acquisition in MRI. *Math Meth Appl Sci* 2007;30:1437–1451.
- [86] Uecker M, Karaus A, Frahm J. Inverse reconstruction method for segmented multishot diffusion-weighted MRI with multiple coils. *Magn Reson Med* 2009;62(5):1342–1348.
- [87] Knoll F, Clason C, Uecker M, Stollberger R. Improved reconstruction in non-Cartesian parallel imaging by regularized nonlinear inversion. In *Proceedings of the 17th Scientific Meeting and Exhibition of ISMRM, Honolulu, HI. 2009; .*

- [88] Uecker M, Zhang S, Frahm J. Nonlinear inverse reconstruction for real-time MRI of the human heart using undersampled radial FLASH. *Magn Reson Med* 2010;63(6):1456–1462.
- [89] Xiang QS. Accelerating MRI by skipped phase encoding and edge deghosting (SPEED). *Magn Reson Med* 2005;54(5):1112–1117.
- [90] Bakushinsky AB, Kokurin MY. Iterative methods for approximate solution of inverse problems, volume 577 of *Mathematics and Its Applications (New York)*. Dordrecht: Springer, 2004.
- [91] Blaschke B, Neubauer A, Scherzer O. On convergence rates for the iteratively regularized Gauss-Newton method. *IMA J Numer Anal* 1997;17(3):421–436.
- [92] Hohage T. Logarithmic convergence rates of the iteratively regularized Gauss-Newton method for an inverse potential and an inverse scattering problem. *Inverse Problems* 1997;13(5):1279–1299.
- [93] Frahm J, Haase A, Matthaei D. Rapid nmr imaging of dynamic processes using the flash technique. *Magn Reson Med* 1986;3(2):321–327.
- [94] Riederer SJ, Tasciyan T, Farzaneh F, Lee JN, Wright RC, Herfkens RJ. Mr fluoroscopy: technical feasibility. *Magn Reson Med* 1988;8(1):1–15.
- [95] Wright RC, Riederer SJ, Farzaneh F, Rossman PJ, Liu Y. Real-time mr fluoroscopic data acquisition and image reconstruction. *Magn Reson Med* 1989;12(3):407–415.
- [96] Zhang S, Block KT, Frahm J. Magnetic resonance imaging in real time: advances using radial FLASH. *J Magn Reson Imaging* 2010;31(1):101–109.
- [97] Uecker M, Zhang S, Voit D, Karaus A, Merboldt KD, Frahm J. Real-time MRI at a resolution of 20 ms. *NMR Biomed* 2010;23:986–994.
- [98] Chambolle A, Pock T. A first-order primal-dual algorithm for convex problems with applications to imaging. *Journal of Mathematical Imaging and Vision* 2010;40(1):120–145.
- [99] Block KT, Uecker M, Frahm J. Model-based iterative reconstruction for radial fast spin-echo MRI. *IEEE Trans Med Imaging* 2009;28(11):1759–1769.
- [100] Doneva M, Boernert P, Eggers H, Stehning C, Senegas J, Mertins A. Compressed sensing reconstruction for magnetic resonance parameter mapping. *Magn Reson Med* 2010;.
- [101] Hansen MS, Atkinson D, Sorensen TS. Cartesian SENSE and k-t SENSE reconstruction using commodity graphics hardware. *Magn Reson Med* 2008;59(3):463–468.
- [102] Sorensen TS, Schaeffter T, Noe KO, Hansen MS. Accelerating the nonequispaced fast Fourier transform on commodity graphics hardware. *IEEE Transactions on Medical Imaging* 2008;27(4):538–547.

- [103] Vogel C, Oman M. Iteration methods for total variation denoising. *SIAM Journal of Applied Mathematics* 1996;17:227–238.
- [104] Chambolle A, Lions PL. Image recovery via total variation minimization and related problems. *Nummer Math* 1997;76(167-188).
- [105] Chan T, Golub G, Mulet P. A nonlinear primal-dual method for total variation-based image restoration. *SIAM Journal of Applied Mathematics* 1999;20(6):1964–1977.
- [106] Chambolle A. An algorithm for total variation minimizations and applications. *Journal of Math Imaging and Vision* 2004;20(1–2):89–97.
- [107] Carter J. Dual Methods for Total Variation-based Image Restoration. Ph.D. thesis, UCLA, Los Angeles, CA, USA, 2001.
- [108] Chambolle A. Total variation minimization and a class of binary MRF models. In *Energy Minimization Methods in Computer Vision and Pattern Recognition*. 2005; 136–152.
- [109] Zhu M, Chan T. An efficient primal-dual hybrid gradient algorithm for total variation image restoration. *UCLA CAM Report 08-34*, 2008.
- [110] Zhu M, Wright SJ, Chan TF. Duality-based algorithms for total variation image restoration. *UCLA CAM Report 08-33*, 2008.
- [111] Popov LD. A modification of the Arrow-Hurwicz method for search of saddle points. *Mathematical Notes* 1980;28(5):845–848.
- [112] Goldstein T, Osher S. The split Bregman algorithm for L1 regularized problems. *UCLA Computational and Applied Mathematics Reports* 2008;08(29).
- [113] Goldfarb D, Yin W. Parametric maximum flow algorithms for fast total variation minimization. Technical report, Rice University, 2007.
- [114] Pock T, Unger M, Cremers D, Bischof H. Fast and exact solution of total variation models on the GPU. In *CVPR Workshop on Visual Computer Vision on GPU's*. Anchorage, Alaska, USA, 2008; .
- [115] Peters DC, Korosec FR, Grist TM, Block WF, Holden JE, Vigen KK, Mistretta CA. Undersampled projection reconstruction applied to MR angiography. *Magn Reson Med* 2000;43(1):91–101.
- [116] Digital Imaging and Communications in Medicine (DICOM). NEMA Publications PS 3.1-PS 3.12. The National Electrical Manufacturers Association. Rosslyn, VA, 1992, 1993, 1994, 1995.
- [117] Roujol S, de Senneville BD, Vahala E, Srensen TS, Moonen C, Ries M. Online real-time reconstruction of adaptive TSENSE with commodity CPU/GPU hardware. *Magn Reson Med* 2009;62(6):1658–1664.

- [118] Bammer R, Aksoy M, Liu C. Augmented generalized SENSE reconstruction to correct for rigid body motion. *Magn Reson Med* 2007;57(1):90–102.
- [119] Tamhane AA, Arfanakis K. Motion correction in periodically-rotated overlapping parallel lines with enhanced reconstruction (PROPELLER) and turboprop MRI. *Magn Reson Med* 2009;62(1):174–182.
- [120] Odille F, Vuissoz PA, Marie PY, Felblinger J. Generalized reconstruction by inversion of coupled systems (GRICS) applied to free-breathing MRI. *Magn Reson Med* 2008; 60(1):146–157.
- [121] Odille F, Uribe S, Batchelor PG, Prieto C, Schaeffter T, Atkinson D. Model-based reconstruction for cardiac cine MRI without ECG or breath holding. *Magn Reson Med* 2010; 63(5):1247–1257.
- [122] Nesterov Y. Smooth minimization of nonsmooth functions. *Mathematical programming Series A* 2005;103:127–152.
- [123] Nemirovski A. Prox-method with rate of convergence $O(1/t)$ for variational inequalities with Lipschitz continuous monotone operators and smooth convex-concave saddle point problems. *SIAM J Optim* 2004;15(1):229–251.
- [124] Pock T, Cremers D, Bischof H, Chambolle A. An algorithm for minimizing the Mumford-Shah functional. In *International Conference on Computer Vision (ICCV)*. Kyoto, Japan, 2009; 1133 – 1140.

Curriculum Vitae

Personal Data

Name: Florian Knoll
Date and Place of Birth: February 23, 1979
Nationality: Austrian

Education

2007 - present: Ph.D. Studies, Electrical Engineering
(Graz University of Technology)
2001 - 2006: Studies in Electrical and Biomedical Engineering
Graduation to DI (equivalent to M.Sc.) with distinction
(Graz University of Technology)
1998 - 2001: Studies in Medicine
(Medical University of Graz)
1997: Graduation Diploma (Matura)

Military Service

1997 - 1998

Academic Experience

2007 - present: Scientific Project Collaborator
Institute of Medical Engineering
Graz University of Technology
Teaching: Bioimaging Lecture (2010)
Imaging Lab (2008, 2009, 2010)
Fundamentals of Biomedical Engineering Lab (2008, 2009, 2010, 2011)

Research Grants

Co-Author of one subproject in SFB "Mathematical Optimization and Applications in Biomedical Sciences" (FWF-SFB32: Austrian Science Fund, 2011-2014).

List of Publications as First Author

Journal Publications

2011:

- Knoll, F.; Clason, C.; Bredies, K.; Uecker, M.; Stollberger, R.: Nonlinear Parallel Imaging with Variational Penalties, *Magnetic Resonance in Medicine*, accepted for publication, in press.
- Knoll, F.; Clason, C.; Diwoky, C.; Stollberger, R.: Adapted Random Sampling Patterns for Highly Accelerated MRI, *Magnetic resonance materials in physics, biology and medicine* 24 (2011) 1, P. 43 - 50.
- Knoll, F.; Bredies, K.; Pock, T.; Stollberger, R.: Second Order Total Generalized Variation (TGV) for MRI: *Magnetic Resonance in Medicine*, 65 (2011), P. 480 - 491.

2010:

- Knoll, F.; Unger, M.; Diwoky, C.; Clason, C.; Pock, T.; Stollberger, R.: Fast reduction of undersampling artifacts in radial MR angiography with 3D total variation on graphics hardware: *Magnetic resonance materials in physics, biology and medicine* 23 (2010) 2, P. 103 - 114.

Refereed Conference Proceedings

2011:

- Knoll, F.; Clason, C.; Bredies, K.; Uecker, M.; Stollberger, R.: Parallel Imaging with Nonlinear Reconstruction using Variational Penalties. To appear in *Proc. Intl. Soc. Mag. Reson. Med.* (2011).
- Knoll, F.; Bredies, K.; Stollberger, R.: Iterative parallel imaging reconstruction of time-resolved data using 3D variational regularization. To appear in *Proc. Intl. Soc. Mag. Reson. Med.* (2011).
- Knoll, F.; Freiberger, M.; Bredies, K.; Stollberger, R.: AGILE: An open source library for image reconstruction using graphics card hardware acceleration. To appear in *Proc. Intl. Soc. Mag. Reson. Med.* (2011).

2010:

- Knoll, F.; Dong, Y.; Hintermueller, M.; Stollberger, R.: Total Variation Denoising with Spatially Dependent Regularization. Proc. Intl. Soc. Mag. Reson. Med. 18:5088 (2010).
- Knoll, F.; Bredies, K.; Pock, T.; Stollberger, R.: Total Generalized Variation (TGV) for MRI. Proc. Intl. Soc. Mag. Reson. Med. 18:4855 (2010).
- Knoll, F.; Clason, C.; Aschauer, M.; Ebner, F.; Stollberger, R.: Adapted Random 3D Sampling Patterns for CE-MRA. Proc. Intl. Soc. Mag. Reson. Med. 18:3763 (2010).
- Knoll, F.; Clason, C.; Stollberger, R.: Tailored 3D Random Sampling Patterns for Non-linear Parallel Imaging. Proc. Intl. Soc. Mag. Reson. Med. 18:2876 (2010).
- Knoll, F.; Bredies, K.; Stollberger, R.: MR Image Reconstruction of Subsampled Spiral Data from Multiple Coils using Total Generalized Variation. Biomed Tech 55 (Suppl. 1): 184 - 188 (2010).
- Knoll, F.; Dong, Y.; Hintermueller, M.; Stollberger, R.: Automatic Spatially Dependent Parameter Selection for TV Denoising of MR Images with Non-Uniform Noise Distribution. Biomed Tech 55 (Suppl. 1): 198 - 202 (2010).

2009:

- Knoll, F.; Clason, C.; Uecker, M.; Stollberger, R.: Improved Reconstruction in Non-Cartesian Parallel Imaging by Regularized Nonlinear Inversion. Proc. Intl. Soc. Mag. Reson. Med. 17:2721 (2009).
- Knoll, F.; Unger, M.; Ebner, F.; Stollberger, R.: Real-Time Elimination of Undersampling Artifacts using 3D Total Variation on Graphics Hardware. Proc. Intl. Soc. Mag. Reson. Med. 17:2838 (2009).

2008:

- Knoll, F.; Ebner, F.; Keeling, S.; Stollberger, R.: Assessment of image reconstruction methods for subsampled DCE-MRI. Proc. Intl. Soc. Mag. Reson. Med. 16:3263 (2008).

Talks**2010:**

- Knoll, F.; Bredies, K.; Stollberger, R.: Second Order Total Generalized Variation for MR Image Reconstruction, SFB Workshop: Imaging with Modulated/Incomplete Data, Graz, Austria, July 8 - July 10.

2009:

- Knoll, F.: Towards real-time MR imaging: Data acquisition strategies and image reconstruction, Conference on applied Inverse Problems, Minisymposium: Magnetic Resonance and Magnetic Induction Tomography, Vienna, Austria, July 20 - July 24.

2008:

- Knoll, F.; Unger, M.; Ebner, F.; Stollberger, R.: Real time elimination of undersampling artifacts in CE MRA using variational denoising on graphics hardware, 20th annual international conference on magnetic resonance angiography, Graz, Austria, October 15 - October 18.
- Knoll, F.; Ebner, F.; Keeling, S.; Stollberger, R.: Compressed Sensing reconstruction for subsampled DCE - MRI, OEGMP Annual Meeting and 3rd AISCMP Meeting, Graz, Austria, May 30 - May 31.

Poster Presentations**2010:**

- Knoll, F.; Bredies, K.; Stollberger, R.: Total Generalized Variation (TGV) constrained reconstruction of undersampled MRI data from multiple coils, Workshop on Novel Reconstruction Strategies in NMR and MRI 2010, Goettingen, Germany, September 9-11.
- Knoll, F.; Clason, C.; Stollberger, R.: Nonlinear Parallel Imaging for Variable Density Sampling Patterns, SFB Workshop: Imaging with Modulated/Incomplete Data, Graz, Austria, July 8 - July 10.
- Knoll, F.; Dong, Y.; Hintermueller, M.; Stollberger, R.: Automatic Spatially Dependent Regularization Parameter Selection for Variational Denoising of MR Data Sets, SFB Workshop: Imaging with Modulated/Incomplete Data, Graz, Austria, July 8 - July 10.

2009:

- Knoll, F.; Clason, C.; Bredies, K.; Unger, M.: Optimierte Bildrekonstruktion für unterabgetastete MR-Bildgebung, Jahrestagung 2009 der Österreichischen Gesellschaft für Biomedizinische Technik, Graz, Austria, October 2.
- Knoll, F.; Clason, C.; Ebner, F.; Aschauer, M.; Stollberger, R.: CE-MRA with tailored 3D random sampling patterns and nonlinear parallel imaging reconstruction, 21th annual international conference on magnetic resonance angiography, East Lansing, Michigan, USA, September 29 - October 1.

2008:

- Knoll, F.; Stollberger, R.; Ebner, F.: Assessment of Different Image Reconstruction Methods for DCE-MRI, European Conference of Radiology, Vienna, Austria, March 7 - March 11.

Miscellaneous**2011**

- Receiver of an ISMRM Educational Travel Stipend.

2010

- Finalist: ISMRM 2010 Reconstruction Challenge: Need for Speed competition.
- Receiver of an ISMRM Educational Travel Stipend.

2009

- 21st Annual International Conference on Magnetic Resonance Angiography: First Place Poster Presentation: CE-MRA with tailored 3D random sampling patterns and nonlinear parallel imaging reconstruction.
- Best Ph.D. thesis award 2009 (finished and ongoing work) of the Austrian Society for Biomedical Engineering.
- Receiver of an ISMRM Educational Travel Stipend.

Acknowledgments

This thesis would not have been possible without the support of numerous people, and I am very happy to be able to thank them in this section.

First of all, I would like to thank **Prof. Rudolf Stollberger** for introducing me to the exciting and extremely rewarding field of medical imaging and in particular to MR image reconstruction. He always supported me and gave me the freedom to pursue my research in directions that were of special interest to me.

MR image reconstruction is a very interdisciplinary field that brings together radiologists, physicists, engineers, computer scientists and mathematicians. Therefore the SFB Research Center "Mathematical Optimization and Applications in Biomedical Sciences" was an optimal working environment that will be hard to beat in the future. No result in this thesis would have been possible without the fruitful cooperation between medical engineers and mathematicians. Therefore special thanks go to **Prof. Karl Kunisch** for putting together this SFB, and **Prof. Stephen Keeling**, the principal investigator of subproject "Inverse". In addition, I have to highlight two people within the SFB. **Christian Clason**, my main collaborator in all work concerning the nonlinear inversion method, and **Kristian Bredies**, the pioneer of TGV, who was very excited about the application in MR imaging. The enthusiasm of both of you is extremely contagious and motivating, and I am really looking forward to any joint work in the future.

A big thanks goes to all people at the Institute of Medical Engineering for providing such a relaxed and productive atmosphere, especially the MR team consisting of **Clemens Diwojky**, **Michael Hofer**, **Markus Kraiger**, **Bernhard Neumayer**, **Peter Opriessnig** and **Andreas Petrovic**. Special thanks to Bernhard for numerous exciting Badminton matches.

The talent of **Manuel Freiberger** to instantly understand even the most complicated problems always impressed me from the first day as an undergraduate student. Thank you Manuel for many interesting discussions, your support with our CUDA reconstruction computer, funny gaming nights and an almost decade-long friendship.

The help and experience in GPU computing of **Markus Unger** and **Thomas Pock** from the Institute of Computer Graphics and Vision was invaluable.

I want to thank **Martin Uecker** from the Max Plank Institute in Goettingen for many interesting discussions about image reconstruction in general and the IRGN method in particular. Additional thanks go to **Tobias Block** from Siemens Medical Solutions in Erlangen.

Christian Langkammer and **Michaela Soellinger** from the department of Neurology (Medical University Graz) often helped during MR measurements.

Finally, I would like to thank my sister and my parents, **Hannah, Robert** and **Sigrid Knoll** for always supporting me during my studies. I dedicate this thesis to you.